

INFORMATION TO USERS

This material was produced from a microfilm copy of the original document. While the most advanced technological means to photograph and reproduce this document have been used, the quality is heavily dependent upon the quality of the original submitted.

The following explanation of techniques is provided to help you understand markings or patterns which may appear on this reproduction.

1. The sign or "target" for pages apparently lacking from the document photographed is "Missing Page(s)". If it was possible to obtain the missing page(s) or section, they are spliced into the film along with adjacent pages. This may have necessitated cutting thru an image and duplicating adjacent pages to insure you complete continuity.
2. When an image on the film is obliterated with a large round black mark, it is an indication that the photographer suspected that the copy may have moved during exposure and thus cause a blurred image. You will find a good image of the page in the adjacent frame.
3. When a map, drawing or chart, etc., was part of the material being photographed the photographer followed a definite method in "sectioning" the material. It is customary to begin photoing at the upper left hand corner of a large sheet and to continue photoing from left to right in equal sections with a small overlap. If necessary, sectioning is continued again — beginning below the first row and continuing on until complete.
4. The majority of users indicate that the textual content is of greatest value, however, a somewhat higher quality reproduction could be made from "photographs" if essential to the understanding of the dissertation. Silver prints of "photographs" may be ordered at additional charge by writing the Order Department, giving the catalog number, title, author and specific pages you wish reproduced.
5. PLEASE NOTE: Some pages may have indistinct print. Filmed as received.

University Microfilms International

300 North Zeeb Road
Ann Arbor, Michigan 48106 USA
St. John's Road, Tyler's Green
High Wycombe, Bucks, England HP10 8HR

77-11,457

McCARTHY, Donald Wans, Jr., 1948-
AN INFRARED SPATIAL INTERFEROMETER: DESIGN
AND DISCOVERIES.

The University of Arizona, Ph.D., 1976
Physics, astronomy and astrophysics

Xerox University Microfilms, Ann Arbor, Michigan 48106

AN INFRARED SPATIAL INTERFEROMETER:
DESIGN AND DISCOVERIES

by

Donald Wans McCarthy, Jr.

A Dissertation Submitted to the Faculty of the
DEPARTMENT OF ASTRONOMY
In Partial Fulfillment of the Requirements
For the Degree of
DOCTOR OF PHILOSOPHY
In the Graduate College
THE UNIVERSITY OF ARIZONA

1 9 7 6

THE UNIVERSITY OF ARIZONA

GRADUATE COLLEGE

I hereby recommend that this dissertation prepared under my
direction by Donald Wans McCarthy, Jr.
entitled An Infrared Spatial Interferometer: Design and
Discoveries
be accepted as fulfilling the dissertation requirement of the
degree of Doctor of Philosophy

Frank J. Low
Dissertation Director

Oct. 26, 1976
Date

After inspection of the final copy of the dissertation, the
following members of the Final Examination Committee concur in
its approval and recommend its acceptance:*

Frank J. Low
Kolger J. Thompson
Keith J. Woolf
Ron S. Hilliard

Oct 27, 1976
Oct 27, 1976
Nov 3, 1976

*This approval and acceptance is contingent on the candidate's
adequate performance and defense of this dissertation at the
final oral examination. The inclusion of this sheet bound into
the library copy of the dissertation is evidence of satisfactory
performance at the final examination.

STATEMENT BY AUTHOR

This dissertation has been submitted in partial fulfillment of requirements for an advanced degree at The University of Arizona and is deposited in the University Library to be made available to borrowers under rules of the Library.

Brief quotations from this dissertation are allowable without special permission, provided that accurate acknowledgment of source is made. Requests for permission for extended quotation from or reproduction of this manuscript in whole or in part may be granted by the head of the major department or the Dean of the Graduate College when in his judgment the proposed use of the material is in the interests of scholarship. In all other instances, however, permission must be obtained from the author.

SIGNED:

Donald W. McCarthy Jr.

PREFACE

We set sail on this new sea because there is new knowledge to be gained and new rights to be won, and these must be won and used for the progress of all people.

But why, some say, the moon? Why choose this as our goal? And they may well ask: Why climb the highest mountain? Why thirty-five years ago fly the Atlantic? We choose to go to the moon! We choose to go to the moon in this decade and do the other things, not because they are easy but because they are hard--because that goal will serve to organize and measure the best of our energies and skills; because that challenge is one we are willing to accept, one we are unwilling to postpone and one we intend to win.

-- John F. Kennedy, "To the Moon"
(Time-Life Records).

* * * * *

This dissertation owes its existence to those family members, coaches, and friends who have instilled in me an enthusiastic curiosity about the nature of God's universe. They have shown me that humans can understand and appreciate the gross properties of Nature and can constructively apply this knowledge in daily life.

I wish especially to thank Dr. Frank Low, my advisor, in whose imagination this project was conceived and who patiently provided ideas and impetus during the development of the interferometric method.

Naturally in any successful experimental project, the final product is the result of help from many individuals with their own special skills. This project has benefitted from help by Dr. Rodger

Thompson, Mike Reed, Nick Gautier, Griffin, Wade, George, Arnold, Ken, Earl, Harold, and Jim.

Dr. Ron Hilliard meticulously read an early draft of this dissertation and offered many helpful criticisms and comments.

Of course, special thanks go to my wife, Carol, and my family who patiently stood by and encouraged me along the way. Carol typed two early drafts of the thesis and other family members gave financial assistance. I also want to thank my grandparents, two of whom were enthusiastically with me at the start but were unable to see the final product.

TABLE OF CONTENTS

	Page
LIST OF TABLES.	viii
LIST OF ILLUSTRATIONS	ix
ABSTRACT.	xi
 1. APPLICATIONS OF HIGH SPATIAL RESOLUTION IN INFRARED ASTRONOMY	 1
Infrared Stars.	3
Importance of High Spatial Resolution	3
Current Techniques of Spatial Resolution.	9
Expected Angular Diameters.	12
Infrared Nebulae.	14
Infrared Galaxies	17
Solar System Objects.	20
Overview of This Research	20
 2. SPATIAL INTERFEROMETRY: THEORY AND PRACTICE.	 22
Physical Foundations.	23
Angular Resolution.	29
Atmospheric Phenomena	31
Infrared Considerations	35
 3. DESIGN OF THE INTERFEROMETER.	 38
Design Considerations	38
Principles of Operation	42
The Stage	46
Aperture Mask	50
Adjusting Mirrors	50
Roof Mirror	53
Beamsplitter.	55
Dewar and Detector Systems.	55
System-One.	56
System-Two.	57
Slotted Masks	58
Visual Focus.	59
Telescopic Requirements	59
The Beam Converter.	61
Electronics	61

TABLE OF CONTENTS--Continued

	Page
4. EXPECTED INSTRUMENTAL RESPONSE; LABORATORY TESTS.	64
Interferometric Magnification	64
Beam Patterns	67
Expected Response to a Point Source	70
Laboratory Tests.	73
Principles of Data Analysis	79
5. OPERATION AND PERFORMANCE OF THE INTERFEROMETER AT THE TELESCOPE	83
Atmospheric Perturbations of the Interference Pattern . . .	84
Phase and Amplitude Fluctuations of the Fringe Signal	84
Rediscussion of Instrumental Tolerances	86
Operating Procedures.	87
Alignment	87
Measurement	92
Data Analysis	95
Electronic Processing	95
Conversion to Fringe Visibilities	98
System Performance.	99
Sensitivity	99
Measurement Accuracy and Sources of Error	100
Observed Response to a Point Source	103
Minor Problems.	104
6. ATMOSPHERIC AND ASTROPHYSICAL RESULTS	106
Atmospheric Results	107
Correlation Between Visual and Infrared Seeing.	107
Fringe Stability in Excellent Seeing.	110
Wavelength Dependence of Seeing	112
An Instance of Anomalous Infrared Seeing.	112
Astrophysical Results	113
Observations and Reductions	113
IRC +10216.	117
VY CMa.	121
NML Cyg	122
Unresolved Stars.	124
7. CONCLUSIONS AND IDEAS FOR THE FUTURE.	125
Observational Results	125
Limitations to This Technique	127
Improvements in Instrumentation	130
Future Observational Goals.	136

TABLE OF CONTENTS--Continued

	Page
APPENDIX A: DESIGN AND TESTS OF THE PIEZOELECTRIC CRYSTAL STACKS.	138
REFERENCES.	142

LIST OF TABLES

Table		Page
1.1	Expected Angular Diameters and Previous Measurements for Selected Stars.	13
3.1	Instrumental Tolerances Required for Operation During Ideal Atmospheric Conditions.	48
5.1	Instrumental Tolerances Required for Operation During Typical Seeing Conditions	88
6.1	Visibility Measurements and Angular Diameters for Observed Stellar Sources	116

LIST OF ILLUSTRATIONS

Figure		Page
2.1	Young's Double Slit Experiment	24
2.2	The Visibility Function.	26
3.1	Beamsplitter Optics for a Spatial Interferometer	39
3.2	Schematic Diagram of the Spatial Interferometer.	41
3.3	Fringe-Chopped Intensity Profiles.	44
3.4	The Interferometer Mounted on the 90-Inch Telescope.	47
3.5	The Stage.	49
3.6	Schematic Diagram of Interferometer Electronics.	62
4.1	Theoretical Beam Patterns.	69
4.2	Theoretical Normalized Fringe Amplitude of a Point Source. .	72
4.3	Schematic Diagram of Test Equipment.	74
4.4	Laboratory Measurements of Visibility Functions.	76
4.5	Laboratory Measurements of Angular Diameters	78
5.1	Alignment of the Interferometer.	89
5.2	Schematic Diagram of Data Analysis Electronics	96
6.1	Extremes of Infrared Seeing.	108
6.2	Interferogram of α Boo	111
6.3	Anomalous Behavior of Infrared Seeing.	114
6.4	Visibility Measurements of IRC +10216 and VY CMa	119
6.5	Measurements of Fringe Amplitude and Flux from IRC +10216 and R Leo.	120

LIST OF ILLUSTRATIONS--Continued

Figure		Page
6.6	Measurements of Fringe Amplitude and Flux from VY CMa and α Ori.	123
7.1	An Improved, Low Background Aperture Mask.	132
7.2	Schematic Diagram of a Servo-Controlled Spatial Interferometer	133
7.3	A New Alignment Technique.	135
A.1	Expansion Versus Voltage for the Piezoelectric Fringe Chopper	140

ABSTRACT

A new type of infrared interferometer has been developed to increase substantially the angular resolution of infrared astronomical observations. While operating on conventional telescopes of diameter 1.5, 2.3 meters and at a wavelength of 5 microns ($\Delta\lambda = 0.7$ microns), this instrument has successfully measured fringe visibilities of astronomical objects in the presence of atmospheric "seeing." It is the first infrared interferometer to resolve the angular diameters of circumstellar shells and to study their shapes. As a result, the angular resolution of telescopic observations at 5 microns has been extended from ~ 1 arc sec to ~ 0.1 arc sec.

Eleven stars were observed during good atmospheric conditions at baselines ranging from 1.0 to 1.9 meters. The circumstellar shells of IRC +10216 and VY CMa are resolved and upper limits are placed on the angular diameters of nine other stars. The size and structure of IRC +10216 are consistent with previous lunar occultation results requiring two spherical shells of angular diameters 0.44 and 2.0 arc sec. The angular diameter of VY CMa is approximately 0.45 arc sec. An upper limit of 0.3 arc sec exists on the angular size of NML Cyg. The angular diameter for each of these three stars nearly equals the diameter of a uniform, circular, unit emissivity disk having the observed 5 micron flux and color temperature.

Atmospheric disturbances cause shifts of amplitude and phase in the infrared fringe pattern. These shifts occur at frequencies

varying from ~ 0 to greater than 40 Hz depending on atmospheric conditions; and they have necessitated special methods of observation and data analysis. Current observations suggest that the amplitude fluctuations are inversely proportional to wavelength. During excellent atmospheric conditions, the 5 micron fringes are highly stable, showing only small phase shifts of $\lesssim \frac{\pi}{2}$ during a time of ~ 40 seconds. Observational experience suggests the existence of at least two different regimes of infrared "seeing," which differ in characteristics of the amplitude and phase shifts of the fringe pattern.

The existing infrared spatial interferometer was designed to be a versatile, test instrument. The possibility now exists of using this instrument with baselines longer than 2 meters to achieve 5 micron resolutions greater than 0.1 arc sec. Only minor instrumental modifications are necessary to observe at longer wavelengths, such as 11 and 20 microns.

CHAPTER 1

APPLICATIONS OF HIGH SPATIAL RESOLUTION IN INFRARED ASTRONOMY

Although infrared observations began in the year 1800 with the work of Sir William Herschel, the modern science of "infrared astronomy" has appeared only within the last fifteen years and is now evolving rapidly into a state of technological sophistication which is producing important astronomical discoveries. Curiously, this recent transition has followed the earlier pattern of radio astronomy in the sense that improvements in instrumental sensitivity and angular resolution are leading the way. For example, after Low (1961) invented a sensitive, low temperature detector for far-infrared observations, new techniques were developed to permit high quality photometric and spectroscopic measurements using ground-based telescopes in the atmospheric windows from 1-40 μ and 350 μ . Now astronomers utilize the full diffraction-limited performance of large telescopes to map complex sources and to resolve discrete sources at resolutions down to ~ 1.0 arc sec. Nevertheless, the angular sizes of many intriguing infrared sources remain unresolved, and thus their physical nature is uncertain.

Undoubtedly, infrared astronomy would benefit from the application of interferometric techniques to increase the spatial resolution of observations. This step might be considered a major advance in astronomy and could be compared to the use of the first radio

interferometer in the 1950's (Strom, Miley and Oort 1975). Not only did improved understanding of radio sources result but also the basic concepts of interferometry were soon extended into the powerful techniques of aperture synthesis and very long baseline interferometry whereby discrete and extended sources are now mapped at resolutions of a milliarcsecond (Ryle 1975; Swenson and Kellermann 1975). The chapters presented here trace the development of a simple interferometric technique which was designed to extend infrared spatial resolution from ~ 1.0 arc sec to about 0.1 arc sec. It is hoped that this work will contribute to infrared astronomy in the same way that early interferometers benefited radio astronomy.

Since 1961, the discoveries from infrared sky surveys and the observations of many individual sources have helped astronomers realize the significance of a variety of objects which radiate energy primarily at wavelengths between 1 and 1000 μ (the "infrared" spectral region). For discussion purposes, these objects are classified into the following infrared groups: stars, nebulae, galaxies and solar system objects. The remainder of this chapter describes these sources briefly and demonstrates that high spatial resolution observations can help answer various fundamental questions concerning each one. In addition, present techniques of spatial resolution are described and evaluated in terms of current needs. Special emphasis is given to the infrared stars because they are the targets of the observational work in this dissertation.

Infrared Stars

Importance of High Spatial Resolution

The term "infrared star" denotes a star radiating more infrared energy than expected from a blackbody whose temperature is appropriate to the stellar spectral type. This so-called "infrared excess" is believed to be generated by a circumstellar envelope (or "shell") of gas and dust and is exhibited by a large assortment of stars including M supergiants, some F, G, and K supergiants, RV Tauri stars, late-type giants, A and B emission stars, Mira variables, T Tauri stars, Wolf-Rayet stars, and novae. Among such stars, specification of the general characteristics of the infrared excess has been an area of active research. Details of recent observations and theories can be found in the reviews of Woolf (1973) and Stein (1975).

The belief that circumstellar envelopes actually exist and can generate infrared excesses is based mainly on indirect evidence from optical (Reddish 1967; Strom, Strom and Yost 1971), infrared (Low and Smith 1966; Mendoza 1966 and 1968), and radio (Hyland et al. 1972) observations as well as from theoretical investigations (Gilman 1969 and 1974). Presently, only two physical processes are required to account for this excess radiation: thermal reradiation from dust particles and free-free interactions in chromospheric gas.

The first process postulates the existence of dust grains in a circumstellar shell (Low and Smith 1966). These grains attain thermal equilibrium by absorbing short wavelength radiation from the central star and by emitting an equal quantity of infrared energy which is

characteristic of the low temperature of the grains. Consequently, more infrared energy is generated than expected from the star. Observationally, the existence of circumstellar grains has strong support. Identified grain materials include: silicates (Woolf and Ney 1969; Low and Swamy 1970); silicon-carbide (Treffers and Cohen 1974); and perhaps carbon, iron and nitrides (Treffers and Cohen 1974; Stein 1975). Already the dust shells of two infrared stars have been resolved by lunar occultations, thus providing support for the validity of this mechanism.

In the second emission process, free-free and free-bound interactions occur between electrons and neutral hydrogen atoms in a warm stellar chromosphere (Dyck and Milkey 1972; Gilman 1974). This mechanism can produce infrared excesses in both early and late-type stars and explains the excess radiation at wavelengths between 1-8 μ . Verification of this model rests on agreement between theoretical and observed spectra as has been obtained by Gilman (1974). This process also creates the observed "veiling" of optical and near-infrared absorption lines (Humphreys 1974).

A current astronomical consensus is that both processes operate in the envelopes but with varying degrees of importance. For example, Wallerstein (1971) has suggested that there is a continuous sequence of stars with the Be stars at one end showing pure free-free emission and stars like NML Cyg and VY CMa at the other end showing only thermal reradiation from dust.

By studying infrared stars at high spatial resolution, we can determine the angular size, shape, and structure of the envelopes.

This information will be valuable in order to:

1. verify the two proposed emission mechanisms;
2. verify existing theoretical models which have made predictions concerning the characteristics of certain infrared stars;
3. investigate the presence of nonthermal energy sources;
4. deduce the physical and chemical properties of the dust grains;
5. determine the evolutionary processes occurring within the different types of infrared stars; and
6. determine effective temperatures of the normal, late-type stars.

Because most types of dust grains are not expected to survive in the hot environment close to a star, a dust shell must have a larger angular diameter than the chromospheric region where free-free interactions occur at temperatures of several thousand degrees. Thus, angular diameter measurements can determine which emission process is the dominant contributor to the infrared spectrum. Also, the angular dimensions of a dust shell may depend on the wavelength of observation since a distribution of dust probably extends radially outward from the star. This effect is not expected if free-free emission is the dominant energy source.

During the last decade, many theoretical dust shell models have been proposed to explain the characteristics of infrared stars.

Such stars include VY CMa (Herbig 1970b), NML Cyg (Herbig 1974b), and R Mon (Low and Smith 1966). Occasionally, such theories make predictions which can be tested observationally; for example, some predict the angular diameter as a function of wavelength (Apruzese 1975). These theories require observational support if we are to distinguish between conflicting models and determine the real properties of the object. Many theorists and observationalists recognize this dilemma and have requested high spatial resolution measurements (Low and Smith 1966; Robinson, Hyland and Thomas 1973; Stein 1975).

High resolution studies also provide a test of the assumption that the only energy input into the stellar dust envelope is short wavelength radiation from the central star. A priori, we should not exclude other processes such as heating of dust by interactions with high energy, charged particles in a magnetosphere surrounding the star or by dissipation of mechanical energy generated by convective or other motions of stellar material (Gilman 1974; Thomas 1973). Such additional sources would raise the dust temperature above the value generated by stellar radiation alone. A significant effect can be detected in the following way. For a measured angular size of the shell and a given temperature of the central star, one calculates the expected dust temperature and compares it to the temperature deduced from photometry. A gross difference would be evidence for additional energy sources.

It is also possible to deduce the physical and chemical properties of the circumstellar dust by using the measured sizes of infrared stars as inputs to existing theories. Recently,

Apruzese (1975) has published detailed radiative transfer models of some infrared stars including VX Sgr, R Mon, VY CMa, IRC +10216, etc. From measured or assumed angular sizes of these stars he can calculate the optical properties of the dust particles and determine the density distribution of dust within the shell. Thus, such measurements can help determine the size, shape, and composition of circumstellar particles. The possibility has also been discussed by Stein and Ney (1974). Since some of these particles may be "blown" outward from the star and become a major constituent of the interstellar medium, we may be able to study interstellar grains and the evolution of the interstellar medium.

Over the years the origin of circumstellar dust has been a matter of considerable speculation. High spatial resolution studies should provide concrete information concerning this problem and the evolutionary processes occurring in infrared stars. Currently, there are three explanations for the origin of the dust shells:

1. the central star is an evolved object which is losing mass and the ejected mass condenses into dust particles (Geisel 1970; Fix and Alexander 1974);
2. the central star allows condensation of particles in its atmosphere and radiation pressure ejects them along with gas; and
3. the central star is a protostar which is surrounded by remnants of its original dust and gas cloud (Herbig 1970a).

Geisel's (1970) work supports the first explanation. Her studies of a wide variety of stars indicate that the envelope may not be a

permanently stable phenomenon but rather is governed by equilibrium behavior in which dust is continuously condensed and ejected into interstellar space. Conceivably, differences in angular size and optical thickness of circumstellar envelopes may be caused by different rates of mass loss. Therefore, angular size measurements may not only reveal the rate of mass loss but also provide a means to study the condensation mechanism of the dust.

The third explanation is supported by a wealth of observational and theoretical evidence, some of which is discussed here. Larson (1969) has predicted some observational consequences of the process of star birth. For instance, massive stars which are just reaching the main sequence should retain a remnant of the circumstellar cloud from which they formed whereas less massive stars will show such a remnant only in their pre-main sequence evolution. Observational support of this prediction is given by Strom et al. (1972) from their study of Ae and Be stars. These authors also conclude that the observed envelopes are flattened disks rather than spherically symmetric shells. Similarly, Woolf (1973) and Cohen (1974) have suggested that T Tauri stars and stars in cometary nebulae will form dense, flattened disks. Possible examples of such objects are the Egg Nebula (Ney 1975), VY CMa (Herbig 1970b), the Becklin-Neugebauer source in Orion (Becklin and Neugebauer 1967), and an infrared star located near a Herbig-Haro object (Strom, Strom and Grasdalen 1974). It seems clear that observations of angular size and shape of these and other objects may lead to unequivocal conclusions about their evolutionary status.

Finally, high spatial resolution studies can provide new insight into the evolution of pulsating variables and novae. For example, the prototype Mira variable, α Ceti, is ejecting particles which have formed within its atmosphere (Shaw 1972). High resolution studies could verify the existence and symmetry of the pulsations and could conceivably reveal how these particles are ejected into space. In the case of Nova Serpentis 1970, which became a luminous infrared source (Geisel, Kleinmann and Low 1970), the expansion rate could have been measured. In conjunction with narrow band photometric data, the condensation process could have been studied and then applied to the more normal infrared stars which are undergoing continuous mass loss.

A final point concerns measurement of the effective temperatures of normal, cool stars which are not surrounded by circumstellar dust shells. By measuring the star's total absolute flux, angular size, and distance, it is possible to derive its effective temperature, radius, and absolute luminosity. This information is needed to calibrate the spectral type versus temperature relation and to plot stars as observed points in a theoretical HR diagram. Results for early-type stars have been published by Code (1975). For late-type stars, current knowledge is summarized by Johnson (1966).

Current Techniques of Spatial Resolution

Presently, three techniques exist for measuring the angular size of an infrared star: (1) variable beam size studies; (2) scanning techniques; and (3) lunar occultations. Even though available observations have not resolved many infrared stars, the existing

results are important not only for their scientific merit but also because they provide a glimpse of what can be learned by employing higher resolutions.

The variable beam size technique is illustrated by the work of Low and Swamy (1970). At a wavelength of $22\ \mu$, they attempted to resolve the circumstellar dust shell of α Ori which showed a "silicate" emission feature at this wavelength. Using different instrumental beam sizes, they obtained $22\ \mu$ photometric data and, in each case, calculated the observed flux density. If the object is unresolved (i.e., smaller than the beam), the relationship between flux density and beam size will be one of constant flux density. However, when the object becomes resolved, smaller beams will show decreased flux density. Clearly, limitations to this method are imposed by telescopic diffraction and atmospheric seeing.

A second procedure is to scan the source across a narrow slit which is being "switched" between the source and the sky. For a scan made in a direction perpendicular to the slits, the source will drift slowly through each and the resulting signal will rise to a peak amplitude and then decrease to a peak in the opposite phase. Scans are obtained of nearby point sources and of the object under study. The observed signal patterns are then fit by a profile consisting of a convolution of the intensity distribution of the extended source with the observed pattern from the point source. The latter represents the instrumental profile including the effects of diffraction and seeing. The intensity distribution of the source can be modelled so that different fits are obtained for various assumed values of the angular size.

This technique was employed by Gehrz et al. (1973) who resolved η Car at wavelengths between 2.2 and 18 μ . They observed that the angular size increased from 2 arc sec at 2.2 μ to 6 arc sec at 10-18 μ . Although an object whose angular size is less than the diffraction limit can be "resolved," this technique is limited by diffraction and seeing so that angular diameters below ~ 0.5 -1.0 arc sec cannot be determined.

In the third technique, one records the intensity variation in the Fresnel diffraction pattern caused by a lunar occultation of the observed source. From this data, it is possible to recover the object's angular size, brightness distribution in one direction, and location. This technique is similar to the operation of a variable baseline interferometer and is discussed in detail by Lang (1971). Results have been obtained by Toombs et al. (1972) on IRC +10216 (carbon star) and by Zappala et al. (1974) on IRC +10011 (M-type Mira variable) for wavelengths between 2.2 and 20 μ . These authors show that the structures of these circumstellar shells are consistent with either multiple shells at different temperatures or with a smooth, radial distribution of dust away from the central star. Although the lunar occultation technique is a powerful one capable of high resolution, it is limited to only a few objects and astronomers are at the mercy of weather and the lunar ephemeris. Also, only one position angle on the sky is observable for each occultation.

Expected Angular Diameters

In this section the expected angular diameters of several infrared sources are derived and it is demonstrated that the beam size and scanning techniques cannot hope to resolve the majority of known infrared stars. Working at a wavelength of 5μ , we shall model infrared sources as optically thick, circularly symmetric disks of unit emissivity radiating like blackbodies at temperature T_c (note comments by Stein and Ney 1974). Photometric observations determine the color temperature, T_c , and 5μ flux density, $F_{5\mu}$. The expected angular diameter at 5μ is then given by θ_{\min} as follows:

$$F_{5\mu} \approx B_{5\mu}(T_c) \frac{\theta_{\min}^2}{4}, \quad (1.1)$$

where $B_{5\mu}(T_c)$ is the Planck function at temperature T_c . Note then that θ_{\min} is the minimum diameter expected for this ideal source; both a non-ideal (< 1) particle emissivity and a lower optical depth will increase θ_{\min} .

For several normal and infrared stars, Table 1.1 lists the derived values of θ_{\min} obtained from 5μ photometric observations as indicated. The apparent 5μ magnitude is designated by M . For the infrared stars, the temperatures and flux densities refer to the circumstellar dust envelope, as noted. For comparison, existing angular diameter measurements are also listed.

Table 1.1. Expected Angular Diameters and Previous Measurements for Selected Stars

PHOTOMETRIC DATA				ANGULAR DIAMETERS			
Object	M	T_c (°K)	Ref.*	θ_{\min} (arc sec)	Previous Measurements		Ref.*
					θ_{λ} (arc sec)	$\lambda(\mu)$	
VY CMa	-3.9	580	1	0.36	
IRC +10216	-3.9	$\begin{bmatrix} 375 \\ 600 \end{bmatrix}$		$\begin{bmatrix} 0.98 \\ 0.28 \end{bmatrix}$	$\begin{bmatrix} 2.0 \\ 0.44 \end{bmatrix}$	4.8	2
	-5.0	$\begin{bmatrix} 375 \\ 600 \end{bmatrix}$	3	$\begin{bmatrix} 1.6 \\ 0.39 \end{bmatrix}$	
NML Cyg	-3.5	580	1	0.29	
α Ori	-4.3	3500	1,4	0.041	$\begin{bmatrix} 0.062 \\ 0.044 \end{bmatrix}$	$\begin{bmatrix} 0.42 \\ 0.63 \end{bmatrix}$	5
α Boo	-3.0	4000	3,6	0.020	0.026	0.5	5
α Her	-3.2	3400	7	0.025	0.031	0.5	8
R Leo	-3.4	2000	3,9	0.044	
α Sco	-3.8	3500	10	0.033	0.039	0.43	11
VX Sgr	-2.2	3000	10	0.018	
X Cyg	-2.6	$\begin{bmatrix} 1675 \\ 2425 \end{bmatrix}$	7,12	$\begin{bmatrix} 0.036 \\ 0.030 \end{bmatrix}$	
	-3.0						
W Hya	-4.3	2200	13,14	0.052	

*References and Notes:

- Low et al. (1970)
- Toombs et al. (1972); equally bright components are assumed
- Becklin et al. (1969)
- Low and Swamy (1970)
- Currie et al. (1974)
- Low and Rieke (1974)
- Gillett et al. (1968)
- Gezari et al. (1972)
- Gillett et al. (1971)
- Humphreys et al. (1972); 3500°K temperature is assumed
- Evans (1955)
- Johnson et al. (1965)
- Neugebauer et al. (1971); 25% of the 5μ flux is excess radiation above that of a 2000°K blackbody; θ_{\min} calculation ignores this excess
- Gehrz and Woolf (1971)

Clearly, most of the objects have expected diameters less than 0.5 arc sec and are beyond the resolution limits of the beam size and scanning techniques. Current observational evidence suggests that these expectations are consistent with reality (Stein and Ney 1974).

To summarize, it is clear that interferometric techniques are required for high spatial resolution measurements of infrared stars and that such data can be applied profitably to the study of many fundamental properties of these objects. So far only a taste of the benefits has resulted from modern techniques.

Infrared Nebulae

"Infrared nebulae" are galactic infrared sources whose angular dimensions range from a few arc seconds to 30 arc minutes or more. To date, most of these objects are identified with H II regions and planetary nebulae. Both have infrared excesses at wavelengths beyond $10\ \mu$ in the sense that they radiate more energy than expected from the free-free interactions in the region of ionized gas.

A recent review article summarizes the infrared properties and models of H II regions (Wynn-Williams and Becklin 1974). Since about 1967 progress in this field has been achieved by the use of techniques to map sources at different wavelengths ($2.2\ \mu$ to $\sim 1\ \text{mm}$) and angular resolutions (~ 1 arc sec to 1 arc min). The current picture proposes that dust grains are mixed with and heated by ambient gas. This process generates an infrared excess from $\sim 5\text{--}20\ \mu$. However, H II regions characteristically emit most infrared energy at $100\ \mu$, and it is thought

that this energy originates from colder dust lying outside the H II region in the neutral gas (Lemke and Low 1972).

Accompanying these large features are smaller sources, both extended and discrete, which have been discovered within and around H II regions. Examples are found in the Orion nebula. Approximately one arc minute to the northwest of the Trapezium is a cluster of four optically invisible infrared sources. Two of these are unresolved at a resolution of 5 arc sec, and one is unresolved at 2 arc sec. The latter is the "BN" object (Becklin and Neugebauer 1967). The remaining member is an extended nebula (Kleinmann and Low 1967) whose overall angular size is ~ 30 arc sec. This entire "infrared cluster" is associated with many OH/H₂O maser sources and lies at the center of a CO molecular cloud. A similar cluster exists outside the H II region (Gatley et al. 1974).

The overall model for the Orion H II region and similar objects (e.g., W3) pictures the birth of a star cluster from a diffuse cloud of dust and molecular gases. Observational evidence suggests that we are viewing clusters of protostars in different stages of their evolution toward the main sequence.

Planetary nebulae are also extended sources of infrared emission having excesses between wavelengths of 10 and 18 μ . Cohen and Barlow (1974) have conducted a photometric survey of 113 planetaries from 2.2 to 22 μ . They believe the excesses are caused by thermal emission from cool ($\sim 180^\circ\text{K}$) dust grains which are heated by absorption of Ly radiation from the central star. There is some evidence for

nonuniform emission but no real "hot spots" have appeared within the emitting region. Some observations indicate that dust exists beyond the optical limits of the nebulae. Conceivably, the dust condenses within outflows of mass from the nuclei of these nebulae.

At the present time studies of infrared nebulae are limited by modern techniques. For example, the Orion nebula region has been mapped by combining a series of beam switched flux measurements or individual scans which have been spaced periodically across the region of interest. The data at each position can then be contoured. However, the beam switching technique often suppresses low contrast, extended features and the current picture of the Orion infrared sources has taken more than eight years to assemble; even this picture is limited to ~ 1 arc sec resolution by diffraction and seeing effects. Clearly, it would be desirable to improve such methods as radio astronomers have done by means of aperture synthesis. Thus, higher resolution maps could be obtained more efficiently. This is one benefit which can be anticipated by the introduction of interferometric techniques to infrared astronomy.

More accurate maps of extended sources and better resolution of discrete sources will help to answer the following questions:

1. does cold dust exist outside the boundaries of the ionized gas in H II regions and planetary nebulae;
2. what is the detailed structure and physical nature of the extended nebulae found within H II regions;
3. is detailed infrared structure present in the planetary nebulae; and

4. what is the physical and evolutionary nature of the discrete sources ("infrared protostars"?) in infrared clusters?

Infrared Galaxies

Infrared studies of galactic nuclei are of great current interest in astrophysics (Stein 1975). Extensive observations have revealed that many galaxies emit the bulk of their energy in the infrared and that the infrared luminosities of galactic nuclei range up to at least 10^{12} solar luminosities. The nuclei of a large number of normal galaxies emit at least $10^8 - 10^9$ solar luminosities in the infrared. These large amounts of energy cannot originate from the normal stellar component of these galaxies, and it has been suggested that the nuclei of all galaxies emit such energy by a common physical process (Kleinmann and Low 1970a). The exact nature of this process is mysterious and may be outside the domain of established physical laws. However, current theories center around two ideas:

1. the emission has a thermal origin and is caused by reradiation from dust surrounding an energy source;
2. the emission is nonthermal synchrotron radiation from a collection of separate sources.

Apparently, both processes are operating in the nuclei of external galaxies. For example, from scanning studies the Seyfert galaxy NGC 1068 was found to emit most of its 10μ radiation from an area 60 parsecs (~ 1 arc sec) in diameter (Becklin et al. 1973). This fact was interpreted as evidence for thermal reradiation from dust. However,

there is also evidence for 30 percent variation in the $10\ \mu$ flux on the time scale of two months (Rieke and Low 1972) and for a net polarization of this radiation (Knacke and Capps 1974). Although these latter observations are disputed (Jones and Stein 1975), they suggest the existence of small (~ 1 arc sec) nonthermal sources within the larger area of thermal emission. Variable, nonthermal radiation is also observed in the Seyfert galaxy NGC 4151 and in the quasar 3C 273.

Two other galaxies have been resolved and mapped at infrared wavelengths: NGC 253 and M 82. At $10\ \mu$, both objects contain extended (~ 10 -25 arc sec) sources (Kleinmann and Low 1970b), which have been interpreted as thermal emission from dust. However, in NGC 253 recent results by Rieke and Low (1975) indicate that a nonthermal component also exists.

In our galaxy, the infrared luminosity of the nucleus is comparatively low but because of its near location, high spatial resolution can be obtained. Using the scanning techniques previously discussed, Rieke and Low (1973) have published maps of the galactic center at 3.5, 5.0, 10.5, and $21\ \mu$ with a resolution of 5.5 arc sec. These maps show a complex of unresolved objects near the center. Many properties of these sources are explained by thermal reradiation from dust similar to that from galactic H II regions. Also, radio astronomers have discovered a nonthermal source (Sgr A) at our galactic center and recently resolved it into separate sources which seem associated with the infrared sources (Balick and Sanders 1974). At the very center of the galaxy an intense, unresolved ($\lesssim 0.1$ arc sec) radio source has been detected

whose physical nature is as yet unknown (Balick and Brown 1974). It is possible that both thermal and nonthermal processes are, or have been, at work in our galactic nucleus.

As was true for the infrared nebulae, progress in the understanding of infrared galaxies will be achieved by new techniques to map extended sources of higher resolution and to resolve discrete sources. This type of research will allow us to discover the distribution and nature of infrared sources both in our own galactic nucleus and in the nuclei of external galaxies.

It is important to understand the origin of infrared energy in these objects. An important test of the two current theories requires the measurement of angular sizes of the emitting regions in galactic nuclei. A small size argues against thermal emission from heated dust while a large size may preclude a single source of synchrotron radiation (Becklin et al. 1973). In terms of the second model, the more luminous galaxies may have more synchrotron sources since they have the largest and most frequent outbursts (Low 1970).

Because of the high infrared flux and similar energy spectra of many galaxies, it seems that all of them may emit infrared energy through the same physical process(es). Differences in variability, explosive behavior, and nonthermal flux among galaxies might be explained in terms of an evolutionary process which relates all galaxies. High spatial resolution studies may not only define the energy generating process but also provide maps of the nuclei in order to characterize this evolutionary trend.

Solar System Objects

Within the solar system, high resolution infrared studies can help to determine the physical sizes of satellites and asteroids and to map thermal emission from the major planets. For the satellites, accurate angular diameters are important quantities in determining densities which, in turn, help specify the chemical composition and evolution of these bodies. Similar arguments apply to the asteroids. In addition, direct measurement of asteroid sizes will provide a strong check of current, indirect methods to obtain this quantity (Chapman, Morrison and Zellner 1975). In principle, the shape of an asteroid and its rotational properties can also be deduced and then compared with the results from light curve methods (Gehrels 1971).

Overview of This Research

Previous sections of this chapter have demonstrated the need for higher spatial resolution in infrared astronomical observations. Since current techniques are limited mainly by diffraction and atmospheric seeing, a logical step forward would be to utilize interferometric methods. When faced with similar difficulties at visual and radio wavelengths, astronomers have found great success with this approach.

In the research described here, the goal has been to build a simple infrared spatial interferometer which could extend observational resolution by an order of magnitude using existing telescopes and could investigate atmospheric seeing. Chapter 2 presents the basic physics of this technique and outlines the various considerations which influenced construction of the interferometer. Chapters 3, 4, and 5

describe the details of the instrument's design, testing, and telescopic performance. Chapter 6 is the discovery section of this work since it describes the observational results concerning the atmosphere and several infrared stars. Chapter 7 discusses the achievements and limitations of this new technique and presents ideas for future improvements.

Although these initial efforts are confined to the determination of angular diameters of several bright stars, it should eventually become possible, at some infrared wavelengths, to perform high resolution mapping observations of rather faint sources by aperture synthesis techniques.

CHAPTER 2

SPATIAL INTERFEROMETRY: THEORY AND PRACTICE

Theoretically, the angular resolution of a telescope is limited only by the effect of diffraction from a finite aperture, so resolving power should increase as the aperture is enlarged. Practically, however, this expectation is unrealistic at visual wavelengths because of the severe blurring aspects ("seeing") of Earth's atmosphere.

In 1868, Fizeau proposed a simple technique to increase a telescope's resolving power and to decrease its sensitivity to atmospheric seeing. Ironically, only small, widely separated portions of the aperture are used and diffraction and interference remain the dominant physical mechanisms at work. In 1891, Michelson employed this technique to measure the angular diameters of planetary satellites. Subsequently, Michelson and Pease designed and built a telescopic instrument to resolve the "disks" of bright stars. In 1921, this device ("The Michelson Stellar Interferometer") was used to measure stellar angular diameters down to 0.02 arc sec. An excellent historical review of these pioneering efforts has been written by De Vorkin (1975).

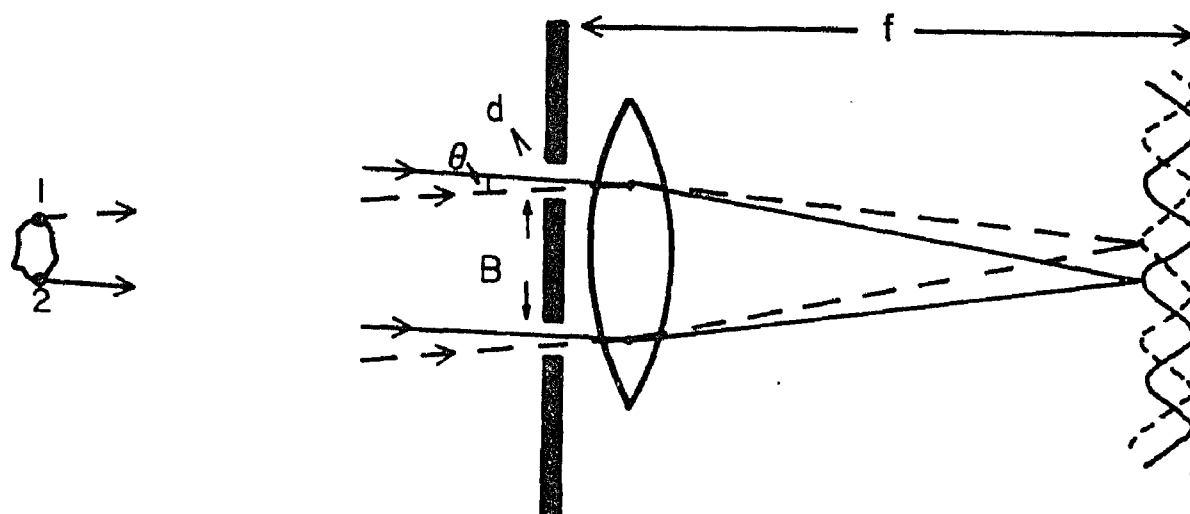
Between about 1940 and 1965, visual spatial interferometry lay rather dormant. However, the advent of modern technology has fostered improved instruments and yielded new astronomical results (Labeyrie 1970; Wickes and Dicke 1973; Currie, Knapp and Liewer 1974; Brown 1974).

The "amplitude" (Knapp 1974) and "intensity" (Brown 1974) interferometers are the current state-of-the-art at visual wavelengths. Other, more futuristic ideas can be found in the Woods Hole Summer Study on Synthetic Aperture Optics (1967). At radio wavelengths, where atmospheric seeing is less troublesome, Fizeau's idea has been amplified into the concepts of aperture synthesis (Fomalhont and Wright 1974). However, at infrared wavelengths spatial interferometry is just now being attempted (Johnson, Betz and Townes 1974; McCarthy and Low 1975), so, in light of Chapter 1, discoveries are waiting to be made.

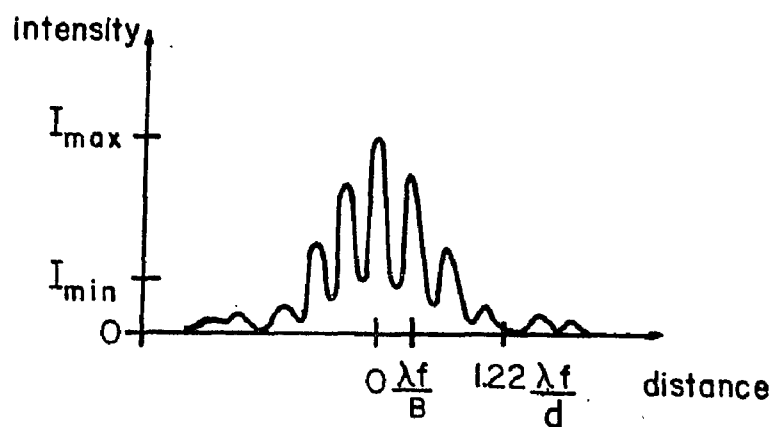
This chapter presents the general considerations which influenced the design and operation of an infrared spatial interferometer. We begin by examining the physics of the technique and continue with a discussion of atmospheric effects. Finally, some complications of operating at infrared wavelengths are discussed.

Physical Foundations

The physics of spatial interferometry is rooted in the complex theory of partial coherence (Born and Wolf 1959) but is simply exhibited in the classic Young's double slit experiment. In Young's arrangement (Figure 2.1a) partially coherent, quasimonochromatic light is incident on a screen which transmits light through two identical apertures whose separation, B , is called the baseline. The transmitted light is focused on a distant screen where Fraunhofer diffraction images from the apertures are superimposed and linear interference fringes form in the overlap region perpendicular to the baseline. The so-called "visibility"



(a)



(b)



(c)

Figure 2.1. Young's Double Slit Experiment

- (a) Experimental parameters
- (b) Observed fringe pattern from a partially resolved source
- (c) image, with fringes, as seen in focal plane

of the fringes is a sensitive indicator of the angular size of the illuminating source.

It is worthwhile to understand how the fringes are produced and what relationships exist between experimental parameters. Returning to Figure 2.1, consider illumination from a series of mutually incoherent point sources lying on the extended object between points one and two. Due to interference effects caused by the double aperture, light from each point source forms a sinusoidal fringe pattern on the screen (here diffraction is temporarily neglected). The "wavelength" or fringe width of this pattern is defined as

$$\text{fringe width} = \frac{f}{B_{\lambda}}, \quad (2.1)$$

where f is the distance from the aperture to the screen and B_{λ} is the baseline measured in wavelength units.

Since the point sources are incoherent, their separate fringe patterns add linearly to yield a net fringe pattern of the same frequency (Figure 2.1b). The visibility of this net pattern is defined as

$$V_o(B_{\lambda}) \equiv \frac{I_{\max} - I_{\min}}{I_{\max} + I_{\min}}, \quad (2.2)$$

here I_{\max} and I_{\min} are the maximum and minimum intensities in the pattern.

Visibility is a function of baseline measured in wavelengths; an illustration of this function appears in Figure 2.2. For a given source, as the baseline length is increased, visibility decreases

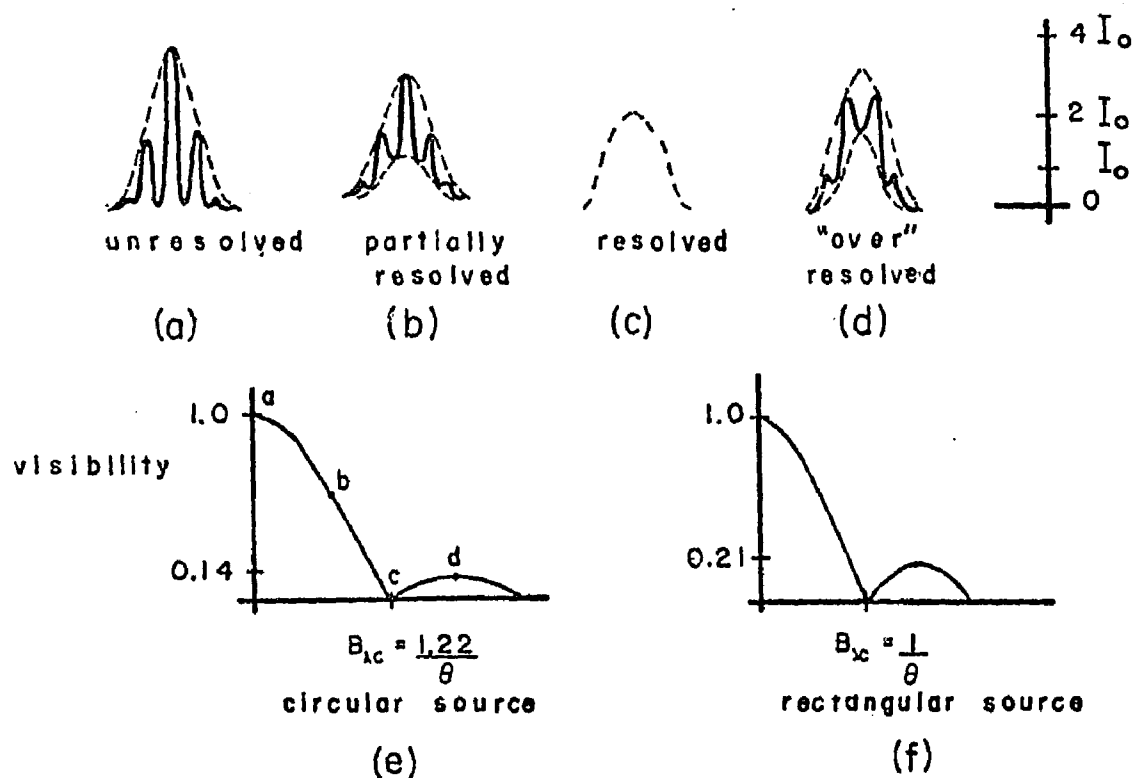


Figure 2.2. The Visibility Function

Parts (a), (b), (c) and (d) are examples of image intensity profiles observed at four different baselines. Parts (e) and (f) illustrate visibility functions for a uniform, circular source and a slit source. I_0 is the intensity emergent from each aperture in Figure 2.1.

toward zero where, by definition, the source is "resolved." The zero-visibility point can be used to compute an object's angular diameter, θ , from the equation

$$\theta = \frac{C}{B_{\lambda c}} \text{ radians,} \quad (2.3)$$

where $B_{\lambda c}$ is the critical value of baseline at this point. The quantity, C , is a constant having values of 1.0, 1.22, and > 1.22 for a slit, circular, or circular limb-darkened source, respectively. Figures 2.2e and 2.2f show the visibility versus baseline relationship for a uniform, circular source and for a slit source. It is interesting to note that a source can be "over" resolved since higher order maxima exist in the visibility function. The locations and shapes of these maxima can also be used to estimate the angular size and shape of a source.

Besides measuring the fringe pattern's visibility, one can also measure its phase. For example, a source with asymmetrical brightness distribution causes the central fringe to shift away from the peak of the diffraction pattern. This fact can be demonstrated by extension of the graphical procedures of Figure 2.1. Thus the phase contains information on the source's brightness distribution parallel to the baseline. Note, also, that the phase shifts 180° in alternate maxima of the visibility function.

Clearly, fringe visibility can be treated as a complex function whose real part measures fringe amplitude (equation 2.2) and whose imaginary part is the fringe phase. The relationship between this function and the intensity distribution across the source is known as the

van Cittert-Zernike theorem. In essence, it states that the complex visibility equals the normalized Fourier transform of the intensity distribution, as expressed below in one dimension,

$$V_o(B_\lambda) e^{i2\pi B_\lambda \delta} = \frac{1}{2I_o} \int_{-\infty}^{\infty} I(\phi) e^{i2\pi B_\lambda \phi} d\phi, \quad (2.4)$$

where δ is the fringe phase and $I(\phi)$ is the source intensity distribution; ϕ is an angular coordinate on the sky.

From the inverse Fourier transform,

$$I(\phi) = 2I_o \int_{-\infty}^{\infty} V_o(B_\lambda) e^{-i2\pi \delta B_\lambda} dB_\lambda, \quad (2.5)$$

which demonstrates that the intensity distribution can be recovered from a set of interferometric observations at different baselines, each of which samples a certain spatial frequency in the intensity distribution. To arrive at a unique answer, each observation must measure both V_o and δ . In order to determine the two-dimensional intensity distribution, similar measurements must be made at different orientations (position angles) of the baseline.

Unfortunately, it is difficult to measure δ even at radio wavelengths because the atmosphere induces its own phase shifts. As a result, fringe phase is almost never determined and the astronomer compensates by assuming a model source in order to fit a theoretical curve to the measured data (Swenson and Kellermann 1975).

Angular Resolution

The Michelson Stellar Interferometer is simply an adaptation of Young's experiment in which a conventional telescope replaces the lens in Figure 2.1a. This instrument will resolve (as defined in the previous section) a double star whose components have an angular separation $\theta = \frac{\lambda}{2B}$. This resolving power is a factor of 2.44 better than for a normal telescope according to the Rayleigh criterion! It is not obvious why the interferometer's resolution is superior even if the physical length of both instruments is identical. The following treatment offers an explanation which also illustrates why the interferometer seems less sensitive to atmospheric seeing.

The resolution of an instrument can be characterized by the spatial frequencies it transmits. For example, an interferometer with two tiny holes separated by a distance B is sensitive to a spatial frequency, $B_\lambda = \frac{B}{\lambda}$, in the observed object. Consider a larger, circular aperture. It may be envisioned as a collection of such hole-pairs with a variety of available spacings. Pairs with identical spacings contribute identical fringe patterns which add in phase regardless of their location on the aperture. Summation of these patterns over all allowed spacings yields the diffraction pattern of that aperture.

By utilizing only certain portions of the uniform aperture, it is possible to emphasize some spatial frequencies more than others. For example, even though some high frequencies are present, the effective response of a uniform aperture is concentrated at lower frequencies because most of its area is devoted to hole-pairs of smaller spacing. As discussed quantitatively by Code (1975) and

Young (1974), a central obscuration shifts this response toward higher frequencies by eliminating area devoted to the lower ones. An extreme case of such an annular aperture is the two element interferometer whose response is constrained to a narrow range of the highest frequencies available. Needless to say, the price paid for this "advantage" is a severe loss in collecting area.

Now consider a uniform aperture in the presence of atmospheric seeing. Ideally, at any allowed spatial frequency the fringe patterns from hole-pairs of identical spacing will add in phase. Each frequency will then have a certain fringe amplitude whose value depends on the redundancy of its hole-pairs over the entire aperture. However, since atmospheric turbulence distorts the incident wavefront nonuniformly across the aperture, very few fringe patterns add precisely in phase. Consequently, the amplitudes of certain spatial frequencies are reduced and instrumental resolution is degraded.

One way to alleviate this degradation is to reduce the phase cancellation by decreasing the redundancy of identical hole-pairs. The two aperture interferometer operates in this way so it should be and often is less sensitive to atmospheric seeing than its conventional counterpart.

Besides the factor of 2.44 improvement in angular resolution mentioned earlier, an interferometer can be used to infer the angular diameters of very small objects for which the zero-visibility point cannot be reached with available baselines. This improvement is accomplished by fitting a theoretical model source to existing data and then by extrapolating it to find the expected zero-visibility point.

Thus a spatial interferometer possesses the ability to increase angular resolution substantially beyond that available with normal telescopes.

Atmospheric Phenomena

Ironically, in travelling to Earth, starlight traverses distances of many light years only to have its precious information jumbled or destroyed a few miles or feet from the telescope. Acting as an inhomogeneous barrier, our atmosphere distorts incident plane waves into wrinkled (or "corrugated") wavefronts having bumps of variable amplitude and extent--much like the turbulent surface of a swimming pool. The inhomogeneities are thought to be temperature fluctuations in the form of moving "cells" whose sizes range from a few inches to many feet or kilometers. These cells distort starlight by refractive effects. The resulting telescopic phenomena are termed "seeing" and "scintillation"; several review articles have been written concerning them (Stock and Keller 1960; Meinel 1960; Meyer-Arendt and Emmanuel 1965). Scintillation describes the time variation of image intensity. Seeing is a vague term referring to the changing size, morphology, and position of an image. Both effects are now rather well understood theoretically (Young 1974).

Although Michelson's interferometer overcomes the major resolution limit imposed by the atmosphere on a uniform aperture, its usefulness is still severely impaired by seeing effects which cause rapid fringe motions of variable amplitude and frequency. It is important to understand the nature of these motions at visual wavelengths in order to anticipate the role they will play in the infrared.

As starlight passes through an atmospheric turbulence cell, it seems to suffer two important perturbations. First, its direction of propagation is altered ("wavefront tilts") and second, its phase is retarded relative to its nominal value ("phase delays"). According to the Kolmogoroff "law of turbulence" (Young 1971, 1974), a cell's refractive index changes in proportion to its size, so bigger cells will inflict larger tilts and delays. In addition, a wind will sweep a collection of these cells across the line of sight to the star so tilts and delays can change rapidly. To a telescopic observer, the stellar image will then appear to fluctuate in size, shape, and position in a manner dependent on wind velocity and telescope size.

In the interferometer wavefront tilts generally differ at each of the two apertures and the images appear to "dance" in the focal plane. Relative motion between images causes the degree of overlap to vary between 0-100 percent so that fringe amplitude will also vary even though visibility may remain constant if it could be measured at a frequency greater than that of the dancing. On the other hand, different phase delays at each aperture will shift the phase of the net fringe pattern; visually, an interferometric observer sees the fringes vibrating back and forth through some distance which is a measure of the total instantaneous phase difference (Breckenridge 1976). Clearly, visibility measurements must be obtained at a frequency higher than that of the phase delays or else fringes will appear "smeared" and the visibility value will be reduced.

The amplitude and frequency of tilts and delays can be estimated quantitatively from previous telescopic and interferometric observations

done at visual wavelengths. First of all, it should be noted that these quantities depend on atmospheric conditions (e.g., winds, weather systems), on site location (e.g., altitude, local weather patterns), and on the structure of the dome and telescope. Typically, wavefront tilts have amplitudes $\gtrsim 1$ arc sec and occur at frequencies from a few cycles per second to over 300 in bad seeing; these values follow from telescopic studies of stellar image size and motion. Phase delays are studied interferometrically. For example, Miller (1970) has used the fact that Michelson and Pease saw fringes to conclude that visual delays have amplitudes of 10-20 wavelengths ($\lambda \gtrsim 0.5 \mu$) and frequencies down to 5-10 wavelengths per second. Although higher frequencies ($>> 10-20 \lambda \text{ sec}^{-1}$) may exist, their amplitude is probably less than 0.5λ because, otherwise, Michelson and Pease could only have seen fringes on the fly.

The effects of tilts and delays are also important because they constrain the maximum aperture size which can be used without decreasing the fringe visibility. Clearly, the aperture should be small enough that incident wavefronts will be uniform in phase and tilt across the aperture. Equivalently, the aperture should be, at most, as large as a small turbulent cell. Otherwise, destructive interference (phase cancellation) can occur to suppress fringe visibility and perhaps to create distorted, nonlinear fringes. The critical size is undoubtedly dependent on atmospheric conditions. At visual wavelengths, on the basis of the well-known aperture effect of seeing, this size is typically ~ 10 cm. It can be shown (Fried 1966) that this size is

proportional to the $6/5$ power of wavelength, so in the infrared at a wavelength of $5\ \mu$ aperture sizes up to ~ 100 cm should be practicable.

All these atmospheric turbulence effects are quite time dependent. Their amplitude and frequency characteristics can change suddenly or gradually during a night of observing. For this reason, most visual spatial interferometers must observe standard stars (i.e., known point sources) to monitor and to provide data corrections for seeing effects. It should also be remarked that these effects are more severe at large zenith distances so best results will probably occur for observations taken during transit and near the zenith. Finally, seeing can also be created within the dome and telescope by turbulent air currents. These can be reduced or eliminated by proper ventilation and other precautions (Meinel 1960).

Atmospheric dispersion is another atmospheric effect which has some rather subtle and important consequences on spatial interferometry (Anderson 1920). Basically, the entire atmospheric layer disperses starlight into a short spectrum with the shorter wavelengths oriented toward the zenith. When the interferometer baseline is aligned perpendicular to the horizon, this spectrum decreases fringe visibility in the same way as does an extended source. The magnitude of this decrease depends on stellar zenith distance, observed bandwidth, and observed wavelength; a calculation of the importance of this effect in the infrared is presented in the next section.

Infrared Considerations

At infrared wavelengths, thermal radiation from the atmosphere and local environment ("background") overwhelms the apparent infrared brightness of most astronomical objects. Therefore, considerations of background elimination and instrumental sensitivity are fundamental in infrared astronomy. The general philosophy in this field is, first, to reduce the background received by a detector so that it can operate at highest sensitivity with low noise and, second, to provide background cancellation through beam switching techniques in order to detect sources which are buried in the background.

Because a Michelson stellar interferometer uses small apertures for coherence reasons, a significant amount of flux incident on the telescope primary is wasted, thereby seriously reducing the instrument's limiting magnitude. Thus, an infrared spatial interferometer should be designed to operate at the highest possible sensitivity with the lowest possible background, and it must incorporate techniques for background cancellation during measurements of fringe visibility.

The atmosphere is transparent to infrared energy only in certain wavelength regions ("windows") where absorptions from CO_2 , H_2O are comparatively weak. Infrared interferometers must operate within one of these windows and at a dry, high altitude site in order to increase the transparency within the window.

Exactly how atmospheric seeing influences the performance of an infrared spatial interferometer was largely unknown during the design of this instrument. No quantitative studies of infrared seeing

were available although the phenomenon of "sky noise" was known to occur especially at 10-20 μ and when using large fields of view. Although seeing effects inhibit visual interferometry, they are hardly noticeable in the radio region ($\lambda > 1$ mm) so it seems natural to expect that at least some portion of the infrared will also be well behaved. In fact, there are indications that seeing is clearly improved at 20 μ (Rieke 1975). Also, Low and Rieke (1974) have noted that the size of the seeing disk decreases with longer wavelengths beyond 0.5 μ . This type of behavior is expected because, as previously stated, uniformity of the wavefront should be proportional to the 6/5 power of wavelength. Therefore, the amplitudes and frequencies of fringe vibrations should decrease and large aperture sizes ($\gtrsim 100$ cm) are feasible. Nevertheless, the original infrared interferometer should be capable of operation at high frequencies ($\gtrsim 100$ Hz) in order to "freeze" the fringes if they are vibrating at these rates. A selection of aperture sizes should also be available.

Recently, some quantitative interferometric measurements of seeing at 10 μ were obtained by Johnson et al. (1974). Using two 28-inch apertures and a 5.5 meter baseline, they observed unexpectedly good fringe stability during visual seeing of 1 arc sec and at a large zenith angle. They stated that the amplitude of fringe motion is $\sim \frac{\lambda}{6} \approx 1.7$ on the average during a 20 second time period.

The importance of atmospheric dispersion in infrared interferometry can be evaluated in the following way. For a plane-parallel

atmosphere, the angle of refraction, R_λ , at a zenith angle, z , is given approximately as (Smart 1965)

$$R_\lambda = (n_\lambda - 1) \tan z \quad (2.6)$$

radians, where n_λ is the atmospheric refractive index. For a bandwidth of $\Delta\lambda$, the angular length of the dispersed spectrum is

$$D_\lambda(z, \Delta\lambda) = \left(\frac{\partial}{\partial \lambda} R_\lambda\right) \Delta\lambda = \left(\frac{\partial n_\lambda}{\partial \lambda}\right) \Delta\lambda \tan z. \quad (2.7)$$

Using refraction tables from Allen (1973) at a wavelength of 4μ with a 0.7μ bandwidth, we have

$$D_{4\mu}(z) \approx \left(\frac{0.1 \times 10^{-6}}{1.0}\right) (0.7) \tan z \quad (2.8)$$

$$D_{4\mu}(z) \approx (1.4 \times 10^{-2}) \tan z \quad (2.9)$$

arc sec. It can be shown that when the interferometer baseline is oriented along the direction of dispersion, the fringe amplitude of a point source is

$$V_o(\Delta) = \text{sinc}(\pi B_\lambda \Delta) \quad (2.10)$$

where $\Delta = D_{4\mu}(z)$. In the observations of this dissertation, $B \leq 100$ inches and $z \leq 60^\circ$, so the fringe amplitude is

$$V_o(\Delta) \geq 0.96. \quad (2.11)$$

In this work no corrections for dispersion are applied to the data.

CHAPTER 3

DESIGN OF THE INTERFEROMETER

Design Considerations

Several optical configurations are suitable for the design of an infrared spatial interferometer. The first and most obvious one is simply that of Young's experiment (Figure 2.1). Here a slotted mask could be placed over the image and some means of modulation would be used to transmit alternately the bright and dark fringes for detection. However, manufacture of this mask is difficult both because fringe size is small, being given as $\frac{\lambda f}{B}$ where B is very large, and because this size is variable as B is changed. Also, there is no attractive means of modulating the fringe pattern or the mask in order to measure I_{\max} , I_{\min} separately. For example, although one could alternately insert and extract in one beam a transparent sheet of material with a thickness of $\frac{\lambda}{2}$, this sheet would create an additional and variable source of infrared background radiation which would contribute unwanted signal and noise into the detector. Another disadvantage is that the two apertures are defined by a "hot stop," so again a detector sees an unwanted source of infrared background.

Figure 3.1 shows another optical configuration in which a beam-splitter is used to combine the two beams. Since the convergence angle between beams can be made very small or zero, fringe size becomes quite

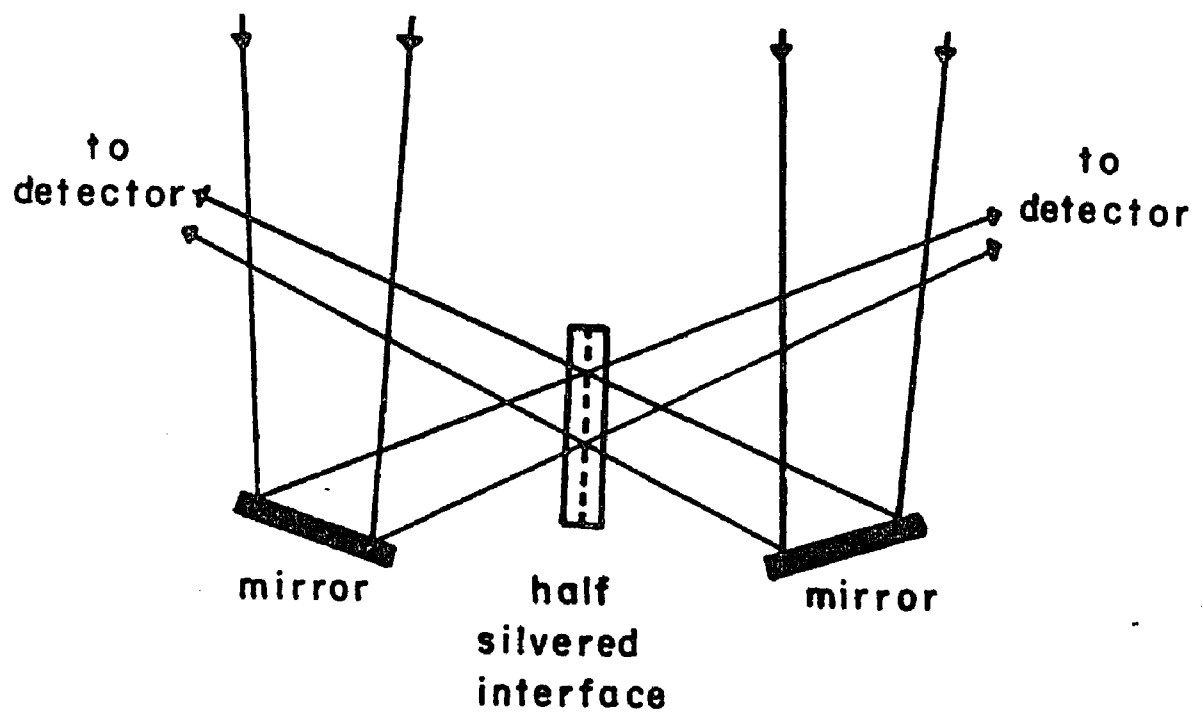


Figure 3.1. Beamsplitter Optics for a Spatial Interferometer

large and can even fill the entire field of view. Another advantage is that fringe size becomes constant; i.e., independent of the baseline length. Thus, a slotted mask is not necessary. However, this method suffers at least two disadvantages. First, beamsplitter efficiency is a function of wavelength. Therefore, in order to observe efficiently at several wavelengths, interchangeable beamsplitters are necessary. Second, this configuration wastes 50 percent of the available light although the use of two detectors would remedy this problem.

Another alternative is a four mirror geometry (Figure 3.2) originally proposed by Dr. F. Low. Here, after two circular beams are selected from the telescope's converging light cone, they are brought together, so that their edges touch, while converging to a common focus. This reduction in the mutual convergence angle enlarges the fringes. With this geometry, only 2.44 fringes are present within the Airy disk of the image and the physical width of the fringes is independent of baseline length. Fringe modulation is provided by translating one of the outer mirrors back and forth through a distance of $\frac{\lambda}{2}$ or by translating the center mirror a distance of $\frac{\lambda}{4}$ and back again. In addition, the central or "roof" mirror can be rotated slightly about a vertical axis in order to provide a star-sky photometric modulator. Mechanically, however, this four mirror configuration is more complicated than Young's setup because, for each mirror, tilting adjustments must be incorporated so that the images can be overlapped at the focus. Unfortunately, this method includes a hot stop to define the two apertures and requires a means of equalizing pathlengths in the two beams.

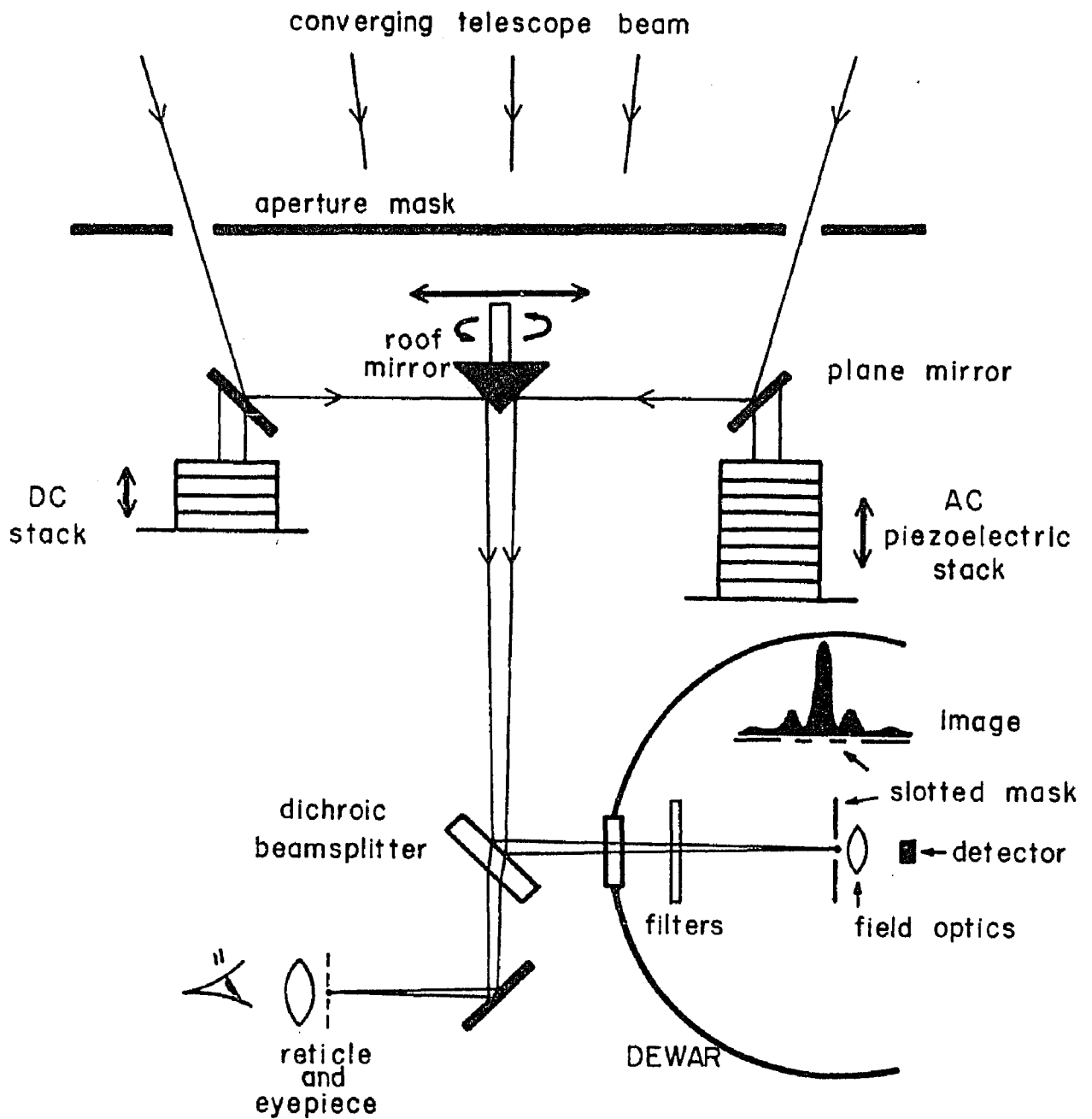


Figure 3.2. Schematic Diagram of the Spatial Interferometer

The four mirror setup was chosen for the interferometer because of its simplicity and versatility. These qualities were considered necessary for a prototype instrument which, from the outset, was intended to be simple, inexpensive, and able to determine atmospheric and other limitations to the technique. This philosophy led to a two aperture, four mirror interferometer to be used at the Cassegrain focus of existing, conventional telescopes. The aim of determining atmospheric limitations necessitated the use of several wavelengths, bandwidths, aperture sizes, baseline lengths, and telescope sites. Measurement of stellar angular diameters and shapes was expected (see Chapter 1) to require rather large (~ 60 inch) telescopes with the ability to rotate the baseline about the telescope's optical axis. Since many infrared stars emit their peak flux near 5μ , this wavelength was chosen for sensitivity reasons.

Principles of Operation

In its present form, the interferometer operates as follows (Figure 3.2). A mask selects two circular beams from the main telescope beam. Each of these is then reflected by two plane mirror surfaces so that the beams touch and converge together in a narrow, $\sim f/40$, cone to a focus where interference fringes form in the image. A dichroic beamsplitter separates the visual and infrared energy. The infrared image falls on top of a mask with three slots whose width and separation equal that of the fringes. Light from one set of fringes passes through the slots onto an InSb detector which, with the mask and selected filters, is cooled to liquid nitrogen temperature

inside a dewar. The visual image, which also displays fringes, is used for setting and guiding on visible stars, for monitoring visual seeing conditions, and for optical alignment.

Each element of the interferometer has its own special purpose mechanical adjustment. The outer plane mirrors (the "adjusting mirrors") tilt in two dimensions to overlap the two images in the focal plane. The central "roof" mirror can translate along the baseline to equalize the pathlengths in the two arms of the interferometer so as to achieve the "white-light fringe condition." This mirror must be positioned to within about half a wavelength because the instrument utilizes a large bandwidth (0.7μ at 5μ wavelength). The orientations of beamsplitter and detector system are also adjustable so that the detector's field of view will include the complete light cone coming from the roof mirror.

The interferometer incorporates several active features for measurement of fringe visibility. For example, the adjusting mirrors are mounted on stacks of piezoelectric crystals. One stack acts as a "fringe chopper" by introducing a path difference of $\frac{\lambda}{2}$ into one arm at a frequency of 40 Hz by means of an applied square wave signal. This motion produces a 180° phase shift in the interference pattern so the detector sees the adjacent set of fringes. Thus the fringe-chopped signal is a measure of fringe amplitude. Figure 3.3 shows the intensity profile of the image at each position of the chopper. The other crystal stack is operated in a DC mode and provides for initial alignment of the fringes on the slotted mask. Also, the roof mirror can be rotated rapidly through small angles; in this mode it serves as

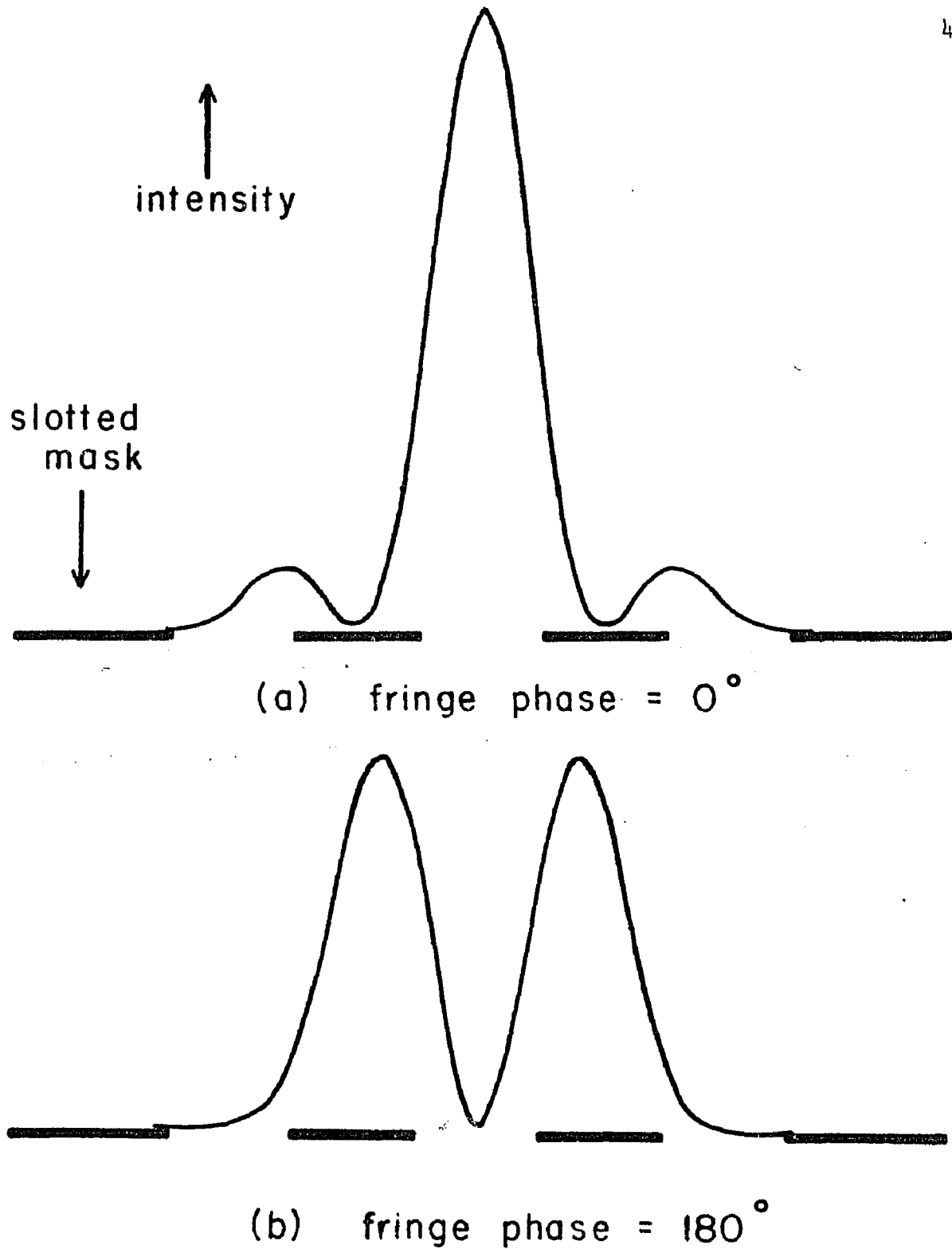


Figure 3.3. Fringe-Chopped Intensity Profiles

Parts (a) and (b) represent intensity profiles in a point source image for each position of the fringe chopper. These profiles are projected onto a slotted mask as in the actual instrument.

a "photometric chopper" to measure the flux from each beam. This photometric measurement is made independently for each beam; the sum effectively provides a zero baseline measurement of visibility which is needed to calibrate the fringe-chopped data. In addition, the photometric chopper is useful for monitoring the variability of astronomical sources and for locating invisible, infrared sources.

Electronically, the chopped signals from the detector are pre-amplified, filtered, amplified again, and FM recorded onto magnetic tape along with the chopper reference (sync) signal. In the laboratory, this tape is replayed through phase sensitive electronics and analyzed to deduce fringe visibilities. For real time analysis, signals are phase detected and displayed on oscilloscope or strip chart.

Actual observations consist of fringe and flux measurements for both extended and point sources; the ratio of these two measurements is called the "normalized fringe amplitude." Point source data must be obtained to convert this quantity into fringe visibility. For each extended source the goal is to measure visibility as a function of baseline, thereby deriving a visibility curve from which angular diameter and shape information are extracted. Different baselines can be selected either by using different sized telescopes or by changing the aperture separation on the mask. Observations are not necessarily limited to a wavelength of 5μ ; with only small modifications, mainly to the detector system and the aperture mask, the interferometer can obtain data throughout the infrared spectral region.

One peculiarity of the interferometer is that it is most easily operated on telescopes whose f-ratio is about $f/13$. This

restriction is imposed both by the four mirror geometry which supplies an upper limit on the f-ratio and by the interferometer's physical length (~ 22 inches) which supplies the lower limit. For example, on the Steward Observatory 90-inch telescope the f/9 focus cannot be lowered to the proper location in the interferometer without vignetting the light beam. However, additional Cassegrain optics can be employed to convert f/9 into about f/14 and at the 90-inch telescope, such a "beam converter" has been used as an interface between telescope and interferometer. Figure 3.4 is a photograph of the interferometer and beam converter mounted to the 90-inch telescope.

The remainder of this chapter gives detailed descriptions of the various mechanical, optical, and electrical systems of the interferometer. Wherever applicable, tolerances are placed on the design of various components and are explained in the text; these are summarized in Table 3.1 and are reexamined in Chapter 5 when atmospheric effects are introduced.

The Stage

The heart of the interferometer is called "the stage" (Figure 3.5). It is a half-inch thick aluminum block supporting the main optical elements, modulators, and aperture mask. The entire block is fastened to the main mounting plate of the interferometer and is designed to flip in and out of the main telescope beam. During operation, the stage is firmly clamped to the mounting plate and cannot be affected by flexures of the interferometer's housing. This overall

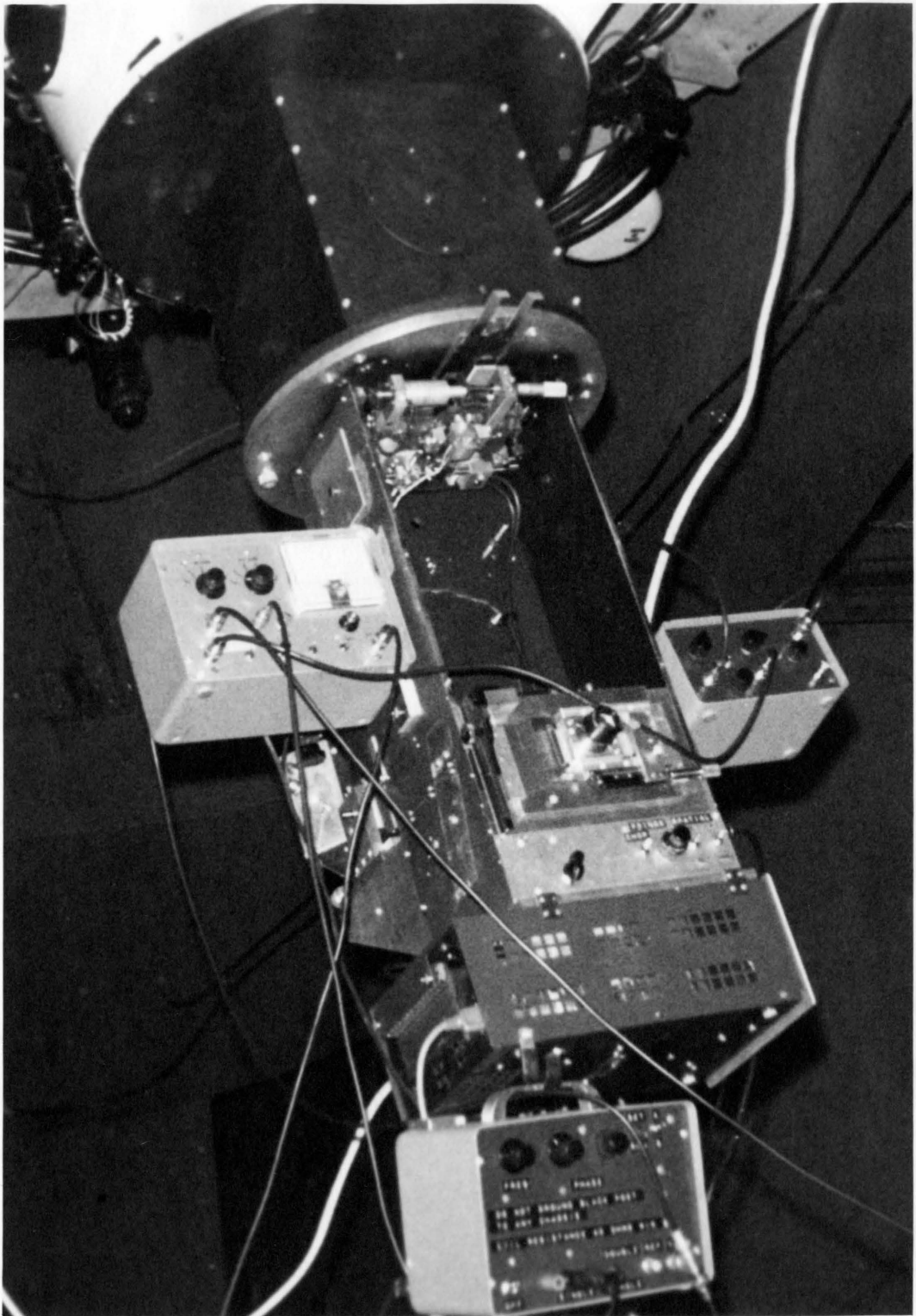


Figure 3.4. The Interferometer Mounted on the 90-Inch Telescope

The "stage" is visible just below the interferometer's mounting plate which is attached to the beam converter.

Table 3.1. Instrumental Tolerances Required for Operation During Ideal Atmospheric Conditions

$\lambda = 5 \mu$, $B = 50$ inches, $f = 20.8$ inches, $d = 0.25$ inch

	<u>Expression</u>	<u>Result</u>
Requirement: achieve and retain alignment of zero-order fringe on slotted mask		
<u>Mechanical Tolerances</u>		
1. displacement of stage components along baseline		
a. relative shift between adjusting mirrors	$\lambda/2$	2.5μ
b. shift of roof mirror	$\lambda/4$	1.3μ
2. resolution in roof mirror translation	$\lambda/4$	1.3μ
3. angular stability of telescope optics	$\lambda/2B$	0.4 arc sec
<u>Operational Tolerances</u>		
1. telescope pointing resolution	$\lambda/2B$	0.4 arc sec
2. telescope tracking error	$\lambda/20B \div 15 \text{ min}$	$4 \times 10^{-5} \frac{\text{arc sec}}{\text{sec}}$

Requirement: achieve a maximum reduction of ~ 10 percent in normalized fringe amplitude; efficient use of instrument		
<u>Mechanical Tolerances</u>		
1. dimensional error in slotted mask	$0.1\lambda f/2d$	0.02 mm
<u>Operational Tolerances</u>		
1. image overlap error	$\sim 10\%$	---
2. touching condition error at roof mirror	----	1 mm
3. fringe chopper throw error	$\sim \lambda/15$	0.3μ
4. telescope setting requirement	----	$\sim 10 \text{ arc sec}$

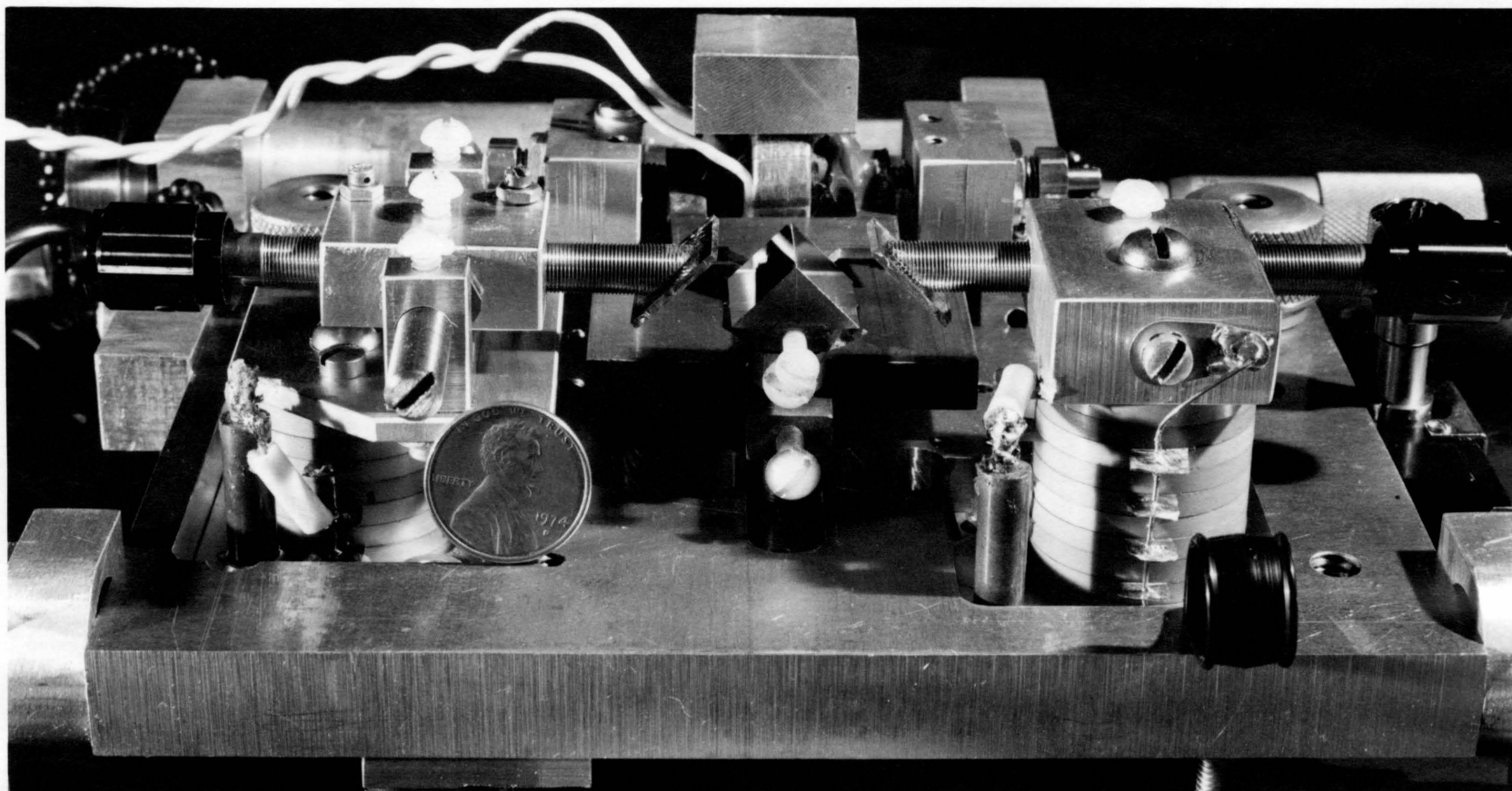


Figure 3.5. The Stage

Visible in this oblique view are the adjusting and roof mirrors at center; the piezoelectric crystal stacks at the sides; the photometric chopper above the roof mirror and the micrometer at the top right corner which translates the roof mirror. In this inverted view, the aperture mask lies underneath the large metal plate and telescope light is incident from below.

design represents an effort to stabilize the optical elements, which will now be discussed individually.

Aperture Mask

This mask provides a means of selecting various sized apertures and baselines during observations. In the original design of the interferometer several values of each could be chosen by manipulating a translation device supporting the aperture mask. However, it was discovered that atmospheric seeing did not usually degrade coherence of the $5\ \mu$ wavefront over the range of aperture sizes employed (4-14 inches). Therefore, subsequent measurements have been made only with the largest convenient apertures; i.e., 0.25 inch holes on the mask. On the other hand, use of the mask as a baseline selector has proven very useful. On a given telescope, two values (full and half spacings) of baseline are normally used during observations.

As noted earlier, this method of defining two apertures allows unwanted infrared background radiation to be received by the detector. A more optimum technique is desired; one possible idea is discussed in Chapter 7.

Adjusting Mirrors

The outer two plane mirrors in Figure 3.2 accomplish four types of alignment which require special adjustments of the mirrors themselves. These adjustments are as follows:

1. The mirrors must bring the light beams together at the roof mirror so that the beams touch while converging to a common focus. This "touching condition" is important because if the

beams do not touch but are separated by say 1 mm, then the resulting fringes will be 20 percent undersized, causing approximately a 20 percent decrease in the amplitude of the fringe-chopped signal. To stay within this guideline, each mirror must be able to raise and lower the vertical level of its reflected light beam by ≤ 0.50 mm.

2. The mirrors must adjust the overlap of the beams in the focal plane. Therefore, at least one mirror must be adjustable in two orthogonal directions. If the overlap is not perfect, then the amplitudes of both flux and fringe signals will be decreased somewhat. However, small amounts of overlap reduction are not crucial because atmospheric seeing causes overlap variations anyway and because measurements are always made relative to a point source which would contain the same percentage error. Therefore, even during ideal seeing conditions, an overlap reduction of ~ 10 percent of the image size should be tolerable. For 0.25 inch apertures on the slide, the mirrors should be able to center images to within 0.1 mm.
3. The mirrors must be able to change horizontal position to allow for observations at other baselines.
4. The mirrors constitute the basis of the fringe chopper and of a sensitive method of fringe alignment. During operation the piezoelectric stacks supporting these mirrors must be capable of translating through distances of $\frac{\lambda}{2}$ and $\lesssim \frac{\lambda}{4}$, respectively.

The following design satisfies all these requirements. Each mirror is fastened to a 45° plane formed on the end of a $\frac{1}{4}$ inch-56 thread, brass screw. This screw mates with a threaded aluminum piece which is rigidly mounted on a stack of piezoelectric crystals. To reduce "play" in the screw movement, a small nylon setscrew tightens against the brass shaft. By rotating the screw several turns, each mirror can be translated horizontally to satisfy the first and third requirements above. A smaller angular rotation about the screw's axis provides one of the two orthogonal tilting motions needed for the second requirement. Since the screw has 56 threads per inch, the height of each mirror's reflected beam can be changed in 0.50 mm increments as required. Note that using the screw's angular rotation to adjust overlap will not result in a significant change in the touching condition.

The left plane mirror possesses an additional tilting movement: it rotates about an axis perpendicular to the plane of Figure 3.2 in order to provide an overlap adjustment along the baseline direction. In this case, the brass screw is mounted like the declination bearing of a fork type telescope. It can be rotated by manipulating two push-pull screws, each on an opposite side of the bearing. Experience at the telescope has revealed that both adjusting mirrors should have this form of adjustment in order to overcome certain problems associated with the relative alignment between telescope and instrument. All the adjustments described here are performed by hand.

It remains to discuss the piezoelectric stacks controlling fringe chopping (the AC stack) and fringe alignment (the DC stack).

Because of their uniqueness, the stacks are described in Appendix A, where the details of design, operation, and testing can be presented in full.

Roof Mirror

The roof mirror accomplishes three tasks. First, it helps to establish the touching condition as discussed earlier. Second, it can be translated between the adjusting mirrors to achieve equal paths in the two arms of the interferometer. Third, it is part of the photometric chopper which allows measurement of the flux from each beam.

The tolerances placed on this mirror's translation and stability are some of the most stringent conditions placed on any element of the interferometer. For example, because a 0.7μ bandwidth is employed for observations, interference fringes will appear only after the so-called "white-light fringe condition" is achieved. Specifically, the roof mirror must be able to translate in increments less than half of the coherence length (Δl) of the observed radiation:

$$\Delta l = c\Delta t \sim \frac{c}{\Delta \nu} = \frac{\lambda^2}{\Delta \lambda} . \quad (3.1)$$

Therefore, for $\lambda = 5 \mu$, $\Delta \lambda = 0.7 \mu$, we find that $\Delta l = 36 \mu$. However, this is only a "ballpark" requirement because the real goal is to center the zero-order fringe on the slotted mask. Thus the mirror must be able to move separate fringes across the mask by translating in

increments of $\frac{1}{2} \left(\frac{\lambda}{2}\right)$. This is a tolerance of about one micron at $\lambda = 5\mu$. The roof mirror's stability should also remain within this tolerance even after the photometric chopper has been operated.

The mirror itself is a home built, aluminized, glass prism. In size the prism is square with a 0.6 inch base and has an apex angle of 90° . It was made by epoxying together two 45° plate glass surfaces which were selected on the basis of interferometric tests.

The photometric chopper rotates the roof mirror through small angles about an axis perpendicular to its base. The mirror is mounted on the end of a $\frac{1}{4}$ inch-56 thread brass screw which rotates in a threaded bearing. Above the bearing, the other end of the screw is clamped to the shaft of a "tuning fork." A small ($\sim \frac{1}{4}$ inch diameter) cobalt-samarium magnet is fastened on the inside of each fork arm with the magnetic poles oppositely oriented. Between the arms, a Ledex solenoid coil is firmly anchored in position. In operation, the coil conducts a ~ 40 volt square wave; thus the magnets are alternately pushed and pulled, thereby oscillating the screw. Adjustable stops limit the angular rotation ("throw").

The chopper has an unusual beam pattern consisting of three collinear "images." At one extreme of chopper rotation, the individual beams are separated and at the other extreme, they overlap; the latter is the central image and contains the fringes. This beam pattern has proven useful in locating invisible sources.

The entire chopper mechanism is fixed to a translation stage which moves against a loaded spring under action of a micrometer. This

arrangement provides the means for path equalization and can achieve the required tolerance.

In retrospect, this chopper has proven to be simple and reliable. Its operation does not destroy the accurate positioning of the roof mirror; in fact, it is possible to detect the presence of fringes during operation. Even though the chopper operates frequently during a night of observing, all optical elements seem to remain stable.

Beamsplitter

The beamsplitter serves two purposes. First, its dichroic characteristic separates visual and infrared energy, thus permitting independent observation of visual light for purposes of alignment and observation. Second, it acts as an alignment device to project infrared energy into the dewar. For the latter reason, the beamsplitter is mounted on two independent axes which can be adjusted to send the reflected light beam in the proper direction. However, this method is only the coarse adjustment because it alone does not ensure that the incoming infrared signal travels exactly along the optical axis of the detector system. An additional adjustment is necessary to place all the infrared energy on the detector. This fine alignment is achieved by small changes in the dewar's mounting orientation.

Dewar and Detector Systems

The infrared detector and its associated optical elements are mounted inside an Infrared Laboratories HD-2 dewar and cooled to liquid nitrogen temperature ($\sim 77^\circ\text{K}$). The dewar is equipped with a 3-position

filter slide and an 8-position focal plane aperture wheel so that observations can be made at wavelengths of 2.2, 3.5, and 5.0 μ using different slotted masks for fringe detection.

Two different InSb detector systems have been used. System-one, provided by Dr. G. Rieke, was a wide beam system used for observations in Spring 1975. A more optimized system with a much narrower beam was assembled by the author in the Fall 1975. At a wavelength of 5 μ both versions operated with a bandwidth of 0.7 μ , where the "cut-on" at 4.5 μ is determined by the atmosphere and the "cut-off" at 5.2 μ is determined by the InSb response.

System-One

This was the original detector system. It employed an InSb photovoltaic detector which was illuminated by a cooled, BaF_2 field lens and was baffled to accept an f/13 cone of incident radiation. The detector was purchased from Barnes Engineering Company; it had an internal resistance of 4.4×10^8 ohms and an N.E.P. of 2.3×10^{-14} watts/Hz $^{\frac{1}{2}}$ at a wavelength of 5 μ . A LiF_2 window and an externally mounted preamplifier were also provided.

Because the f/13 beam from the dewar was about three times larger than the f/40 cone of incident energy from the roof mirror, this system was operated with an unnecessarily large infrared background. Although this aspect reduced the interferometer's sensitivity, it was beneficial from the standpoints of convenience (the system had already been built) and of ease of alignment (the dewar was simply bolted to the back of the interferometer). However, as soon as the interferometric

technique yielded its first astronomical measurements, it was clear that an obvious step forward would be to improve the detector system by narrowing its acceptance cone and by installing a more modern detector.

System-Two

The new system incorporates a modern InSb detector with improved cooled optics and a low noise preamplifier. The detector was purchased from Santa Barbara Research Corporation. Its measured characteristics include an internal resistance of 1.5×10^9 ohms and an N.E.P. at 5μ of 1.8×10^{-15} watts/Hz $^{\frac{1}{2}}$. The original field lens has been replaced by a silicon, f/2 field mirror so that the detector's field of view is f/39. This improvement leads to a factor of three reduction in background photon noise. The new preamplifier follows the design of Hall et al. (1975); it allows for better drift compensation and has lower noise characteristics.

Alignment of the dewar with respect to the interferometer has now become a more complicated problem. Excellent alignment is achieved when the detector's acceptance cone is centered on the roof mirror and includes the two beams of incoming starlight. This situation insures that the detector sees a minimal amount of background emission from high emissivity, room temperature surfaces. The main contributor to background radiation will be the aperture mask, as mentioned earlier. To achieve this degree of alignment, the dewar is mounted so it can pivot independently about the detector in two axes. This method

constitutes the fine alignment discussed in connection with the beam-splitter.

Slotted Masks

The infrared focus occurs on top of an aperture wheel containing selectable slotted masks. Each mask is designed to transmit only one set of fringes within the Airy disk of the image and each consists of a circular aperture with three slots whose size and separation equal the calculated size of the fringes. The Airy disk diameter and fringe width are easily derived from the relations $2.44 \frac{\lambda f}{d}$, $\frac{\lambda f}{d}$, respectively, where f is the distance (20.8 inches) from the aperture mask to the focus and d is the diameter of the aperture.

Slots are made by gluing metallic strips over the circular apertures with General Electric varnish. In order to make the slots parallel and of proper size this process is performed under a microscope which is equipped with a fine lined reticle in one eyepiece. It is an easy task to achieve ≤ 5 percent error in the slot size; this error results in a ~ 5 percent decrease of normalized fringe amplitude. The metallic strips can be made of almost any material; to date, selected paper clips, integrated circuit leads, and flattened copper wire have been used successfully.

Although the mask is a necessary feature for fringe detection in this interferometer, its very presence causes a 49 percent loss in the photometric signal compared to that using an identical circular aperture with no slots. In addition, certain aspects of alignment are rendered more difficult. For example, the technique of centering a

stellar image on the mask by moving the telescope to maximize its photometric signal is no longer as sensitive and as clear-cut because the mask obstructs a significant portion of the available energy. Clearly, an alternate mirror arrangement for the interferometer is preferred if it could reduce the mutual convergence angle of the two beams to zero, thereby creating only one fringe over the entire field. However, such an arrangement has not been found. As mentioned at the start of this chapter, beamsplitters can achieve this situation but they have other disadvantages.

Visual Focus

After traversing the beamsplitter, visual starlight is reflected by a plane mirror so that it focuses on a fine lined reticle which is observed by eye through an eyepiece. The reticle and eyepiece are mounted together on a mechanism which can translate in two independent, orthogonal directions. This feature is used to place the reticle's center at the apparent location of the detector. The visual focus is important not only for setting the telescope accurately on visible stars, but also for monitoring seeing conditions and for aligning optical components of the interferometer and telescope. The latter aspect is treated in detail in Chapter 5.

Telescopic Requirements

The telescope is an integral part of the interferometer. It is important not only because of its large aperture which determines the baseline, but also because it can be pointed to a high degree of accuracy and because it can track this position at the sidereal rate.

Ideally, once the interferometer has been aligned the telescope should be able to center the zero-order fringe on the slotted mask to within half a fringe width (the remaining fine alignment can be performed by the DC stack) and it should be able to hold its position to within a small fraction of a fringe during a ~ 15 minute period. Therefore, the telescope must point to within an angle of $\frac{\lambda}{2B}$ and track to within an angular rate of $\sim \frac{\lambda}{20B} \div 15$ minutes. Clearly, the tolerance becomes more severe as the baseline, B , is increased; for a baseline of 50 inches these criteria become 0.4 arc sec and 4×10^{-5} arc sec/sec, respectively. These remarks are prefaced by the word "ideally"; they assume that the interference pattern will remain stable in position--at least during a 15 minute interval so that integration of the signal can take place. However, as Chapter 5 will show, this situation is not present in reality because of atmospheric fluctuations and the tolerances quoted above are unnecessarily stringent under normal conditions.

The telescope should satisfy some additional requirements. First, it should be capable of setting to within a few arc seconds of the desired coordinates so that invisible stars can be found quickly. Second, it should be equipped with a rotatable position angle bearing so that the interferometer can pivot around the optical axis. Third, to achieve highest sensitivity the telescope should present a small infrared background to the detector; e.g., the spider arms supporting the secondary mirror should be as thin as possible.

The Beam Converter

As mentioned in an earlier section, the large physical length of the interferometer precludes its use on telescopes of small focal ratio. On the Steward Observatory 90-inch telescope this problem was solved by using a beam converter as interface between the instrument and telescope. The converter, as originally designed by Dr. H. Johnson, utilized Cassegrain optics to convert $f/9$ into $f/14$. When focused within the interferometer, the outgoing beam became $f/16$. Although this device enabled the 90-inch telescope to be used, it also presented some new alignment problems, for now the train of optical elements was two telescopes in series with an interferometer!

In the Fall of 1975, the converter was reconfigured. Both mirrors were given new mounting mechanisms so they could be more easily adjusted in position and orientation. In addition, the distance between the mirrors was decreased so the new focal ratio became $f/13$. This last change was made so that very few alignment changes would be required in moving the interferometer between the 61-inch ($f/13.5$) and 90-inch telescopes and also so that the detector's field of view would not come as close to some high emissivity surfaces within the converter.

Electronics

This section describes the essential electronic features of the interferometer's operation. Electronic methods of data analysis are discussed in Chapter 5. Figure 3.6 gives a schematic electrical circuit diagram for the entire instrument.

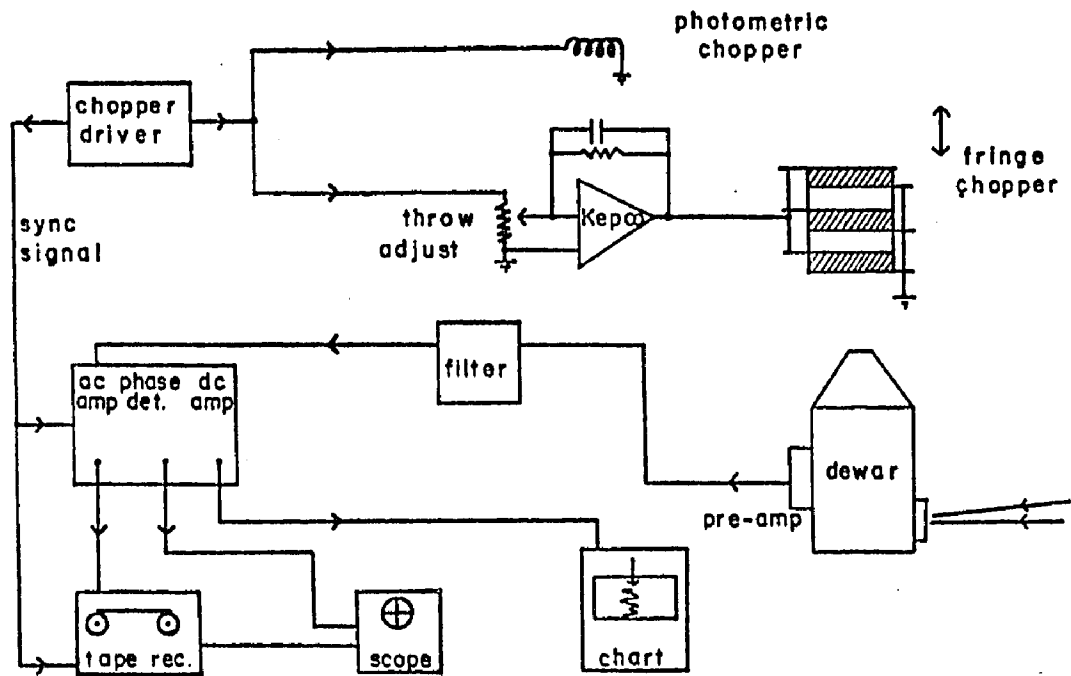


Figure 3.6. Schematic Diagram of Interferometer Electronics

The driving signals for both choppers originate in a device which generates a low voltage (~ 40 volt) square wave whose frequency and phase can be adjusted between 0-40 Hz and 0-360°, respectively. In the photometric chopper, this signal is applied directly to the coil. In the fringe chopper, it becomes the input to a high voltage operational power supply (Kepco OPS-2000) whose output (0-2000 volts) drives the piezoelectric crystals. The throw of this chopper is controlled by varying the gain of the power supply. The alignment crystal stack is operated in a DC mode with a different high voltage power supply. Generally, the fringe chopper operates at 40 Hz, the photometric chopper at 20 Hz, and the DC stack serves no useful purpose in typical seeing conditions.

During normal operation, the detector signal is preamplified, filtered, amplified again, and finally FM recorded on magnetic tape along with the chopper driver's reference signal by a Precision Instrument tape recorder (model PI-6100). For real time inspection the detector signal is also phase-detected and displayed on a strip chart recorder and on a two channel oscilloscope. This presentation enables the observer to estimate observational results and to evaluate the effects of atmospheric seeing.

CHAPTER 4

EXPECTED INSTRUMENTAL RESPONSE; LABORATORY TESTS

This chapter is divided into two parts. The first three sections describe some expected characteristics of instrumental response; the last two sections deal with laboratory tests of instrumental performance. There are several reasons for treating these topics. First, the reader will gain physical insight into the interferometer's behavior and operation, certain aspects of which are not obvious at first sight. Second, this treatment provides some criteria for evaluating reliability and performance of the instrument. Third, it is important to prove that the interferometer can measure angular diameters accurately under simulated telescopic conditions.

Interferometric Magnification

It is instructive to compare the image properties obtained from Young's double slit with those obtained from the four mirror configuration. In both cases, the size and scale of the diffraction envelope (Airy disk) are determined by the focal length of the lens or telescope and by the aperture size. However, the fringe scale is determined by the mutual convergence angle between beams and is not the same in both cases.

It is easy to calculate the number of fringes which should be visible within the Airy disk: merely divide the angular diameter of

the Airy disk by the angular width of each fringe. In Young's experiment with monochromatic radiation, this number is

$$2.44 \frac{\lambda}{d} \div \frac{\lambda}{B} = 2.44 \frac{B}{d} \text{ fringes.} \quad (4.1)$$

Note that it is directly proportional to the baseline length.

However, in the four mirror geometry the touching condition of the two beams causes a constant number (2.44) of fringes to be seen, independent of baseline; this follows from the relation

$$2.44 \frac{\lambda}{d} \div \frac{\lambda}{d} = 2.44 \text{ fringes.} \quad (4.2)$$

Because the fringes in both geometries must have the same angular size if the baselines are identical, the four mirror setup has magnified the fringe scale by a factor $\frac{B}{d}$. Consider a specific example. If B , d equal 50, 5 inches, respectively, then the interferometer's visual (0.5 μ) image contains 2.44 fringes whose angular width is 0.08 arc sec each. The angular diameter of the Airy disk is 2.0 arc sec. If the telescope's plate scale is 10 arc sec/mm, then the Airy disk is seen at this scale but the fringe scale is $10 \frac{d}{B} = 1$ arc sec/mm.

A second characteristic of Young's experiment is that as the source is moved parallel to the baseline, the image also moves and retains its set of fringes. In fact, for a point source, the zero-order fringe remains centered in the image. On the other hand, in the four mirror geometry white-light fringes are seen only when the source is in a specific location. To understand the latter phenomenon, consider the previous example again and let the source be located at this

specific spot. If the source moves along the baseline through 1 arc sec, then the Airy disk moves 0.1 mm in the focal plane whereas the zero-order fringe moves 1.0 mm. Now, if the image were observed in monochromatic light, fringes would still be visible; they would just be of higher order. However, white-light has a bandwidth of $\sim 0.3 \mu$ so its coherence length is considerably smaller and the highest order fringe which can be seen is given by

$$n = \pm \frac{\text{coherence length}}{\lambda} = \pm \frac{\lambda}{\Delta\lambda} \approx 2. \quad (4.3)$$

Therefore, the size of the coherence region is only ~ 0.3 arc sec, so the source cannot be moved more than this amount if fringes are to remain visible.

This aspect of the four mirror interferometer can be very helpful in aligning the instrument. For example, the zero-order fringe should be centered on the slotted mask. However, when the instrument is first mounted to a telescope, fringes will probably be seen some distance away from that location. This means that the path difference between the two beams must be adjusted. To do this, the roof mirror is translated some small amount along the baseline. Looking through the eyepiece, the observer then finds the new fringe location by moving the stellar image. Thus, a simple iterative procedure can be used to align the zero-order fringe on the slotted mask.

This discussion can now be applied at infrared wavelengths. Let $\lambda, \Delta\lambda$ equal 5, 0.7 μ , respectively. From equation 4.3, about 14 total fringes can exist but only 2.44 are observed within the Airy disk

because of the magnification factor. If the diffraction envelope were to enlarge (perhaps because of poor seeing), then more of these allowed fringes would be "seen."

Beam Patterns

An instrument's response can be characterized by its beam pattern which is simply the variation of received signal with angle away from the optical axis. Because the interferometer can be operated in two different modes, two distinct beam patterns are identified and discussed.

The pattern in the photometric mode is expressed analytically by the following relation

$$I(\theta) = I_0 \Delta v \left[\frac{2J_1(\pi d_\lambda \sin\theta)}{\pi d_\lambda \sin\theta} \right]^2 \left[1 + \frac{\sin(\pi B_\lambda a \sin\theta)}{\pi B_\lambda a \sin\theta} \cos(2\pi B_\lambda \sin\theta) \right], \quad (4.4)$$

where $J_1(x)$ is a first-order Bessel function. This expression gives the intensity profile observed in a scan along the baseline through the center of a point source image.

As an example, choose the following parameters:

B = baseline = 50 inches,

d = aperture diameter = 8 inches,

$$a = \frac{\Delta\lambda}{\lambda} = \frac{\text{bandwidth}}{\text{wavelength}} = \frac{0.7}{5.0} = 0.14,$$

$I_0 \Delta v$ = total single beam intensity $\equiv 1.0$.

Figure 4.1a shows the resulting beam pattern in the form of observed intensity from the source versus θ , the angle of the source from the instrument's optical axis. This pattern would be approximately observed at the telescope if a point source were scanned along the baseline and the photometric chopper were operating with both beams at the same time. If the interferometer is misaligned so that an extra path difference is present in one arm, then all fringes will be shifted to one side of the diffraction envelope.

At longer baselines, the angular size of each fringe decreases and the beam pattern will show the set of fringes to be more concentrated together near the center of the diffraction envelope. Because of this effect, the setting and tracking requirements on telescope motions become more stringent if the zero-order fringe is to be properly aligned at all times. Note that the number of fringes is independent of baseline being determined only by the ratio $\frac{\lambda}{\Delta\lambda}$.

Figure 4.1b shows the beam pattern in the fringe-chopping mode; this picture is based on the following equation using the same parameters previously mentioned:

$$I(\theta) = 4I_o \Delta\nu \left[\frac{2J_1(\pi d_\lambda \sin\theta)}{\pi d_\lambda \sin\theta} \right]^2 \frac{\sin(\pi B_\lambda a \sin\theta)}{\pi B_\lambda a \sin\theta} \cos(2\pi B_\lambda \sin\theta). \quad (4.5)$$

Compared to the previous figure, this profile is symmetric about the zero-signal axis because the DC term in equation 4.4 has been eliminated by fringe-chopping. Equivalently, one can say that this mode of operation measures only that incident radiation which is coherent and produces interference.

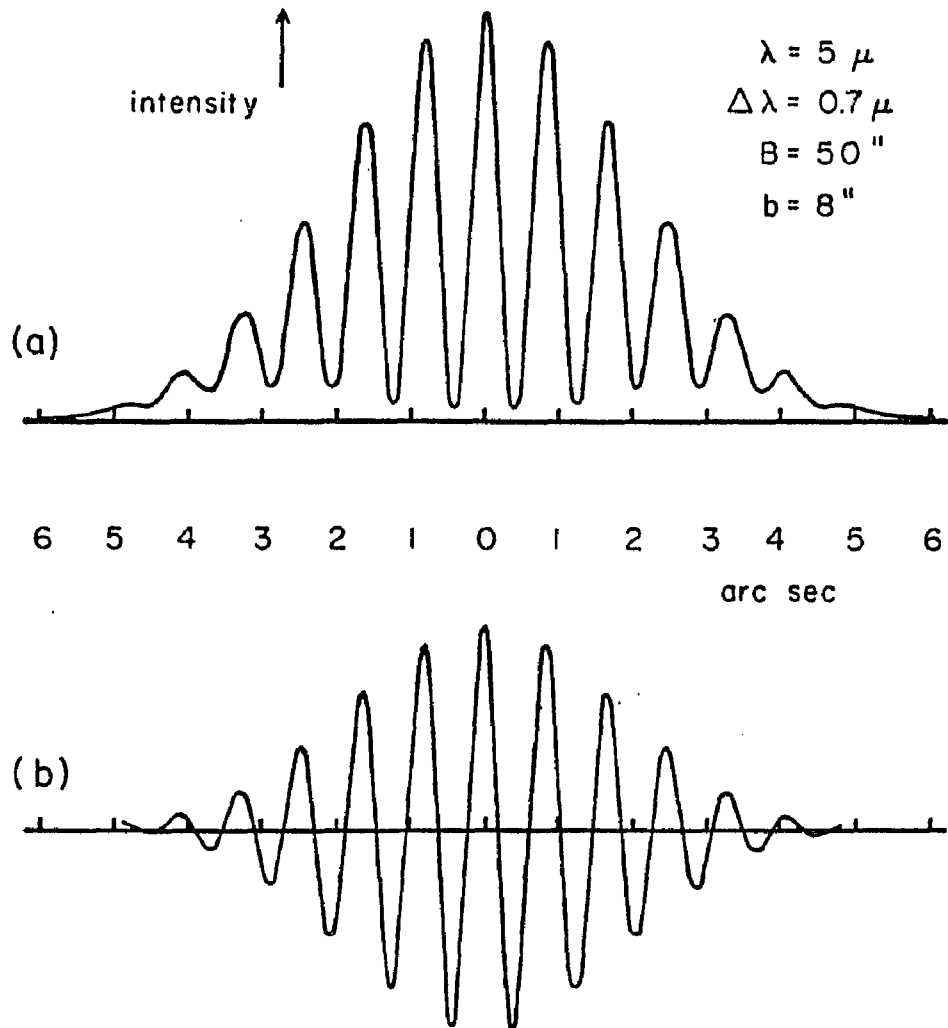


Figure 4.1. Theoretical Beam Patterns

- (a) Photometric mode
- (b) Fringe-chopped mode

At the telescope, this beam pattern (interferogram) can be approximately observed by scanning a point source along the baseline while fringe-chopping. Indeed, this technique has been used successfully both in the lab and at the telescope (c.f., Chapter 6). If an extended source is scanned in this manner, the form of the interferogram remains the same but its amplitude decreases; a large enough object will reduce the amplitude to zero.

Expected Response to a Point Source

As discussed in Chapter 3, all interferometric data for a given source are expressed in terms of a "normalized fringe amplitude" (hereinafter referred to as N.F.A.) which is defined as the ratio between the fringe and total flux signals. Furthermore, the ratio of an unknown object's N.F.A. to that of a point source is its fringe visibility. Clearly, it is desirable to know the theoretical N.F.A. of a point source so that instrumental performance can be measured by comparing this number to that observed at the telescope. This parameter is also beneficial in evaluating the severity of atmospheric disturbances, as discussed in Chapter 5. We shall now calculate the theoretical N.F.A. of a point source.

The plan of attack is to integrate the three-dimensional intensity profiles measured in the fringe and photometric modes along a direction parallel to the fringes. For each mode, the resulting intensity profile will be projected on a slotted mask which simulates the focal plane mask within the instrument. Finally, a planimeter is

used to integrate the intensity transmitted by the mask in each mode so that the ratio of the two results yields the theoretical N.F.A.

The three-dimensional signals in the two modes are expressed by the following:

$$\text{flux distribution:} \quad \int_{\text{image}} 2 \left| \frac{2J_1(\pi d_\lambda \sin\theta)}{\pi d_\lambda \sin\theta} \right|^2 ds, \quad (4.6)$$

$$\text{fringe-chopped} \quad \int_{\text{image}} [\text{equation 4.5}] ds. \quad (4.7)$$

distribution:

These equations were integrated on a Monroe 325 calculator using a 100 step trapezoidal rule. The following definitions and parameters were employed:

1. $B_\lambda \equiv d_\lambda$ --this definition incorporates the touching condition;
2. integration performed only over Airy disk whose radius equals 1.0 by definition;
3. $\lambda = 5 \mu$; $\Delta\lambda = 0.7 \mu$.

Figure 4.2 shows the resulting intensity profiles projected over a slotted mask. Final integration by planimeter yields the result that

$$\text{N.F.A. of a point source} = 1.26. \quad (4.8)$$

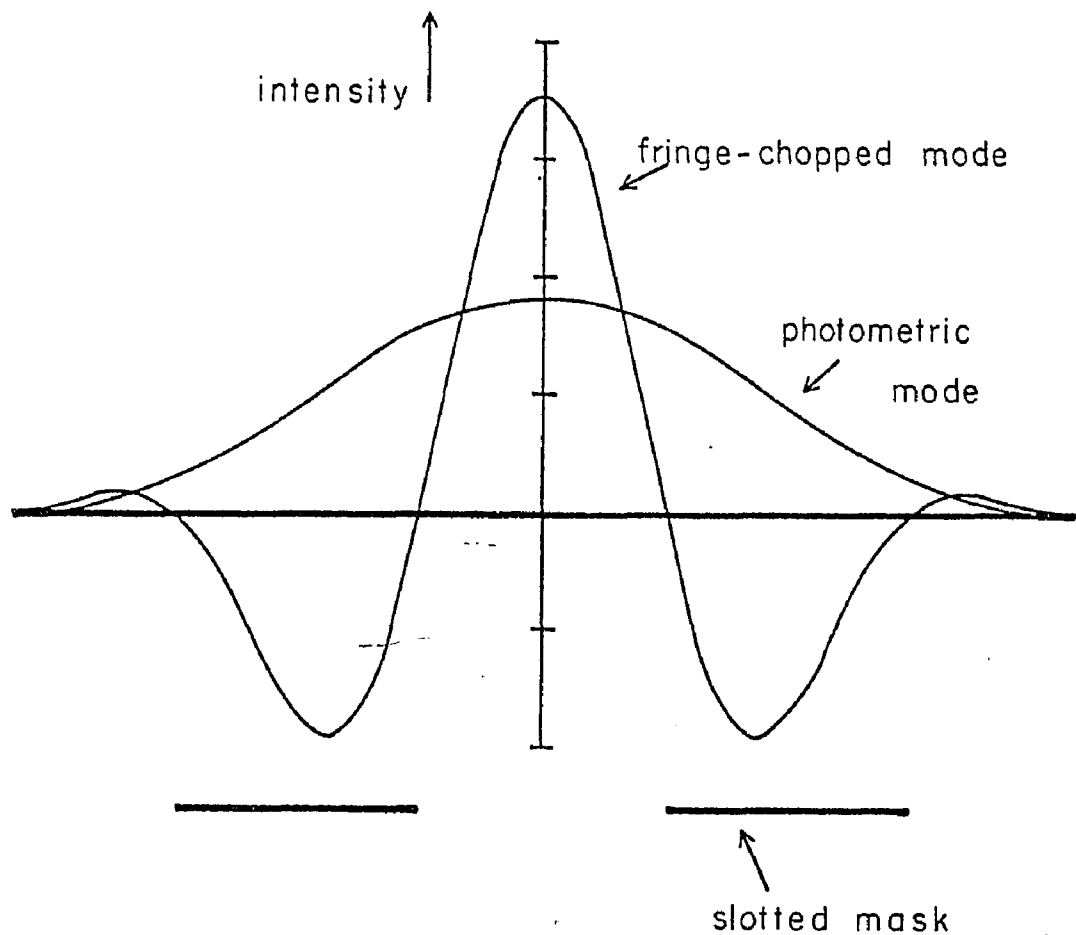


Figure 4.2. Theoretical Normalized Fringe Amplitude of a Point Source

A point source intensity distribution has been integrated perpendicular to the baseline for both photometric and fringe-chopped modes. The area under each curve transmitted by the slotted mask represents a measure of instrumental performance.

Laboratory Tests

Beginning in January 1974, various optical tests were conducted in the laboratory to verify that the instrument design, proposed in Chapter 3, would operate as desired. At $5.0\ \mu$, the first successful lab tests occurred in December 1974; the first telescopic fringes were observed in late January 1975 on the Steward Observatory 90-inch telescope after initial failures at the Steward 21-inch telescope in downtown Tucson. (These failures were caused by very poor atmospheric seeing at this site.) Next, an infrared lab experiment was devised to verify that the interferometer could accurately measure the visibility function and angular diameter of an extended source. The following paragraphs describe that experiment and the results which occurred in February 1975.

The experimental arrangement is shown schematically in Figure 4.3. A thermal source situated behind a small circular aperture of known size provides the artificial infrared star which is imaged by a 12-inch telescope into the interferometer after reflection by a 45° plane mirror. A series of apertures can be interchanged to simulate stars of different angular diameter. The telescope is used here to provide an $f/15$ beam. The 45° mirror is mounted on a translation stage so that the star can be scanned along the baseline to produce an interferogram. Also, the entire interferometer rests on a two axis mount which can execute small translations to simulate the setting motions of a telescope.

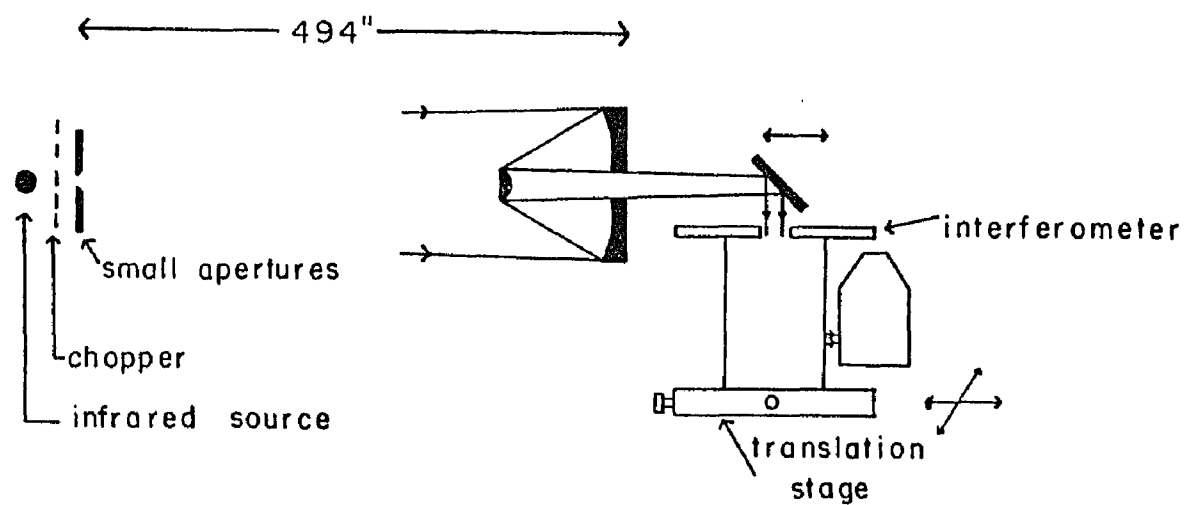


Figure 4.3. Schematic Diagram of Test Equipment

The first goal of this experiment was to demonstrate that the interferometer could measure visibility functions of artificial "stars." Instead of varying the baseline length for each of several "stars," it was easier from a practical standpoint to use four different baselines and to observe a series of star sizes. Consequently, at each baseline measurements of flux and fringe amplitude were obtained for many stars. In each case the N.F.A. was calculated. In order to convert N.F.A. into visibility, simulated point sources were observed using the smallest star for which reasonable signal-to-noise was obtained. The measured point source N.F.A. was 1.0; the difference between experiment and theory is discussed in Chapter 5. In some cases the point source was partially resolved and corrections were applied to the data. The correction technique is to note the star size where fringe amplitude is zero and then to calculate from this number the expected visibility of the point source star. The ratio of expected to measured visibility for the point source can then be used to scale the other measurements. This procedure led to ~ 10 percent corrections.

The visibility results are shown in Figure 4.4 for each baseline. Errors are highest for the smallest stars because of their relatively low signal-to-noise. At the large baselines (Figure 4.4c, -d), errors for small stars are even larger because these were partially resolved and the data were corrected as described in the previous paragraph. Another problem is that the telescope optics were figured for longer wavelengths (25-1000 μ) and at the longest baselines wavefront distortions were probably induced by these optics. This

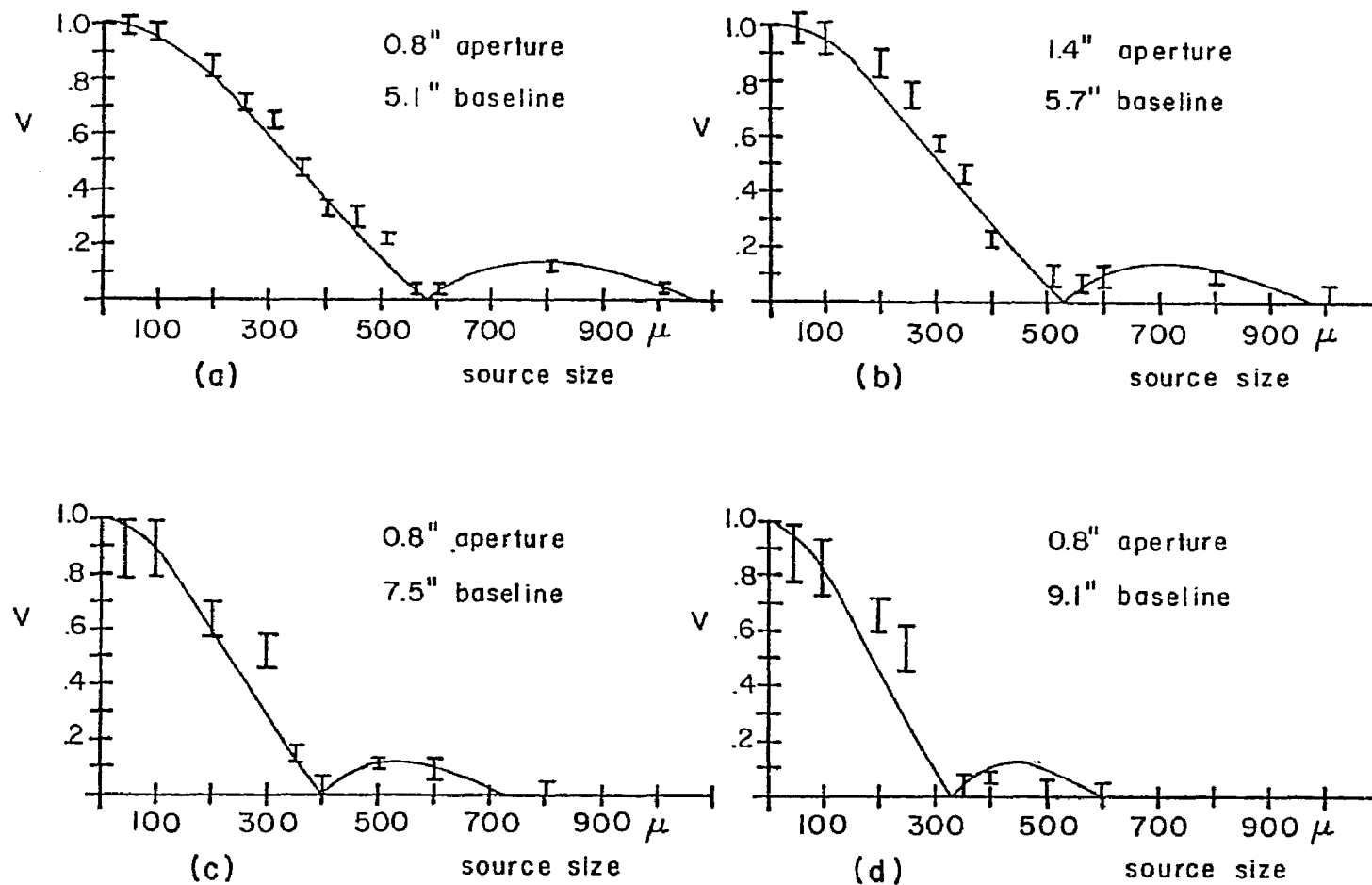


Figure 4.4. Laboratory Measurements of Visibility Functions

Data points are experimental observations. Solid curves are expected theoretical visibility functions.

suspicion is supported by the erratic 2.2μ results (not shown here) at baselines longer than about five inches.

Also shown in Figure 4.4 are the expected visibility functions (solid curves). In view of the experimental problems described above, the overall agreement between theory and experiment seems sufficient to conclude that the interferometer measures visibilities accurate to $\lesssim 10$ percent.

The second goal of this experiment was to measure actual angular diameters. Using the data from Figure 4.4 for a given artificial star, one can pretend that the star's size is unknown and use the data at each baseline to predict this size. The results are shown in Figures 4.5a, -b for two different stars. In the first figure, the known aperture size is 200μ (~ 3.3 arc sec), whereas the solid curve, representing a possible fit to the data, gives a size of $166 \pm 20 \mu$. Here, the long baseline data is relatively inaccurate because of corrections for partial resolution of the point source. This difficulty is alleviated in Figure 4.5b which shows the measured visibilities of a larger source; the data corrections are now much smaller because of the smaller visibility values. Here the known aperture size is 400μ (~ 6.6 arc sec) and the measurements yield $398 \pm 20 \mu$. Therefore, one can conclude that the interferometer performs as expected and that accuracies of $\lesssim 10$ percent can be achieved in measured angular diameters under laboratory conditions. Undoubtedly better accuracy could be obtained by improving the signal-to-noise ratio of the observations as well as the telescope optics.

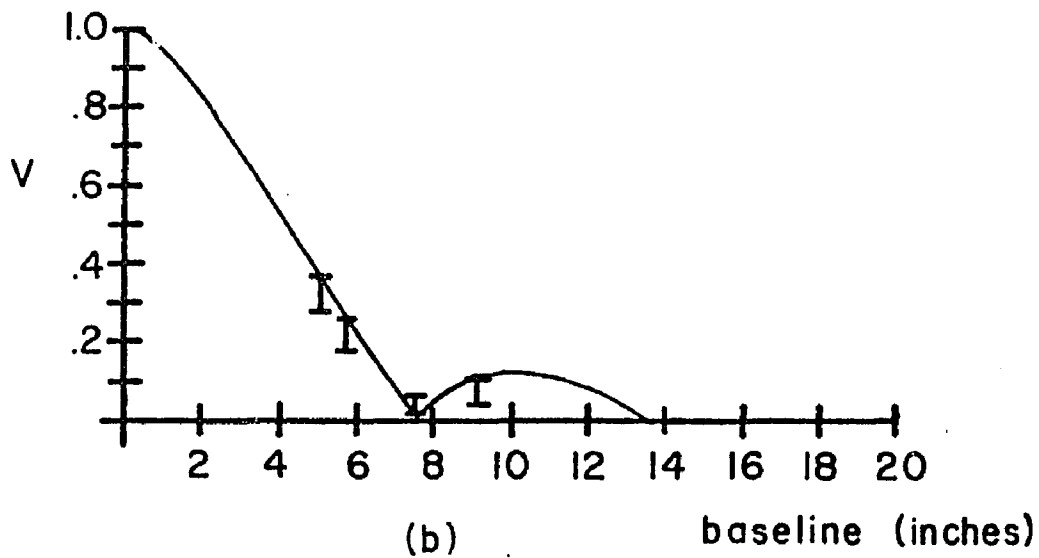
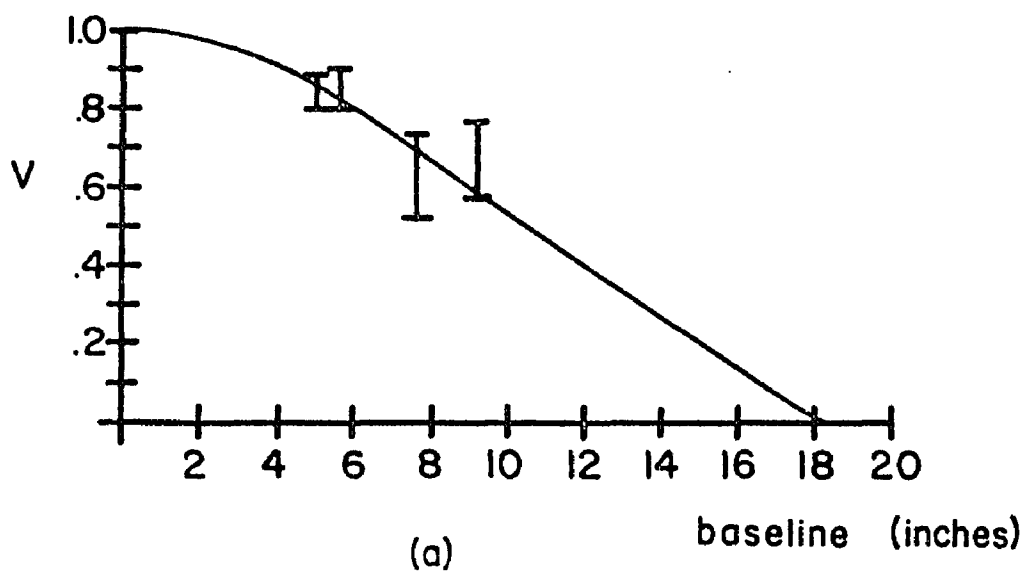


Figure 4.5. Laboratory Measurements of Angular Diameters

- (a) 200 μ source
- (b) 400 μ source. Solid curves are theoretical fits to the data.

In a different test with the same equipment, the secondary supports of the 90-inch telescope were simulated by black wire strung across the telescope's front end. The goal was to measure how such supports would alter the earlier measurements if they intersected the field of view of the two beams. No significant changes were found.

Atmospheric seeing was introduced in these experiments by using a hot air gun to create temperature fluctuations and turbulence within the light path to the telescope. When located close to the telescope, the hot air blast caused fluctuations in the amplitude and phase of the fringe-chopped signal. It was even possible to so distort this signal that only a large amplitude, high frequency noise remained. However, when the blast was located near the source, very little degradation of fringe behavior was apparent. Blasts of cooler, ambient air did not disturb the fringes at any position of the air gun. Similar results have been obtained by Beavers and Swift (1968). No quantitative studies of this induced atmospheric seeing were made in either of these experiments.

Principles of Data Analysis

Previous sections have simply stated that both fringe and flux data are needed from point sources in order to calibrate similar data from extended sources. This section offers a more formal expression of this fact and describes an alternative which does not require point source data.

The intensity distribution in the interference pattern from an extended source with angular diameter, θ , is

$$S_1 = 2I_e [1 + v_e(B_\lambda)], \quad (4.9)$$

where $2I_e$ is the total intensity from both beams including diffraction effects, and $v_e(B_\lambda)$ is the fringe visibility function. The process of fringe-chopping causes a periodic 180° phase shift in the interference pattern so that intensity alternately becomes

$$S_2 = 2I_e [1 - v_e(B_\lambda)] . \quad (4.10)$$

The difference between these two quantities integrated over the slotted mask is the instrumental output given as

$$S_e = S_1 - S_2 \propto 4I_e v_e(B_\lambda) . \quad (4.11)$$

Therefore, the visibility is proportional to the ratio of fringe signal to flux signal and the problem is to determine the proportionality constant, K . If similar data is obtained on a point source of total intensity, $2I_p$, then we can write

$$\text{N.F.A.} = \frac{S_p}{4I_p} = K v_p(B_\lambda) = K \quad (4.12)$$

so that

$$\frac{[\text{N.F.A.}]_{\text{extended}}}{[\text{N.F.A.}]_{\text{point}}} = v_e(B_\lambda). \quad (4.13)$$

Thus, to determine the visibility and hence the angular diameter of the extended source from measurements at one baseline, we must measure the N.F.A. of a point source. This technique will work even during non-ideal atmospheric conditions (cf., Chapter 5) but does assume that these conditions are similar during observations of both sources.

Another technique for measuring angular diameters does not require point source data; however, it does require measurements at two baselines as well as similar atmospheric conditions during the observations. For baselines B_λ^1 and B_λ^2 , we can write

$$M = \frac{S_e^1}{S_e^2} = \frac{I_e^1}{I_e^2} \frac{V_e(B_\lambda^1)}{V_e(B_\lambda^2)} = \frac{V_e(B_\lambda^1)}{V_e(B_\lambda^2)} = \frac{\text{N.F.A.}(B_\lambda^1)}{\text{N.F.A.}(B_\lambda^2)}. \quad (4.14)$$

Because M is a measured quantity, the angular diameter can be derived with an iterative method. For example, if the source is assumed to be uniform and circularly symmetric, then

$$M = \frac{V_e(B_\lambda^1)}{V_e(B_\lambda^2)} = \frac{J_1(\pi B_\lambda^1 \theta)}{J_1(\pi B_\lambda^2 \theta)} \frac{B_\lambda^2}{B_\lambda^1} \quad (4.15)$$

or

$$J_1(\pi B_\lambda^2 \theta) = (\text{constant}) J_1(\pi B_\lambda^1 \theta), \quad (4.16)$$

where

$$\text{constant} = \frac{B_\lambda^2}{B_\lambda^1} \frac{\text{N.F.A.}(B_\lambda^2)}{\text{N.F.A.}(B_\lambda^1)}. \quad (4.17)$$

This method has been applied to the laboratory measurements of the 400 μ source discussed in the previous section. Using data at baselines of 5.14 and 7.48 inches, the best fit diameter is 375 μ .

CHAPTER 5

OPERATION AND PERFORMANCE OF THE INTERFEROMETER AT THE TELESCOPE

Generally speaking, any type of interferometer is difficult to align and operate successfully at the telescope; the infrared spatial interferometer is no exception. Nevertheless, if the observer patiently follows certain procedures, precautions, and performance checks, this instrument will measure visibilities accurate to ≤ 10 percent when the prevailing atmospheric conditions are not too severe. Admittedly, instrumental performance is "seeing sensitive." In fact, atmospheric phenomena are so different from laboratory conditions that special techniques of operation and data analysis have been developed to cope with the signal distortions often induced by the atmosphere.

The first part of this chapter specifies the procedures used to operate the interferometer and to analyze its astronomical data; the final part evaluates system performance and mentions some minor problems which have arisen. Although infrared atmospheric effects are discussed primarily in Chapter 6, the general nature of their influence is presented in the opening section here so that atmospheric distortions, which impose the main limitation on spatial interferometry, may be well understood at the outset.

Atmospheric Perturbations of the
Interference Pattern

Phase and Amplitude Fluctuations
of the Fringe Signal

In laboratory conditions, interference fringes remain stable so that the interferometer's phase-detected fringe signal possesses constant amplitude and phase for a significant period of time. Since neither images nor fringes are moving, it is possible to align the instrument easily and accurately such that the brightest, or zero-order, fringe sits at the peak of the diffraction envelope and is also positioned over the center of the slotted mask. It would be possible to integrate the fringe signal to improve instrumental sensitivity and to display it as a deflection on a strip chart recorder so that data analysis is simply a matter of comparing deflections from various observed objects.

Unfortunately, real astronomical objects are not often observed under such conditions. Instead, atmospheric disturbances cause the images to dance in the focal plane (cf., Chapter 2), so that now both the amplitude and phase of the fringe signal are fluctuating at frequencies which change from night to night between ~ 0 to > 40 Hz. Instead of a constant amplitude deflection, the output now appears as shown in Figure 6.1 (see Chapter 6, p. 108). Clearly, integration of this output is no longer desirable. Nevertheless, it is still possible to extract meaningful, although usually less accurate, results from this new form of data as will now be shown.

Chapter 2 discussed the fact that the atmosphere alters the interference pattern by inducing wavefront tilts and phase delays. Tilts which differ in the two beams cause the images to separate, thereby decreasing the fringe amplitude because fringes form only in the remaining region of overlap. Phase delays cause the zero-order fringe to translate perhaps several fringe widths in either direction away from its ideal position. Therefore, the largest amplitude signals occur when the overlap reaches ~ 100 percent and when the zero-order fringe is either moving across or sitting on top of the central slot in the mask. Because these two conditions are not always satisfied simultaneously, or for a long time, the largest signals appear as intermittent spikes whose duration and separation depend on the frequencies of wavefront tilts and phase delays. The amplitude of a significant number of the largest spikes can be used as the measurement of fringe amplitude.

In practice, the observational goal for each object is to accumulate a sample of these large spikes using a technique which responds rapidly enough to isolate the zero-order fringe so that its measured amplitude is not affected by its motion. The method which has been employed is to operate both choppers at the highest, practicable frequency (20 Hz photometric; 40 Hz fringe) and to FM record the amplified and filtered detector signal onto magnetic tape, thereby preserving its high frequency components in a permanent form. In the laboratory, this tape is replayed through a phase-detector so as to display the amplitude and phase of each chopper cycle on chart paper.

At the present time, observations are usually restricted to nights when the diameter of the full-aperture seeing disk from the telescope is $\lesssim 3$ arc sec. When atmospheric conditions are worse than this limit, the choppers cannot adequately follow the fringe motion and the normalized fringe amplitude of a point source decreases from its nominal value of 1.0 to 0.6 or less. In very poor conditions (seeing disk ≥ 6 arc sec) it is sometimes impossible to detect any fringes.

Redisussion of Instrumental Tolerances

Table 3.1 has presented some mechanical and operational tolerances which the various instrumental components must achieve for the interferometer to operate properly. However, these tolerances were based on the assumption of perfect fringe stability. Since this ideal condition occurs only very rarely (cf., Chapter 6), many of these tolerances can be relaxed to a degree which is dependent on atmospheric conditions. For example, let us assume that the visual seeing is 2 arc sec; i.e., that image dancing is occurring between the two interferometric images and that the amplitude of their separation is 2 arc sec. Now, if observations are being made at a baseline of 50 inches, then the induced path difference between the two beams is at least

$$\Delta l = \pm (50 \text{ inches})(2 \text{ arc sec}) \approx \pm 12 \mu. \quad (5.1)$$

At a wavelength of 5μ , this distance corresponds to ± 2.5 fringe widths so the zero-order fringe is vibrating in the focal plane with an extent of 2.5 fringes in either direction about its nominal position. Therefore, the observer must align the instrument as best he can under the

given conditions and then rely on the atmosphere to center this fringe frequently during the measurement. Thus, it is no longer necessary to require roof mirror positioning to within $\frac{\lambda}{4}$ and stability of the optical components to within $\frac{\lambda}{2}$. Also, the restriction on telescope tracking can be relaxed since now only the centroid of the two images needs to be tracked accurately. Table 5.1 gives an idea of some new tolerance values which are more realistic than Table 3.1. However, these are only ballpark numbers because atmospheric conditions do change; indeed, the tolerances of Table 3.1 should still be within the capabilities of instrumental design because occasionally the atmosphere does become quite well behaved at infrared wavelengths.

Operating Procedures

Alignment

Once the interferometer has been mounted on the telescope, the initial goal is to visually align the instrument relative to the telescope (Figure 5.1a, -b). First, with the stage out of the viewing field the telescope is visually focused on a star which is bright at both optical and infrared wavelengths. Second, with the stage in place, the visual image is used to locate the position of the InSb detector on the reticle; all future observations must be made with the visual image centered on this spot. To find this spot, the telescope's slow motions are used to maximize the infrared photometric signal. Third, the observer must center the two beams on the telescope's primary mirror. To date, this alignment has been accomplished in three steps:

Table 5.1. Instrumental Tolerances Required for Operation During Typical Seeing Conditions

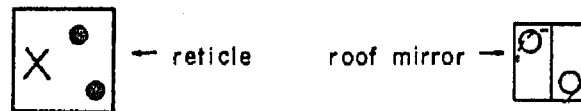
$\lambda = 5 \mu$, $B = 50$ inches, $f = 20.8$ inches, $d = 0.25$ inch, visual seeing disk = 2 arc sec

	<u>Expression</u>	<u>Result</u>
<u>Requirement:</u> achieve and retain intermittent alignment of zero-order fringe on slotted mask during ~ 100 percent image overlap		
<u>Mechanical Tolerances</u>		
1. displacement of stage components along baseline		
a. relative shift between adjusting mirrors	2.5λ	12μ
b. shift of roof mirror	1.3λ	6μ
2. resolution in roof mirror translation	1.3λ	6μ
3. angular stability of telescope optics	$2.5 \lambda/B$	2 arc sec
<u>Operational Tolerances</u>		
1. telescope pointing resolution	$2.5 \lambda/B$	2 arc sec
2. telescope tracking error	$2.5 \lambda/B \div 15 \text{ min}$	$2 \times 10^{-3} \frac{\text{arc sec}}{\text{sec}}$

<u>Requirement:</u> achieve a maximum reduction of ~ 10 percent in normalized fringe amplitude; efficient use of instrument		
<u>Mechanical Tolerances</u>		
1. dimensional error in slotted mask	$0.1 \lambda f/2d$	0.02 mm
<u>Operational Tolerances</u>		
1. image overlap error when images at centroid	$\sim 10 \%$	---
2. touching condition error at roof mirror	---	1 mm
3. fringe chopper throw error	$\sim \lambda/15$	0.3μ
4. telescope setting requirement	---	$\lesssim 10$ arc sec

symbols :

- X - detector position
- - image of one interferometer beam
- - image of one beam out-of-focus
- ⊙ - interferometer images with fringes
- ⊖ - image of primary mirror

images in reticleout-of-focus images at roof mirror

(a) interferometer out of alignment



(b) align relative to telescope



(c) align interferometer



(d) path equalization

Figure 5.1. Alignment of the Interferometer

This figure illustrates what an observer sees at the visual focus during the different stages of alignment.

1. with stage lowered, center the stellar image on the detector's reticle position;
2. with stage in place, recenter the stellar image from the right-hand, adjusting mirror so that it is aligned with the detector along the baseline direction; this adjustment has been made by tilting the roof mirror;
3. rotate the right-hand adjusting mirror so its image lies on the detector position; then use both motions of the left mirror to overlap the two visual images.

It should now be possible to remove the eyepiece and observe that the out-of-focus aperture images are unvignetted circles of starlight bisected by the spider arms of the telescope's secondary mirror, assuming that the baseline is oriented along the spider arms (Figure 5.1b). If the alignment is not satisfactory the aperture mask can be shifted and the above procedure repeated until the desired result is achieved. The instrument has now been visually aligned relative to the telescope. In the remaining alignment the positions of beamsplitter, apertures, and telescope should be considered as fixed.

The next goal is to visually align the interferometer itself (Figure 5.1c). First, the touching condition is established by translating the adjusting mirrors horizontally until the out-of-focus aperture images are nearly touching as they leave the roof mirror. Second, with the eyepiece in place, the individual stellar images are recentered on the detector position using the adjusting mirrors.

Next, the interferometer is aligned in the infrared. First, the $2.2\ \mu$ photometric signal from each beam is examined to see if both are equal. If not, then image overlap must be adjusted by maximizing the signal from one beam (usually the right beam) with the telescope's slow motions and then by moving the other adjusting mirror to maximize its signal. In this case, the telescope had to be moved to be certain that the first beam was centered on the slotted mask. Second, the dewar should be oriented to maximize the signal from each beam. Third, photometric signals are examined at $5\ \mu$; the goal is to equalize signals and to eliminate "sky offsets" when the star is moved away. At this point, the dewar orientation may require slight changes to eliminate offsets and the image overlap may require readjustment to equalize signals because the change of infrared filter can alter image location. Once all these requirements are met, the interferometer is ready for the final adjustment: path equalization and fringe detection.

The goal of path equalization (Figure 5.1d) is to center the interference pattern on the slotted mask. Undoubtedly, fringes will not be present if the fringe chopper is simply turned on at this time, so it is necessary to find them first and to do the centering second. The idea is to operate the fringe chopper while translating the roof mirror in small increments until evidence of interference fringes is seen in the infrared phase-detected output. It is most convenient to work at the longest possible wavelengths ($5\ \mu$ here) because here the coherence length is largest (depending on bandwidth, of course) and the roof mirror can be translated in large ($\geq 10\ \mu$) steps. Also, fringes will probably be more stable at the long wavelengths and hence

easier to find, especially if the seeing conditions are marginal. Once fringes are found, the roof mirror is moved in very small increments to maximize the signal. During good seeing conditions a finer alignment or check is available using the position of the white-light fringes in the eyepiece; the roof mirror is translated until these fringes are located on top of the detector position. Now the interferometer has been aligned and tested; it is ready to perform actual observations.

Measurement

As mentioned in previous chapters, the general scheme of observing is to record photometric and fringe data for both extended and point sources. The point source data is needed to convert the normalized fringe amplitude of an extended source into fringe visibility. For this conversion to be accurate, both sets of measurements must be obtained under similar atmospheric conditions; therefore, it is most desirable to have these sources close together on the sky. In addition, because atmospheric conditions can change unexpectedly during a night, it is necessary to obtain frequent measurements of point sources and to sandwich each set of extended source data between observations of nearby point sources. Several repetitions of this procedure may be required to produce an accurate result unless atmospheric conditions are well behaved.

The specific measurement process consists of the following steps:

1. Location of the object. This can be accomplished either visually or by scanning the telescope in a raster pattern

and watching for an increase in the infrared photometric signal from an invisible source.

2. Center the infrared image on the slotted mask. As before, this can be done either visually using the detector's known reticle position or by maximizing the infrared photometric signal with the telescope's motion. On an ideal night, the DC piezoelectric stack can be used to help maximize the fringe signal by centering the zero-order fringe on the central slot. On a nonideal night, one relies on the atmosphere to provide this fine alignment.
3. Photometric measurement. The flux from each beam is measured separately; the combination requires ~ 1 -2 minutes of time.
4. Fringe measurement. Fringe data is accumulated until the observer believes that an adequate sample of the largest signals has been collected. During this time the observer can perform "active guiding" using the visual image, and he can also estimate the object's normalized fringe amplitude to interpret the significance of his results. The duration of this measurement is approximately 5-10 minutes, depending on atmospheric conditions.
5. Photometric measurements. Now, the flux from each beam is remeasured and compared to earlier results to determine if the source image has drifted out of alignment. Such drifts can be caused by telescope tracking errors, shifts between optical elements, or displacements of the detector system.

Atmospheric transparency may also have varied during this time. If changes have occurred, then the preceding steps should be repeated.

6. Sky offset measurement. Finally, the source is moved out of the field of view and photometric measurements are made of the sky-plus-instrument background radiation. If offsets do occur, their amplitude and phase in each beam must be noted because their influence on the photometric signal from the real source must be corrected for later.

Once this sequence of measurements has been applied to both an unknown source and one or more nearby point sources, several choices are available. First, if atmospheric conditions are poor or have changed, then the observer may wish to repeat previous measurements. Second, a new set of objects may be observed. Third, the original objects can be observed with different wavelengths, position angles, or baseline lengths; however, the latter two items will necessitate some realignment.

Two additional items should be noted in connection with observing procedures. First, when visually setting an image on the detector's reticle position, one must be careful to account for atmospheric dispersion effects. For example, with stars at zenith distances of 30° , 45° , and 60° , the visual and $5\ \mu$ stellar images are separated by 2, 3.6, and 6 arc sec, respectively. Second, during the night attempts should be made to control "dome seeing." It is

often advantageous to adjust wind screens and to turn on inside ventilation fans in order to suppress turbulence within the dome or at the slit.

Data Analysis

Electronic Processing

Figure 5.2 is a schematic diagram of the electronic processes involved in laboratory data reduction. The general idea is to replay the FM tape so that the detector signal is phase-detected and the envelope of the resulting AC signal is plotted on chart paper. This AC signal contains the amplitude and phase of the signal obtained during each measurement by the two choppers; i.e., 40 fringe measurements per second and 20 flux measurements per second. Its envelope is obtained by plotting the signal on slowly moving chart paper, thereby blending together all the separate chopper measurements. This format provides a concise record from which the maximum amplitudes of the fringe and flux signals are conveniently determined.

Because the frequency response of the chart recorder decreases sharply beyond 15-20 Hz, additional electronics are used to change the 20 and 40 Hz chopper frequencies into ones which can be handled efficiently by the recorder. First, the normal playback speed of the FM tape is reduced a factor of four by substituting a 400 Hz, 10 volt sine wave for the tape recorder's own oscillator which cannot be easily adjusted. Second, since the frequency-to-voltage converters within the recorder are not optimized for the new speed, the tape must be replayed in the "direct mode" and the demodulation is now performed by separate, adjustable frequency-to-voltage converters (VIDAR 326). As a result,

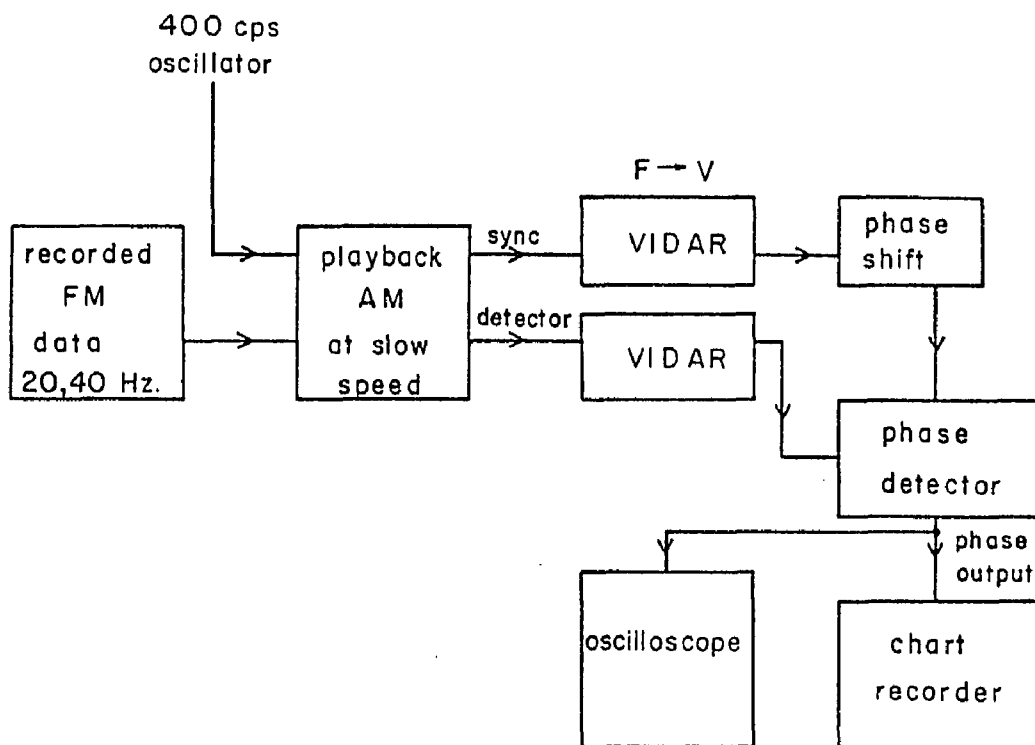


Figure 5.2. Schematic Diagram of Data Analysis Electronics

the new AC signals are replicas of the originals except slowed down by a factor of four in frequency.

Now the new signals are phase-detected using the chopper reference signals which were tape recorded simultaneously at the telescope and were frequency-reduced in the lab. The final product is another AC signal which contains both phase and amplitude information and appears identical to that seen in real time on the oscilloscope at the telescope. This is now recorded on slow moving chart paper where the phase information is revealed by the direction of pen motion. Figure 6.1 (see Chapter 6, p. 108) shows examples of data displayed in this fashion.

The operation of this electronic system must be supervised constantly in order to label properly the data being analyzed, to adjust system gains for different objects, to keep phase-detected signals in phase, and to detect various irregularities and distortions which can sometimes appear. On a night of good observing, nearly one mile of magnetic tape can be utilized to record data. Therefore, laboratory analysis may consume a substantial amount of time, especially since the effective length of time is increased by the factor of four decrease in playback speed. To lessen this effort, it is necessary to edit the recorded tape in the sense of ignoring poor observations as determined by real time inspection at the telescope. Thus, it is important for the observer to provide notes on the quality and tape location of such data.

Before beginning reduction of a data set, the entire electronic system should be tuned to provide optimum performance. For example,

various electronic filters can be selected on the recorder during playback to provide the best waveform and signal-to-noise ratio. The frequency range of the VIDAR is also adjustable so that the slowed-down carrier frequency from the recorder lies near the center of the VIDAR's linear range. In addition, the Sanborn chart recorder is set up to provide the proper degree of damping on the pen motion. Tests of this system have shown that noise levels of ~ 20 mv are maintained in the final output. Because the original signals contain similar noise levels, the data reduction system does not significantly alter the quality of the recorded data.

Conversion to Fringe Visibilities

At this point the observer performs the final steps of data analysis by inspecting the chart record which now contains the envelopes of phase-detected signals for all observations during the night. The initial step is to deduce the maximum amplitude of the envelope for each observation. To date, no rigorous procedure has been followed to determine this quantity; rather a person merely insures in his own judgment that a significant number of the largest signals are present and that these are not spurious. The next step is to calculate the N.F.A. of each object by forming the ratio of fringe to flux amplitude. In the third step, these values are used in equation 4.13 to deduce fringe visibilities of extended sources.

System Performance

Sensitivity

Presently, using 14-inch apertures, the spatial interferometer can obtain meaningful data on objects whose 5 μ apparent magnitude is brighter than + 1.0. This limiting magnitude is the result of three main causes: small apertures, excessive instrumental background radiation, and no integration capability. As mentioned below instrumental improvements can be made in each of these areas so that the interferometer's sensitivity can be extended considerably.

Because the interferometer now operates with the largest beams acceptable by its mirror geometry, the telescopic apertures can only be increased by using larger diameter telescopes where the two interferometer beams will have larger projections on the primary mirror. Note, however, that doubling the aperture sizes does not lead to a four-fold improvement of signal-to-noise because the detected photon noise doubles in a detector system which is limited by sky background. Therefore, signal-to-noise increases only a factor of two.

Excessive infrared background within the instrument is produced by the "hot stop" which selects the two apertures from the main telescope beam. As mentioned in Chapter 3, this stop contributes unwanted photon noise because the detector sees a small area surrounding each hole in the aperture mask. Excess noise can be reduced by replacing the stop with a mirror system designed to select the two apertures and to image the detector's remaining field of view back into the dewar. Chapter 7 describes such a system.

In the existing interferometer, integration techniques can be employed only during ideal atmospheric conditions when the fringe-chopped signal remains nearly stable in amplitude and phase. Existing observations (Chapter 6) suggest that this phenomenon can occur at the telescope but only very rarely. An alternative to waiting for these precious moments is to build a servo system which "corrects" the final image for atmospheric distortions; such a technique is presented in Chapter 7.

Measurement Accuracy and Sources of Error

Resolving power of the interferometer is governed primarily by two factors: baseline length and measurement accuracy. The former regulates angular fringe width so, with larger baselines, higher spatial frequencies are sampled. Measurement accuracy sets an upper limit on attainable resolution at a given baseline. Telescopic observations show that the interferometer measures fringe visibilities to accuracies of 5-20 percent. Let us see what the corresponding range is in terms of resolving power.

Consider a source with an observed 5 μ visibility of 0.95 ± 0.05 at a baseline of 50 inches. We can place an upper limit on the source's angular size by fitting an assumed visibility function through the lower visibility limit. For a uniform, circular object, this limit is 0.20 arc sec. Therefore, the interferometer's limiting angular resolution is 0.20 arc sec for data with 5 percent accuracy. All objects larger than this limit will be resolved because their visibility bounds are

< 1.0 On the other hand, if measurement accuracy is ~ 20 percent and the measured visibility is 0.8 ± 0.2 , then the limiting angular resolution is 0.37 arc sec--much poorer.

Improvements in accuracy will be hard to achieve with present instrumentation because of detrimental effects induced by atmospheric seeing. These effects tend to weaken an observer's control of the measurement process by rendering him dependent on the atmosphere to provide fine alignments of the interference fringes. For example, in order to properly calibrate the N.F.A. of an extended source, it is important that fringe data for both extended and comparison sources be measurements of the same observational parameter such as the fringe amplitude of the zero-order fringe during ~ 100 percent image overlap. In practice, an observer cannot be sure this condition is satisfied because he is dependent on atmospheric fluctuations to provide it. Therefore, in order to regain some influence in the measurement process, he must make several sets of observations on the same objects to check repeatability and consistency of the results. If data are consistent, then he can probably be confident the atmosphere is performing as desired. If not, then the data are of questionable value.

Although atmospheric seeing enables us to relax some of the operational tolerances in Chapter 3, it also makes operation of the interferometer more difficult by increasing its susceptibility to two sources of error. The first concerns instrumental alignment. Since the atmosphere causes image dancing and fringe motion, it is difficult to adjust path equalization well enough so that during ~ 100 percent

overlap the zero-order fringe has a good chance of being centered. If a systematic path error is present, then fringes will be shifted away from the image center and the measured N.F.A. of a point source will become < 1.0 . The second error concerns pointing of the telescope. As an example, assume the telescope is pointed at the centroid of the two moving images. In this position, the interferometer is likely to measure some occasional signals from the zero-order fringe during ~ 100 percent overlap. However, if a positional error occurs along the baseline, then fringes will be displaced away from the centroid, thereby decreasing the fringe-chopped signal; the photometric signal will not decrease as rapidly so the result is a reduction of N.F.A. Therefore, if the image centroids of an unknown and a known source are not positioned identically in successive observations, a serious error could occur in the visibility determination. This effect has already presented problems during observations and is another reason for repeating sets of observations.

Unfortunately, these pointing errors become more significant at longer baselines as the fringes shrink in angular size. For a 50-inch baseline (fringe width = 0.8 arc sec), a positional error of ± 1.2 arc sec will decrease the fringe-chopped signal ~ 20 percent. At a 100-inch baseline, the telescope must point to within ± 0.6 arc sec to achieve the same result. Admittedly, the image centroid is also moving around so that the effects of these errors are somewhat alleviated. Nevertheless, pointing errors are significant, especially when using the peak infrared photometric signal from an invisible

star as an indication of alignment. If the object is visible, then its image can be centered on the reticle in an easily repeatable manner so that positional errors are not as large.

Finally, it should be noted here that absolute accuracy of the derived visibilities is very dependent on the assumption that the comparison object is a point source ($V = 1.0$). If this is not true, then the unknown object will appear too large as occurred in some of the laboratory experiments discussed in Chapter 4. The true nature of the comparison source can be inferred from other observations such as optical interferometry or infrared spectrophotometry. When spatial interferometry is extended to longer wavelengths ($\geq 10 \mu$), the problem of finding point sources will become very real.

Observed Response to a Point Source

An excellent indication of instrumental performance is to compare the theoretical and observed responses to a point source. Chapter 4 has shown that the theoretical normalized fringe amplitude should be 1.26. However, both laboratory (Chapter 4) and telescopic observations give a value of 1.0. Consequently, fringe detection within the interferometer appears to be 80 percent efficient. What causes the 20 percent loss? Unfortunately, the exact cause is unknown but two possible explanations exist. The first involves the frequency characteristics of the electronic equipment used to record and analyze the data. Since the flux and fringe measurements are taken at two different frequencies (20, 40 Hz, respectively), it is possible that the electronic gains are also different. Thus the interferometer might actually

perform properly but the processes of recording and analysis may alter the relative magnitude of these two signals. More tests of the electronics must be done to determine the significance of this effect. The second explanation is that the $5\ \mu$ radiation loses some of its coherence before reaching the focus. If about 14 percent of the available energy were rendered incoherent, then the fringe signal would decrease whereas the flux signal would remain constant. The cause of this coherence loss is not likely to be atmospheric in origin because it is not wavelength dependent from $2.2\text{--}5\ \mu$ and because laboratory and telescopic tests give the same result. The fault could lie within the dewar, perhaps in the window and filter materials, in which case better optical surfaces and coatings for these components might shed some light on this problem.

Minor Problems

Several small problems have arisen occasionally during observations and have proven to be nuisances because they necessitate realignments of the interferometric system. First, when rotating the instrument in position angle about the telescope's optical axis, the images do not remain fixed in the visual reticle. This behavior is expected if the detector is not centered on the axis of rotation. Unfortunately, it means that the entire alignment procedure may need to be repeated depending on the amplitude of image shift. At the least, path equalization must be repeated. The second problem has involved sudden or gradual shifts in the positions of telescope optics. Actually, one should expect such shifts and also changes of focus because of temperature drops during the night as well as flexures in structural elements.

Nevertheless, these effects do shift the zero-order location in the focal plane and cause annoying decreases in N.F.A. which are not predictable.

Another problem concerns the presence of "offsets" in the infrared photometric signals. Such offsets are caused when the detector sees different background intensities in the two photometric chopper positions. These signals simulate real sources but are actually caused by the detector's seeing some warm surface within the interferometer or telescope. For instance, if one or both beams are projected off the edges of the primary or secondary mirrors, then offsets develop. The effect is to increase or decrease the photometric signal depending on the relative phase between the two. Once the amplitude and phase of each beam's offset are measured by photometric chopping on the sky, the effects of offsets can be eliminated.

CHAPTER 6

ATMOSPHERIC AND ASTROPHYSICAL RESULTS

In March 1975, the spatial interferometer became the first instrument of its kind to measure stellar angular diameters at infrared wavelengths. Initial observations with this new system were performed on 61-inch and 90-inch telescopes during a wide variety of atmospheric seeing conditions. They showed that the technique extends infrared spatial resolution down to about 0.1 arc sec and that baselines longer than two meters can probably be used to achieve even higher resolution.

The original measurements were intended to accomplish two goals which would help define the capabilities and limitations of the existing technique. The first goal was to measure angular diameters for IRC +10216 and VY CMa. The former, besides being an interesting object, would serve as a test source, having already been resolved by lunar occultations. VY CMa was a well-known infrared star unresolved by other techniques. The second goal was to study infrared atmospheric seeing--both the phenomenon itself and its limitations on performance of the interferometer. By May 1975 both goals had been achieved (McCarthy and Low 1975). The results are discussed more fully in the remainder of this chapter.

Atmospheric Results

It is well known that atmospheric seeing imposes the main limitations to visual spatial interferometry but its infrared properties were unknown at the beginning of this investigation. Perhaps it was fear of what infrared seeing would be like that postponed the development of infrared spatial interferometry. Now, observations have shown that, although the atmosphere can drastically inhibit $5\ \mu$ spatial interferometry, the amplitude and phase fluctuations of the fringes are more well-behaved in the infrared than in the visual. The purpose of this section is to discuss the nature of these observations and their physical implications.

Correlation Between Visual and Infrared Seeing

An approximate correlation exists between the severity of visual seeing as indicated by the character and motions of the visual images, and the severity of infrared seeing as determined by amplitude and phase fluctuations in the $5\ \mu$ fringe signal. The qualitative nature of this relation is discussed below and illustrated in Figure 6.1.

In conditions of good visual seeing, a stellar image from the full telescope aperture has an angular diameter of ≤ 1.0 arc sec and the two interferometric images resemble textbook diffraction patterns which remain in nearly constant overlap, showing ~ 2.44 white-light fringes. In the infrared, the fringe signal is very stable, showing occasional small changes of amplitude and/or phase at low frequencies as shown in Figure 6.1a. In this figure time runs horizontally across the page.

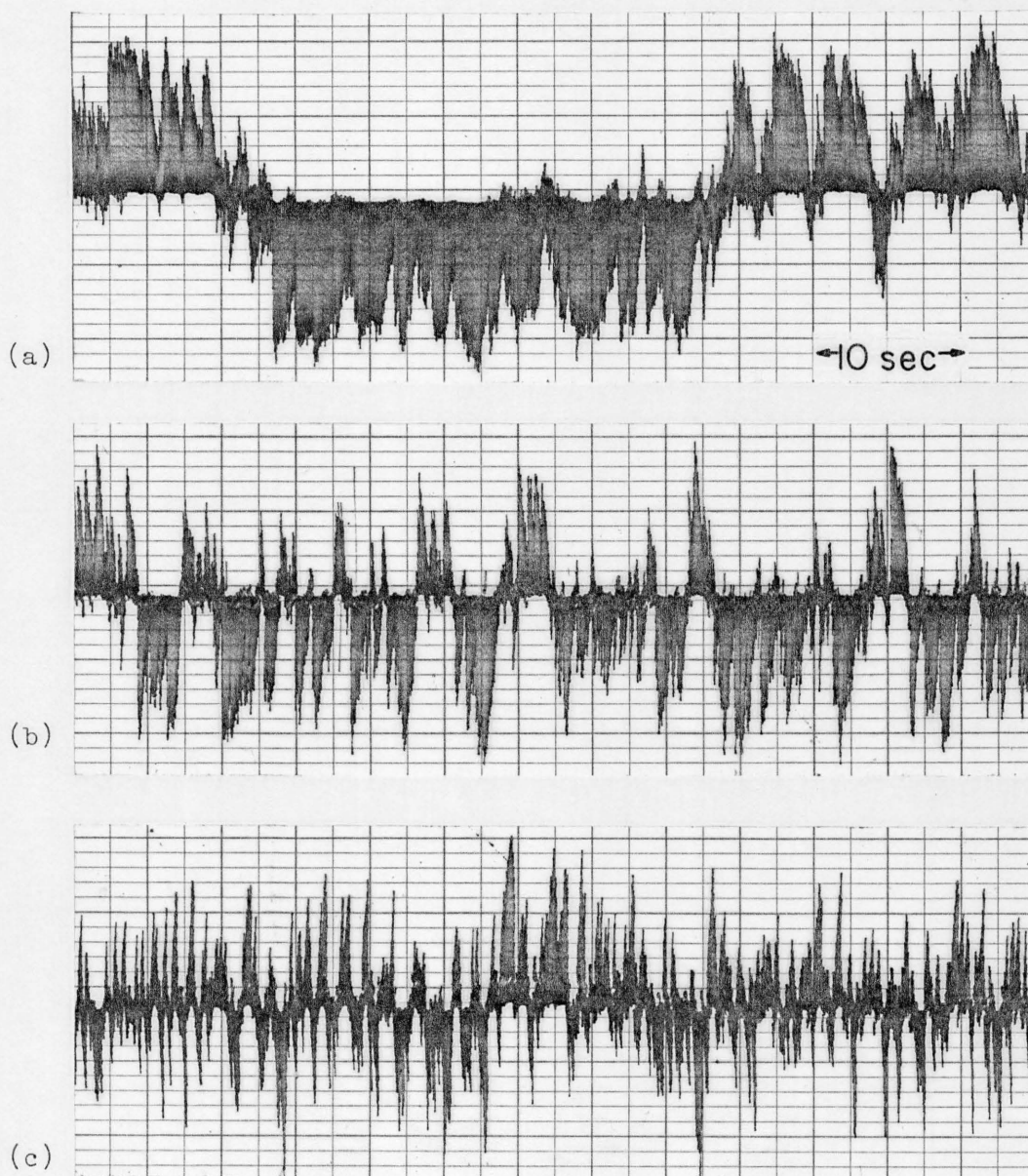


Figure 6.1. Extremes of Infrared Seeing

- a. 1 arc sec visual seeing. α Boo B = 40", d = 8"
- b. 2-3 arc sec visual seeing. VX Sgr B = 74", d = 14"
- c. 3 arc sec visual seeing. VY CMa B = 48", d = 5"

The 5 μ phase-detected fringe signal is shown during different conditions of visual seeing. Separate chopper measurements are blended together to produce an envelope of the signal. At any time, signal amplitude and relative phase are measured by the envelope height and by its location above or below the zero level.

Amplitude and phase of the fringe signal are displayed vertically, where phase changes 180° about the zero-line of the signal.

As visual seeing worsens, the telescopic image expands to ~ 2 arc sec and the rate and amplitude of image dancing increase. At the same time infrared fringe stability deteriorates (Figure 6.1b). When the telescopic image reaches ~ 3 arc sec, individual images have enlarged above their diffraction limit indicating that visual coherence is being lost across each aperture. Also, the amplitude and frequency of image dancing continue to increase. Now, numerous white-light fringes appear throughout an area whose width exceeds that of the theoretical coherence region. Apparently, the zero-order fringe is translating through large distances in the focal plane at frequencies much greater than 10 Hz so that the human eye sees many fringes throughout an enlarged area. In the infrared, the fringe signal becomes more unstable (Figure 6.1c) and the measured N.F.A. of a point source declines to 0.7-0.8. This reduction might be caused by the combination of poor 5μ coherence across the apertures and fringe motions with frequencies approaching the chopping rate of 40 Hz. Conditions are now marginal for visibility measurements. Another serious problem is that telescope pointing can no longer be performed in a reliable, repeatable manner for each astronomical object.

If the visual seeing exceeds 3 arc sec, the 5μ fringes fluctuate at frequencies > 40 Hz. Now the N.F.A. of a point source decreases to ~ 0.6 and infrared visibility measurements are meaningless. At this point, atmospheric disturbances are so severe that they cause

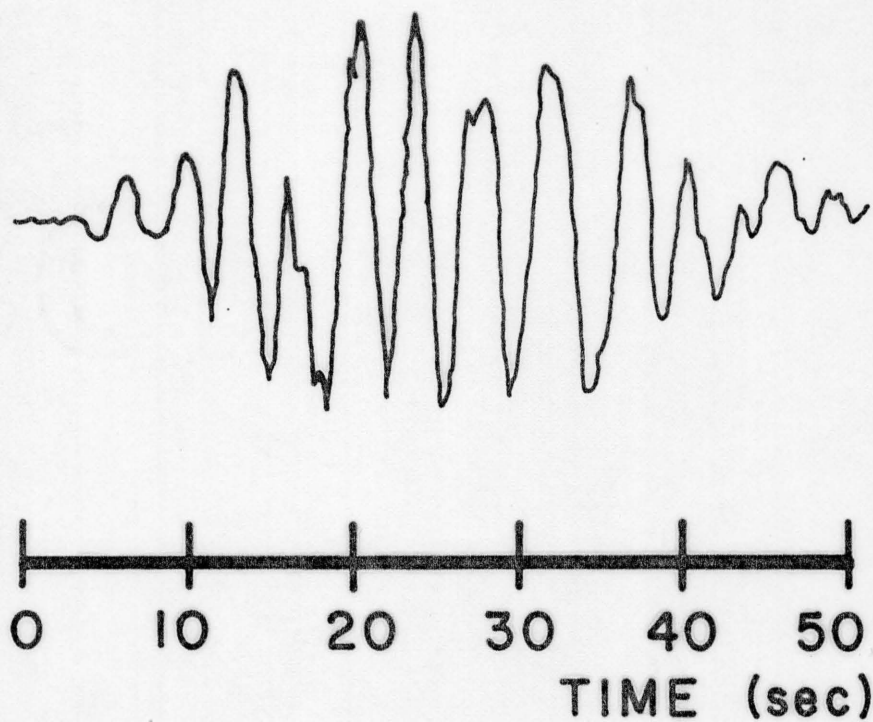
a fringe signal to be observed even when the fringe chopper is not operating. On nights like this, the interferometer should not be used.

Fringe Stability in Excellent Seeing

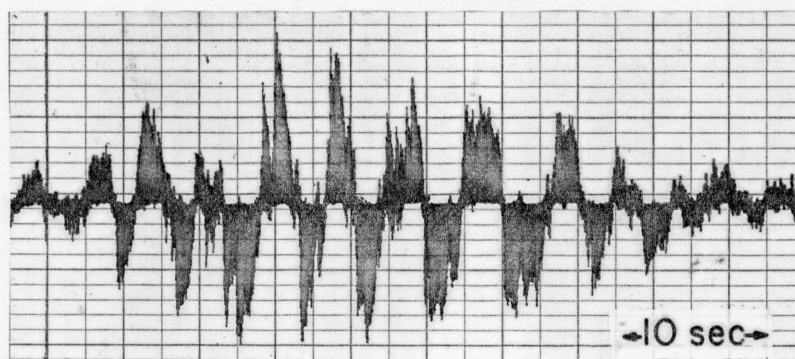
During conditions of excellent seeing, the infrared interference pattern can become stable for periods up to at least 40 seconds. On these rare occasions the visible fringes are exciting to watch as they slowly vibrate within a beautiful diffraction envelope. One such night was 19 April 1975 when the telescopic seeing was 1 arc sec at the 61-inch telescope. Figure 6.2a shows a $5\ \mu$ interferogram of α Boo, obtained during a 40 second scan in right ascension with the fringe chopper operating and with a 40-inch baseline oriented in the east-west direction. The displayed signal is the amplified output from the phase detector and has been integrated with a time constant of ~ 1.0 sec. Figure 6.2b shows the amplitude and phase characteristics of each chopper measurement during this scan. This figure is similar to Figure 6.1.

Excellent atmospheric stability is indicated both by the regular fringe spacing and by the relative amplitudes of successive fringes. Clearly, during the 40 second time period only minor distortions have occurred with amplitudes $\lesssim \frac{\lambda}{4}$.

Figure 6.1a illustrates the fringe signals which were measured before the interferogram was attempted. Although one does not know exactly how far the zero-order fringe moves in causing a given distortion, on the basis of the atmospheric conditions evidenced in the interferogram it seems reasonable that fringe motion is confined to $\pm \frac{\lambda}{2}$.



(a) DC integrated output



(b) AC phase detected output

Figure 6.2. Interferogram of α Boo

As described in the text, this interferogram illustrates a rare occurrence of excellent infrared atmospheric seeing.

Wavelength Dependence of Seeing

Telescopic measurements appear to show that the amplitude of fringe vibration is roughly proportional to inverse wavelength over the range 0.5-10 μ . During excellent seeing conditions (~ 1 arc sec) infrared amplitudes are $\sim \frac{\lambda}{2}$ at 5.0 μ and visual amplitudes are 2-4 λ at 0.5 μ (Knapp 1974). Although not yet fully reduced, data at 2.2 and 3.5 μ also indicate that amplitude and phase fluctuations are increasingly more severe toward shorter wavelengths. At 10 μ , observations by Johnson et al. (1974) reveal typical amplitudes of $\frac{\lambda}{6}$. This approximate proportionality with λ^{-1} is expected if fringe vibration is caused primarily by different wavefront tilts at the two apertures. If this is true, then the variable component of relative tilt along the baseline could be the dominant source of "interferometric seeing." One significant implication is that if the amplitude of this component could always be reduced to zero by a servo system which tilts the adjusting mirrors, then interferometric seeing could be controlled. Such a system is described in Chapter 7.

An Instance of Anomalous Infrared Seeing

Although insufficient data has been gathered to characterize all forms of infrared seeing, at least two different regimes seem to exist and in each, changes can occur quickly during an observing night. In the regime characterized by Figure 6.1, fringes vibrate through distances corresponding to path variations of $\geq \frac{\lambda}{2}$. The frequency and amplitude of these vibrations are not only correlated with visual

seeing, they are correlated also with each other: as the amplitude decreases so does the frequency of motion until only small motions occur at low frequencies. Another regime is characterized by Figure 6.3 in which rapid changes occur at presumably $\lesssim \frac{\lambda}{4}$ amplitude but which always return the fringes to their initial location; here the slow wandering in phase is probably caused by telescope drift. This figure shows that one fringe phase is held constant for at least 30 seconds. Indeed, if the telescope had not drifted, this time would probably have exceeded five minutes. These observations were obtained in 4 arc sec seeing at the 61-inch telescope on R Leo when its hour angle was $\sim 2^h 15^m$ W; at that time a strong wind was blowing. This condition of the fringe signal was quite variable during the night.

This instance seems anomalous because it does not fit into the general scheme illustrated earlier in Figure 6.1. Here visual seeing is poor, 4 arc sec, and yet only small amplitude and phase changes occur but at high frequency. Perhaps this behavior is caused by interaction of the high wind with the dome slit.

Astrophysical Results

Observations and Reductions

During five nights in March and April 1975, the author and Dr. F. Low observed twelve stars using the 61-inch telescope on Mt. Bigelow and the 90-inch telescope on Kitt Peak. All visibility measurements were performed during 1-3 arc sec of visual seeing at a wavelength of 5μ and with a 0.7μ bandwidth. Different aperture diameters and

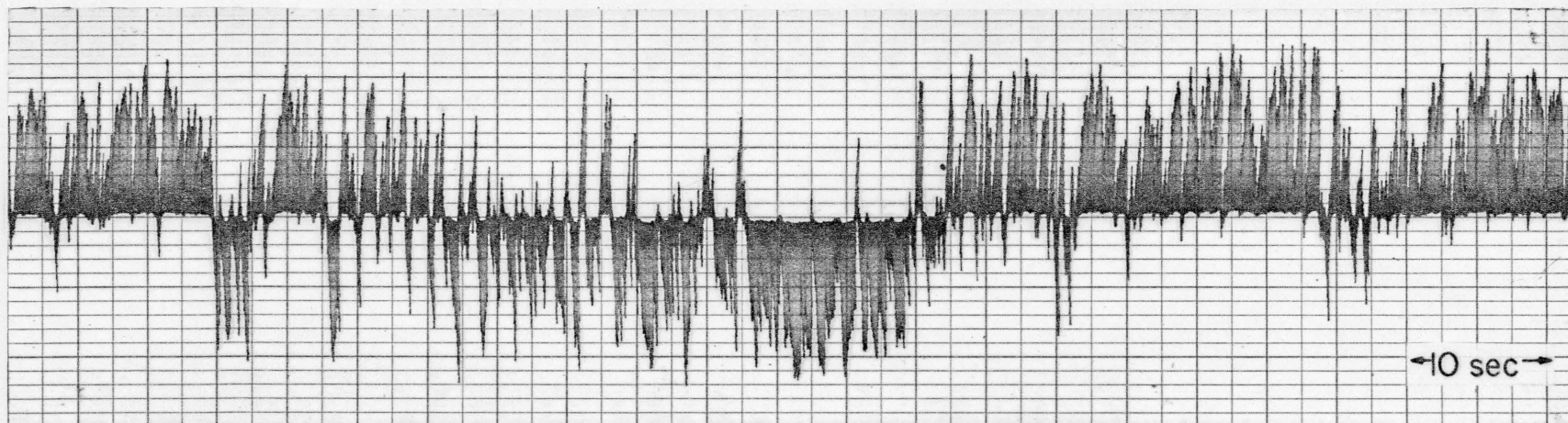


Figure 6.3. Anomalous Behavior of Infrared Seeing

The 5 μ phase-detected fringe signal is shown during an instance of peculiar seeing as discussed in the text.

baselines were used ranging respectively between 12-36 cm (4-14 inches) and between 102-187 cm (40-74 inches).

The procedures of measurement and reduction are identical to those discussed in Chapter 5. At each baseline the observational result for an object is expressed in terms of its average normalized fringe amplitude (N.F.A.). This value is converted into fringe visibility by dividing the former by the average N.F.A. of one or more nearby point sources. Uncertainty in the final result is caused by errors in the flux and fringe observations of both extended and point sources. The dominant sources of error are telescope setting errors and changes in atmospheric conditions as a function of time and position on the sky. Actual values of fringe visibility errors are based on errors in extended and point source visibility measurements. The latter are estimated from measurement repeatability and from uncertainty in determining the amplitude of the largest fringe signals. The final results contain 5-20 percent errors. To date, all measurements have been interpreted by a model which incorporates one or more uniform, circular sources.

Table 6.1 lists the N.F.A.'s, fringe visibilities, and the resulting angular diameters of eleven stars. IRC +10216 and VY CMa are definitely resolved. An upper limit is placed on the size of NML Cyg. Eight other stars are unresolved, and upper limits to their diameters are given. All except two (VX Sgr, W Hya) of these eight were used as comparison point sources. One additional object (IRC +10420) was

Table 6.1. Visibility Measurements and Angular Diameters for Observed Stellar Sources

Object	Average N.F.A.	Fringe Visibility	B(cm)	ANGULAR DIAMETER	
				$\theta_{5\mu}$ (arc sec)	θ_{\min} (arc sec)
VY CMa...	0.55 ± 0.05 0.52 ± 0.02	0.58 ± 0.08 0.55 ± 0.06	174 122	0.45 ± 0.15	0.36
IRC +10216	(See Figure 6.4a)			$\overline{1.6} \pm 0.06$ $\underline{0.44} \pm 0.06$	$\overline{1.6}$ $\underline{0.39}$
NML Cyg	0.58 ± 0.03	0.86 ± 0.06	122	<0.30	0.29
α Ori	0.95 ± 0.05	1.00*	174	<0.10*	0.041
α Boo	0.80 ± 0.09	1.00*	174	<0.10*	0.020
α Her	0.67 ± 0.05	1.00*	122	<0.10*	0.025
R Leo	0.68 ± 0.06	0.77 ± 0.09	174	<0.29	0.044
α Sco	0.56 ± 0.02	0.79 ± 0.04	187	<0.24	0.033
VX Sgr	0.78 ± 0.03	1.00 ± 0.03	187	<0.10	0.018
χ Cyg	0.58 ± 0.03	0.86 ± 0.05	122	<0.30	$\overline{0.036}$ $\underline{0.030}$
W Hya**	0.55 ± 0.03	0.66 ± 0.07	174	<0.33	0.052

*These stars are defined to have a visibility of 1.00.

**Only one observation at a large zenith angle exists for this star, so the upper limit is not a firm result.

observed but was at the limit of sensitivity for the original detector system (-0.5 mag with 8-inch apertures) so it will not be discussed further.

For comparison with the measured $5\ \mu$ angular diameters, Table 6.1 lists diameters obtained from a theoretical calculation (cf., equation 1.1 and Table 1.1). As discussed in Chapter 1, the theoretical diameter is calculated on the assumption that the observed $5\ \mu$ flux density is produced by a uniform, circular disk of unit emissivity with a color temperature T_c , and it therefore represents the minimum angular size possible for a thermal source with that temperature. For IRC +10216, VY CMa, and NML Cyg this disk corresponds to the circumstellar shell, and for the remaining stars it represents the stellar photosphere. For each star, Table 1.1 lists the $5\ \mu$ apparent magnitude and color temperature obtained from previous work as indicated.

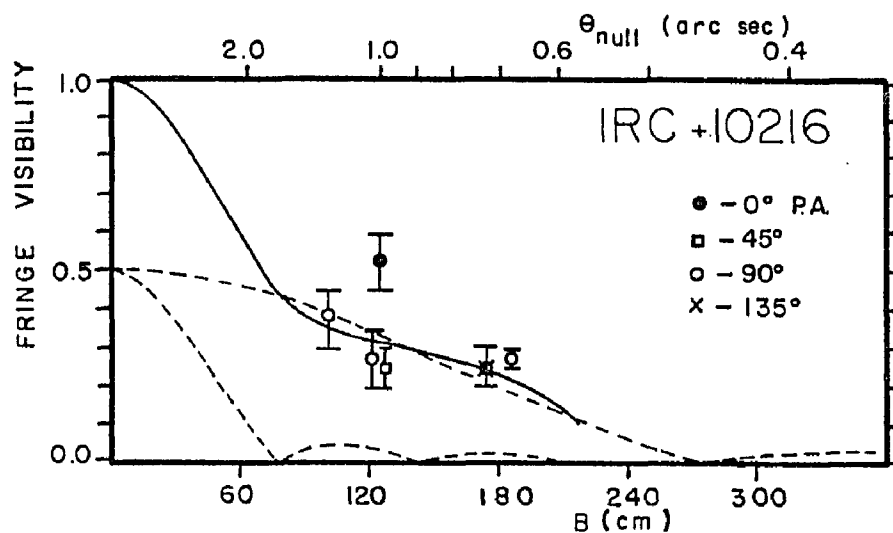
IRC +10216

IRC +10216 is one of the brightest known infrared stars at $5\ \mu$. Its spatial extent and structure were studied during two lunar occultations by Toombs et al. (1972), who interpret this object as a carbon star surrounded by a two component dust shell. The central component is optically thick with an angular diameter and temperature of 0.44 arc sec and 600°K . The outer component is colder ($\sim 375^\circ\text{K}$), optically thin, and has a diameter of 2.0 arc sec. Each part contributes about 50 percent of the total $5\ \mu$ flux and is assumed to be spherically symmetric.

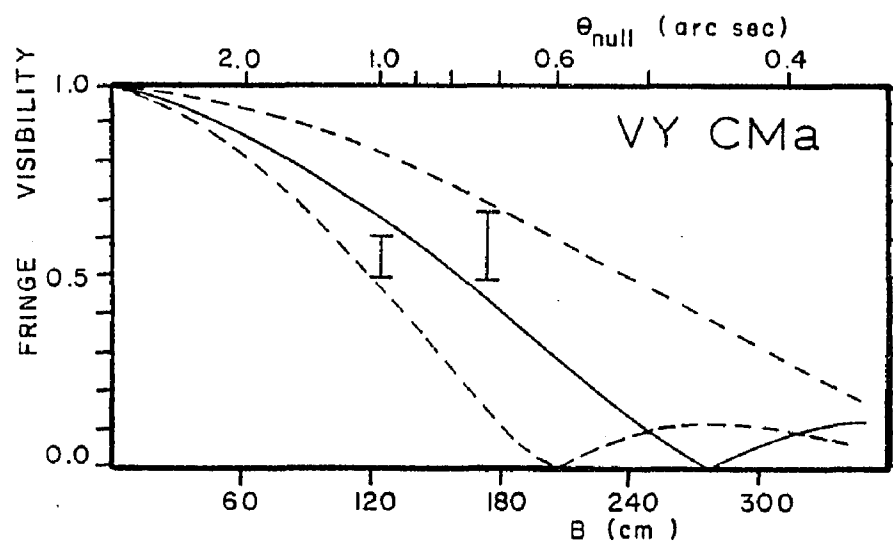
This object is known to be variable at 2.2μ (Becklin et al. 1969) with an amplitude of ~ 2 magnitudes over a period of about 600 days. It is also variable at 5μ because during the 19 months prior to the occultations, the 5μ flux decreased by about 0.6 magnitudes. In addition, flux measurements from the interferometer show that the 5μ magnitude has decreased from -5.0 in April 1975 to -3.9 in November 1975. If the source varies with an amplitude at 5μ of 1.0 magnitudes, then its angular dimensions may also vary as indicated in Table 6.1 by the corresponding theoretical diameters.

Although the occultation data are explained in terms of two concentric, circular sources, there is some photographic evidence for a flattened structure in the wavelength region from 0.5 – 0.7μ . However, between 0.75 – 0.9μ , the object appears starlike (Becklin et al. 1969). Nevertheless, the visibility measurements discussed below have been made at 45° increments of baseline position angle in order to study the shape of this source.

Figure 6.4a shows the fringe visibility results at several baselines. IRC +10216 is clearly resolved as is also shown in Figure 6.5 which illustrates the fringe and flux data obtained for it and its comparison point source, R Leo. At position angles of 0° and 90° , the results show evidence for a departure from spherical symmetry but more data are required to confirm this result. Most of the data is fit by the solid curve representing a theoretical two shell model with diameters of 1.6 and 0.44 arc sec. Individual components are assumed to be spherically symmetric, of uniform brightness distribution, and



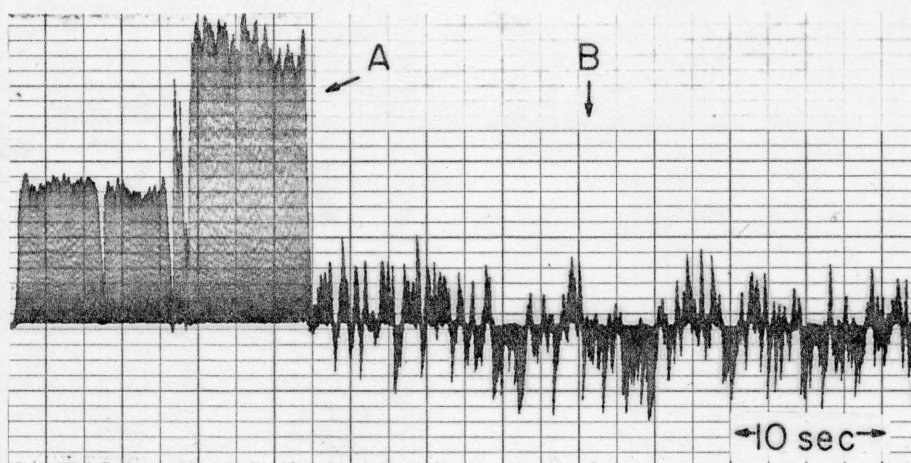
(a)



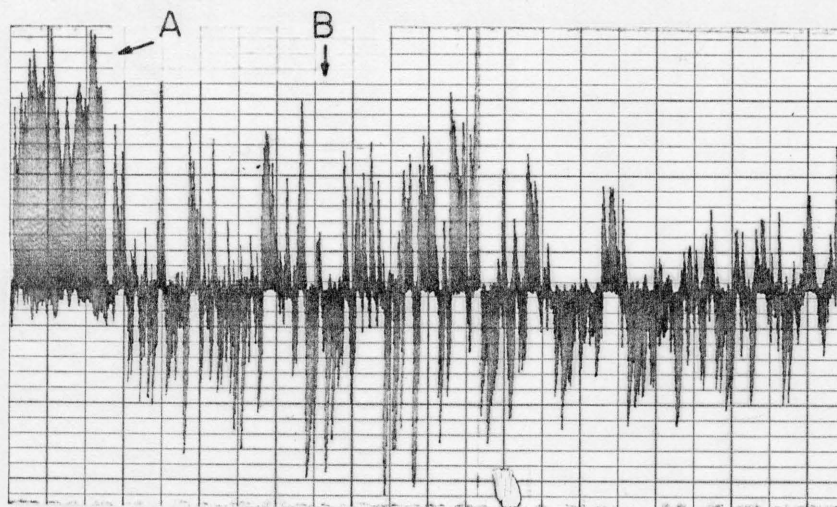
(b)

Figure 6.4. Visibility Measurements of IRC +10216 and VY CMa

(a) IRC +10216. The solid curve represents a theoretical, two-component model in which individual components are represented by dashed curves. (b) VY CMa. The solid and dashed curves are theoretical, single-source fits to the data.



(a). IRC +10216



(b). R Leo

Figure 6.5. Measurements of Fringe Amplitude and Flux from IRC +10216 and R Leo

The $5\ \mu$ phase-detected signals are shown in both photometric (A) and fringe-chopped (B) modes.

equally bright. Dashed lines are visibility curves for each shell. In each of the latter curves, the first visibility null is given by

$$\theta_{\text{null}} = 1.22 \frac{\lambda}{B}, \quad (6.1)$$

where B is the baseline length and $\lambda = 5 \mu$.

Although other geometries can be devised to fit the data, this particular model is preferred because of its good agreement with the occultation studies. In this case good fits exist for a range of shell diameters given approximately by 0.44 ± 0.06 arc sec and 1.6 ± 0.6 arc sec. However, the accompanying photometry yields a 5μ magnitude of about -5.0 , indicating that this object has brightened by about one magnitude since the occultations. The rather good agreement between the two diameter measurements suggests that the spatial extent and structure of IRC +10216 have not changed appreciably while the brightness has varied.

The 5μ measurements are in excellent agreement with θ_{min} . This fact confirms the conclusion that the 5μ radiation has a thermal origin (Toombs et al. 1972) and implies that the emitting region of each shell has nearly unit emissivity.

VY CMa

The star VY CMa is a well-known, peculiar M-type supergiant with associated nebulosity. In a series of papers, Herbig (1970a, 1970b, 1972, 1974a) has explained this object as a young, M3-5 supergiant star surrounded by a flattened disk of dust and gas. Although the disk thickness is not known, one of Herbig's models (1970b)

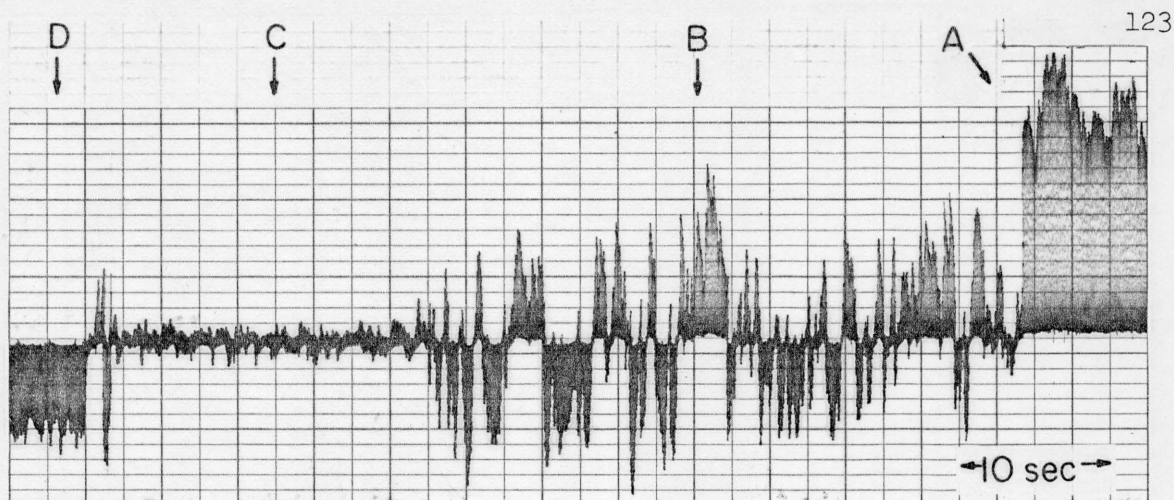
confines the dust between stellar latitudes of $\pm 20^\circ$. The angular extent is then about 1 arc sec by 2 arc sec as seen in the equatorial plane.

Table 6.1 lists the N.F.A.'s obtained for VY CMa at two different aperture separations in the east-west plane. Figure 6.6 shows both the flux and fringe measurements of VY CMa relative to its comparison, point source, α Ori. Here, VY CMa is clearly resolved but shows a larger visibility than IRC +10216. The visibilities are plotted in Figure 6.4b. The solid curve represents a possible single-source fit (assuming spherical symmetry and uniform brightness distribution) and yields a diameter of 0.45 ± 0.15 arc sec. This angular size disagrees not only with Herbig's model, as described above, but also with a recent radiative transfer model (Apruzese 1975) which predicts diameters of 1.2 arc sec at 2.6μ and 5-6 arc sec at 10μ .

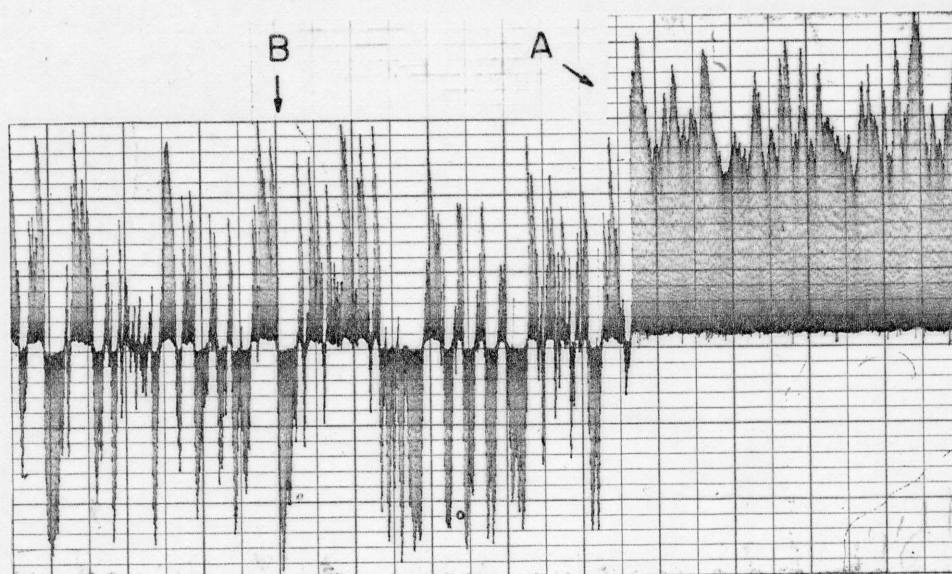
It is interesting to note that for VY CMa, as for IRC +10216, there is good agreement between the measured 5μ angular diameter and θ_{\min} . As before, it appears that the shell has nearly unit emissivity.

NML Cyg

This highly reddened M giant star possesses an infrared luminosity and spectrum which are similar to those of VY CMa (Low et al. 1970). However, Herbig (1974b) has drawn attention to some major differences between these objects. As given in Table 6.1 the interferometric observations place an upper limit of 0.3 arc sec on the angular diameter of NML Cyg. Although the star has not been resolved, this limit may be significant because of its closeness to θ_{\min} . Thus, it



(a) VY CMa



(b) α Ori

Figure 6.6. Measurements of Fringe Amplitude and Flux from VY CMa and α Ori

The 5μ phase-detected signals are shown in the photometric (A) and fringe-chopped modes (B). Portions (C) and (D) show the fringe-chopped and photometric signals from the sky alone--no star in the field of view.

seems possible that the emissivity and structure of the dust shell of NML Cyg are similar to those of IRC +10216 and VY CMa. Such shells are thought to exist in other infrared stars such as R Mon, HD 45677, and the Becklin-Neugebauer source in Orion (Low et al. 1970). The shell temperatures of all these stars are remarkably similar ($\sim 600^\circ\text{K}$), possibly indicating that some common process is operating in these objects. However, further observations of NML Cyg at larger baselines are needed to strengthen this conclusion.

Unresolved Stars

Eight stars are unresolved by these observations. Table 6.1 lists their N.F.A.'s at the largest available aperture separation. These measurements are converted into fringe visibilities by comparison with data from α Ori, α Boo, or α Her, which are assumed to be true point sources on the basis of spectrophotometry and previous optical diameter measurements (Table 1.1). These visibilities are then compared with theoretical models for single sources in order to specify an upper limit on the angular diameter of each object.

CHAPTER 7

CONCLUSIONS AND IDEAS FOR THE FUTURE

The infrared spatial interferometer is a remarkably successful instrument which has measured angular sizes and shapes of circumstellar dust shells and has characterized the factors which limit the scope and accuracy of spatial interferometry, such as atmospheric turbulence and instrument design. The results from these studies can now be summarized and incorporated into the construction of an improved interferometer. This instrument would overcome present limitations and could study fainter and smaller infrared sources over a larger range of wavelengths and baselines.

Observational Results

In this project a spatial interferometer was designed, built, tested, and utilized on several telescopes to measure fringe visibilities of circumstellar dust shells at wavelengths of 2.2, 3.5, and 5.0 microns. When operated on the 61-inch and 90-inch telescopes, this instrument measures visibilities accurate to 5-20 percent. Accuracy is limited primarily by atmospheric turbulence.

Eleven stars were observed at a wavelength of $5\ \mu$ during good seeing conditions with baselines ranging from 1.0 to 1.9 meters. A test object, IRC +10216, was easily resolved. Its visibility data are consistent with a model proposed by earlier lunar occultation studies.

This model consists of two concentric dust shells with angular diameters of 0.44 and 2.0 arc sec. Efforts were made to discover any departures from spherical symmetry but no clear-cut evidence was found. Interestingly, the size and structure of this source did not change in the 19 months after the occultations even though the $5\ \mu$ flux increased about one magnitude. Another infrared star, VY CMa, was resolved for the first time ever at $5\ \mu$. Its angular diameter is approximately 0.45 ± 0.15 arc sec. Upper limits are placed on the angular diameters of nine other stars, one of which is NML Cyg whose upper limit is 0.30 arc sec. The angular diameter for each of these three stars nearly equals the expected diameter of a uniform, circular, unit emissivity disk having the same observed $5\ \mu$ flux and color temperature. This agreement could imply that a common physical process is operating to produce and/or sustain these dust shells.

In addition to astronomical measurements, the interferometer has studied atmospheric behavior at infrared wavelengths. Atmospheric seeing induces phase and amplitude fluctuations of the $5\ \mu$ interference fringes at frequencies ranging from ~ 0 to > 40 Hz from night to night. On rare occasions these fluctuations are very small and fringes remain stable showing only small phase shifts of $\lesssim \frac{\pi}{2}$ radians during a time of $\gtrsim 40$ seconds. The amplitude and frequency characteristics of fringe fluctuations are correlated with visual seeing and appear to be inversely proportional to wavelength from ~ 0.5 to $10\ \mu$. However, another regime of infrared seeing exists in which phase shifts of $\gtrsim \frac{\pi}{2}$ occur suddenly and vanish quickly returning the fringes to their original phase, which remains the same for at least several minutes.

It is now clear that the existing interferometer resolves angular diameters of λ 0.1 arc sec using a 1.9 meter baseline at a wavelength of 5 μ during good seeing conditions. Although the interferometric technique has certain limitations, especially those of atmospheric seeing, the next two sections show that there are no cogent reasons against expanding observations to longer baselines and wavelengths, where new astronomical problems may be studied. Indeed, atmospheric seeing should improve at the longer wavelengths of 11, 20 μ ; such observations might be easier to conduct than those at 5 μ .

Limitations to This Technique

At the present time, the most serious limitations on infrared spatial interferometry are imposed by atmospheric seeing. As discussed in Chapters 5 and 6, seeing causes the fringe signal to fluctuate in phase and amplitude so that an observer is no longer in full control of the measurement process. Instead he must rely on the atmosphere to align fringes properly so that observations of an extended source and its comparison point source are measurements of the same quantity; i.e., the amplitude of the zero-order fringe when the two images are in \sim 100 percent overlap. At present, spatial interferometry can only be performed when the visual seeing disk from the full telescope aperture is λ 3 arc sec and fringe fluctuations occur at frequencies less than the 40 Hz chopping rate. Consequently an observer may "waste" a good deal of telescope time while waiting for such conditions to occur.

There are other factors which have limited the scope and accuracy of infrared spatial interferometry. These dominate when seeing conditions are excellent. They are summarized below.

1. Wavelength. Observations are now confined to wavelengths of 2.2, 3.5, and 5.0 μ because of the limited spectral response of InSb detectors and because the uncooled aperture mask adds unwanted background radiation and photon noise to the desired signals.
2. Sensitivity. Present observations have a 5 μ limiting magnitude of $\zeta + 1.0$ which results mainly from the use of only two small portions of a telescope's primary mirror. In addition, signals cannot be integrated because of atmospheric seeing fluctuations. If the uncooled aperture mask were eliminated and improved detector systems used, then the limiting magnitude would be extended at least two magnitudes. Also, apertures larger than the present 14 inches may be used but, as discussed in Chapter 3, this requires larger telescopes.
3. Telescope Pointing and Tracking. During excellent seeing when fringes are stable, a telescope must center the zero-order fringe and track it accurately. The tolerances quoted in Chapter 3 are very demanding and most telescopes are unable to satisfy them. Consequently a large error can occur in an object's visibility because measurements of the extended source and its comparison point source may not refer to the same observational quantity. Invisible objects are especially

prone to this error since their images are hard to position accurately and repeatably.

4. Baseline. Both longer and shorter baselines are needed for observations. The former supplies the resolution capability which must improve if angular diameters < 0.1 arc sec at 5μ are to be resolved. At longer wavelengths, baselines must be proportionately longer to keep resolution constant. Unfortunately, longer baselines mean more stringent requirements on telescope pointing and tracking. Smaller baselines are needed to supply additional data points on visibility curves such as that of IRC +10216 (Chapter 6).
5. Fringe Modulation. The square wave modulation technique does not effectively separate amplitude and phase fluctuations of the fringes. For example, if the atmosphere causes a shift in fringe phase, then the chopper no longer oscillates exactly between positions of maximum and minimum fringe amplitude so that, during each half cycle of chopper operation, at least part of the fringe signal is comprised of identical but oppositely phased components which cancel in the final output. Thus amplitude fluctuations occur in the output even though the atmosphere may leave fringe amplitude constant and excessive noise appears in the fringe signal.
6. Alignment. It is very time-consuming to align the interferometer from scratch. In addition, when an observer changes the baseline position angle, the instrument must be realigned.

7. Data Analysis. This is a very time-consuming process which involves some personal judgment to determine the maximum fringe signals (see Chapter 5). It is desirable to provide a quicker form of analysis which is more automated and operated in real time at the telescope. This solution would also enable the observer to determine when he has accumulated enough data to yield a meaningful result.

All of these limitations can be easily overcome in future work. The next section shows how this is possible with improvements in instrumentation.

Improvements in Instrumentation

Mr. Robert Howell has recently suggested a new technique for fringe modulation which has already been incorporated into the interferometer and utilized for stellar observations. In this idea square wave modulation is replaced by a sawtooth waveform so that the fringe chopper sweeps the fringes linearly through one wavelength of path difference and then suddenly returns them to the starting position. The detected fringe signal becomes a 40 Hz sine wave whose amplitude and frequency are modulated independently by atmospheric shifts of fringe amplitude and phase. These two effects can now be measured separately and the fringe signal is less noisy.

In conjunction with this new form of modulation, Dr. Frank Low has suggested the use of a phase-locked loop to sense phase shifts of the fringe signal. This electronic circuit tracks fringe phase and provides a corrected reference (sync) signal so that the fringe signal

can be phase-detected and integrated. This improvement has already been added to the data analysis equipment. It has been noticed that the loop circuit tracks fringe phase shifts even when visual seeing is worse than 3 arc sec.

Another improvement is to replace the uncooled aperture mask with a lower background version as illustrated in Figure 7.1. Here the roof mirror is made undersized so that its faces determine the size and shape of the two beams. A concave spherical mirror is located above the roof mirror; its distance from the detector equals its own radius of curvature. Thus, that portion of the detector's field of view which is larger than the roof mirror is reimaged back onto the detector and its cold surroundings. This technique will significantly improve the interferometer's sensitivity and will enable it to be used at longer wavelengths where background reduction is of prime importance. In this event new detector systems will be needed and more crystals must be added to the fringe chopper to increase its throw. These, however, are easy changes to make.

A more ambitious improvement involves the use of a servo control to correct for fringe amplitude fluctuations in real time. Since these originate from atmospheric wavefront tilts which cause the images to dance in the focal plane, the servo mechanism must monitor the displacement of each image from its nominal position and feedback error signals which tilt mirrors to reposition the images. One possible scheme is illustrated in Figure 7.2. If the image sensors operate at visual or near-infrared ($\sim 3 \mu$) wavelengths, then the far-infrared images should be corrected very accurately; fringe amplitude and phase

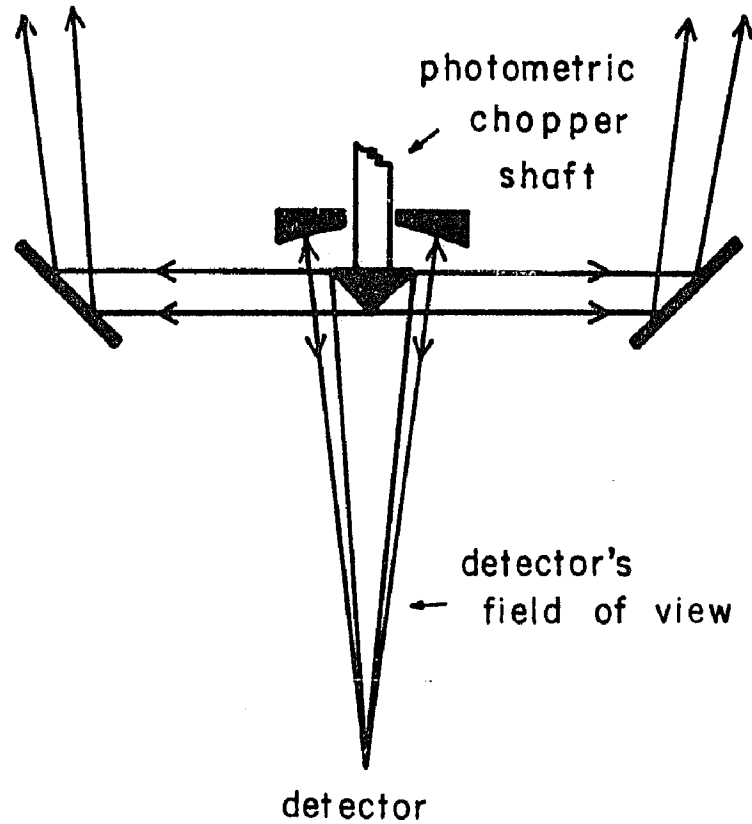


Figure 7.1. An Improved, Low Background Aperture Mask

A reimaging baffle mirror replaces the aperture mask of Figure 3.2.

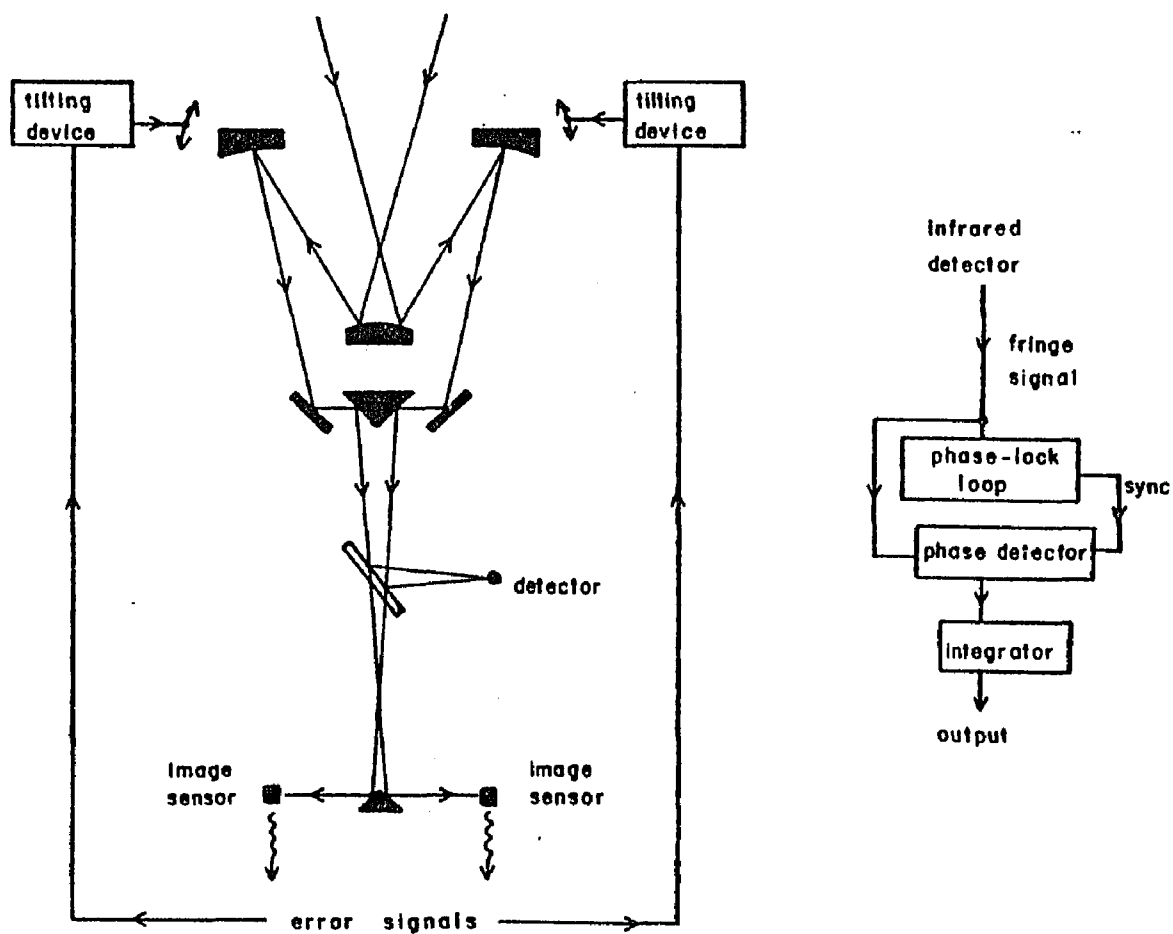


Figure 7.2. Schematic Diagram of a Servo-Controlled Spatial Interferometer

The servo apparatus maintains the visual images in 100 percent overlap at the focus. Any remaining phase shifts of fringes are tracked by a phase-locked loop.

shifts should be virtually eliminated. If any phase shifts still persist, their effects can be eliminated with the phase-locked loop described earlier or with a second servo control which changes the DC level of the fringe chopper to provide small path corrections. With this technique the interferometer can operate in relatively poor seeing conditions and greater sensitivity will be achieved by signal integration. Thus fewer telescope nights would be wasted. This system would also provide important new data concerning atmospheric turbulence. For example, it would measure the amplitudes and frequencies of image motions and could determine if phase shifts result solely from wavefront tilts.

Alignment procedures can also be improved. At present two factors make the instrument hard to align. First, the paths of the two beams must be equalized inside the interferometer and, second, the interferometer's optical axis must be aligned along that of the telescope. The former can be more quickly adjusted by using the arrangement shown in Figure 7.3. The idea is to reimage a visible point source in the eyepiece after its light has passed through the interferometer optics; a person moves the roof mirror to equalize the paths until white-light fringes are seen within the image. This search becomes much quicker if a special point source is used (Martienssen and Spiller 1964). The advantage of this source is that the coherence length of its light can be easily varied over a large range. Thus a person would set this length to be long initially, then find fringes, then narrow the length, and so on until the paths are accurately equalized. The second form of alignment is more difficult to improve upon

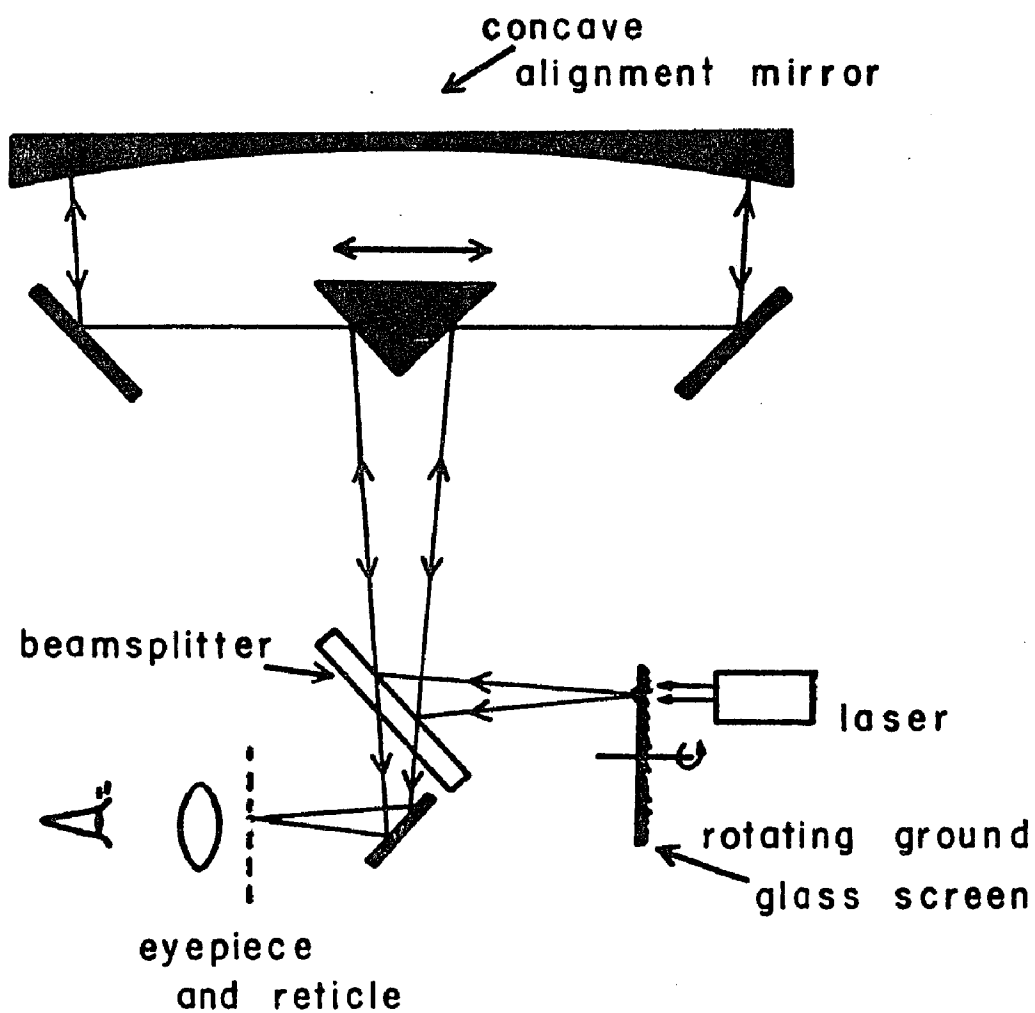


Figure 7.3. A New Alignment Technique

A special laser source with adjustable coherence length can be used to equalize paths within the interferometer.

because it seems to necessitate the placement of optics on or within the telescope structure so that laser beams can be reflected through the telescope into the interferometer. Although feasible, this method would seem to be more applicable on a special purpose telescope which is dedicated to spatial interferometry.

Future Observational Goals

In the immediate future, observational work will continue to concentrate on atmospheric phenomena and the properties of infrared stars. The first goal is to study these topics at longer wavelengths (11, 20 μ) and with both larger and smaller baselines. Several new and interesting effects will then be observable. For example, with baselines less than 100 cm, seeing at 5 μ should be much improved because wavefront tilts along the baseline will cause smaller path differences between beams and because theory predicts (Chapter 2) that the wavefront should be coherent over this distance. Theory also predicts that seeing improves at longer wavelengths. In the case of infrared stars, larger baselines will enable the interferometer to resolve smaller and fainter objects. At longer wavelengths circumstellar dust shells should have larger angular diameters.

As described in Chapter 1, many physical properties of infrared stars can be studied by spatial interferometry. By observing an object over a range of baselines and wavelengths, it is possible to map the distribution of dust within its circumstellar shell and to provide data which theoretical models require in order to determine the physical and chemical properties of the dust grains. Another goal

is to study the shapes of these dust shells. Present data has ruled out gross departures from spherical symmetry in one object, IRC +10216, but more data over a large range of baselines is needed to be completely sure of this result and to observe any small amplitude effects. The shape of VY CMa is also of great interest since it is predicted to be flattened. Two other goals are, first, to search for variations in the sizes of dust shells surrounding variable stars, such as IRC +10216, and, second, to see if the observed angular diameters of other stars agree with their theoretical, thermal values (θ_{\min}).

Solar system objects should also be studied in the near future. In particular, interferometric measurements of asteroidal diameters are needed to verify determinations from other, less direct techniques. Both asteroids and planetary satellites may be valuable as calibration objects for the interferometry.

In the more distant future, improved sensitivity will enable galactic nuclei to be resolved in hopes of ascertaining how these sources generate such enormous energies. If the proposed servo-mechanism is built, then very large baseline (> 5 meters) special purpose interferometers can be built and it may be possible to measure fringe phase accurately enough to perform aperture synthesis.

APPENDIX A

DESIGN AND TESTS OF THE PIEZOELECTRIC CRYSTAL STACKS

One of the critical questions in designing the interferometer was concerned with how to translate an adjusting mirror through a distance of $\frac{\lambda}{2}$ to provide a fringe chopper. Since it was desired to have the chopper operate at wavelengths as low as 2.2 μ , mechanical techniques were abandoned in favor of piezoelectric crystal stacks which had already been experimented with by Mr. M. Reed and Dr. R. Thompson.

The use of such crystals in a fringe chopper is convenient for three main reasons. First, the chopper's frequency and amplitude are easily controlled by simple electronics and the mechanism operates over the wavelength range from ≤ 2 to 10 μ . Second, the entire crystal-mirror arrangement is rigid and compact. Third, the chopper is inexpensive since the crystals and electronics were borrowed from the above two individuals. Also, piezoelectric crystals have a natural application with the other adjusting mirror since that mirror can be translated in small but constant increments to align the fringes accurately on the slotted mask.

Both crystal stacks are comprised of one-inch diameter, lead zirconate titanate elements stacked in parallel between thin brass connectors. Each element has a half-inch hole in the center, and an insulating phenolic core runs through the stack to hold it in place.

This design has been copied from that of Reed and Thompson. However, instead of using a nylon screw through the core to compress the stack, this author has used a 10-32 brass screw which runs through the adjusting mirror mount and the stack and is very tightly clamped to a 1/8-inch aluminum plate which serves as the base. The entire arrangement constitutes a removable module which inserts into a recess of the stage and is firmly screwed to the stage itself. The fringe chopper stack contains ten elements; in operation, it gives an audible chopping sound which is probably caused by the stretching and relaxation of the brass screw. The alignment stack contains only six elements, since its amplitude does not need to be as large.

The dynamic properties and reliability of both crystal systems have been studied in several laboratory experiments over a range of voltages (0-1200 volts) and frequencies (0-40 Hz). The most critical and informative test was performed using a crystal stack as the movable mirror in a conventional Michelson interferometer. Illumination was provided by a He - Ne laser ($\lambda = 0.6328 \mu$). The crystal stack was driven electronically with a slow ramp input which increased in amplitude from zero to 1000 volts at a rate of about 0.09 Hz. This signal originated from an audio oscillator and was amplified by a Kepco operational power supply (OPS-2000). As the mirror moved, a phototransistor counted fringes at the output and displayed the results on a strip chart record.

The results of this test on fringe chopper stack are shown in Figure A.1. The crystal elements of each stack expand individually at a rate of about $0.5 \mu/\text{KV}$. As shown, both stacks exhibit some nonlinear

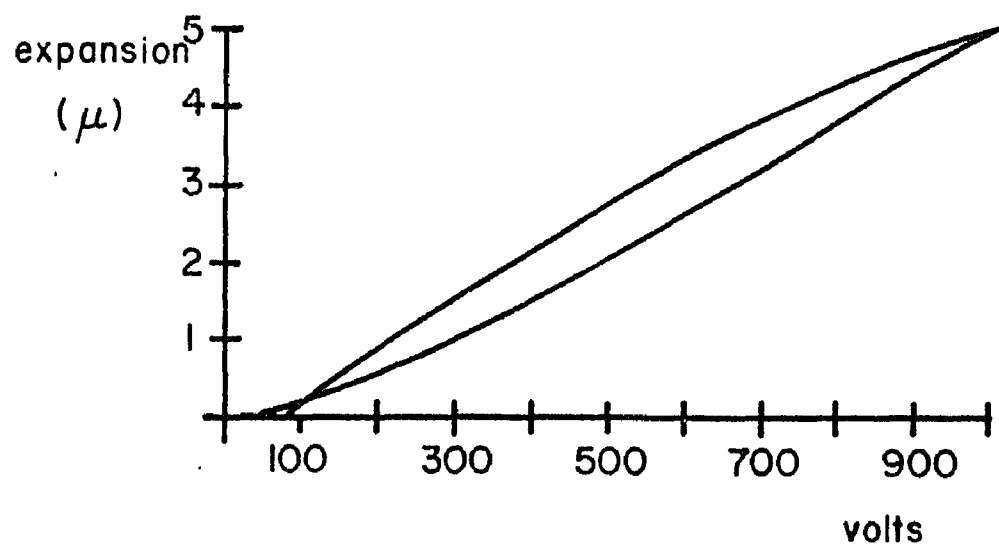


Figure A.1. Expansion Versus Voltage for the Piezoelectric Fringe Chopper

and hysteresis effects. These effects do not inhibit operation of the fringe chopper because it cycles between two points on the curve; the path taken between these points is irrelevant. However, hysteresis does affect the alignment stack because it is difficult to fine tune simply by stepping the voltage up and down to maximize the fringe signal. To date, no temperature dependent effects have been noticed in fringe chopper operation. In addition, the chopper's amplitude and efficiency are not degraded by operating at frequencies up to 40 Hz.

In the interferometer, fringe chopper electronics operate similarly to those used in the lab tests. The detailed arrangement, including the amplitude adjustment, is described at the end of Chapter 3. However, it should be noted here that the Kepco operational power supply is a unipolar device so the fringe chopper is not modulated about a zero voltage reference level. Rather, there is a DC level of ~ 500 volts upon which is impressed a square wave of 500 volts amplitude for chopper operation at a wavelength of 5μ . At the present time the chopper can be operated at a maximum wavelength of 10μ with a 1100 volt square wave.

REFERENCES

- Allen, C. W. 1973, Astrophysical Quantities (London: Athlone), p. 125.
- Anderson, J. A. 1920, Ap. J., 51, 263.
- Apruzese, J. P. 1975, Ap. J., 196, 761.
- Balick, B., and Brown, R. L. 1974, Ap. J., 194, 265.
- Balick, B., and Sanders, R. H. 1974, Ap. J., 192, 325.
- Beavers, W. I., and Swift, W. D. 1968, Appl. Op., 7, 1975.
- Becklin, E. E., Frogel, J. A., Hyland, A. R., Kristian, J., and Neugebauer, G. 1969, Ap. J. (Letters), 158, L133.
- Becklin, E. E., Matthews, K., Neugebauer, G., and Wynn-Williams, C. G. 1973, Ap. J. (Letters), 186, L69.
- Becklin, E. E., and Neugebauer, G. 1967, Ap. J., 147, 799.
- Born, M., and Wolf, E. 1959, Principles of Optics (London: Pergamon Press), p. 490.
- Breckenridge, J. B. 1976, J. Opt. Soc. Am., 66, 143.
- Brown, R. H. 1974, The Intensity Interferometer (New York: John Wiley and Sons, Inc.).
- Chapman, C. R., Morrison, D., and Zellner, B. 1975, Icarus, 25, 104.
- Code, A. D. 1973, Ann. Rev. Astr. and Ap., 11, 239.
- Code, A. D. 1975, Dudley Obs. Rep., No. 9, 221.
- Cohen, M. 1974, P.A.S.P., 86, 813.
- Cohen, M., and Barlow, M. J. 1974, Ap. J., 193, 401.
- Currie, D. G., Knapp, S. L., and Liewer, K. M. 1974, Ap. J., 187, 131.
- De Vorkin, D. H. 1975, J. Hist. Astro., 6, 1.
- Dyck, H. M. and Milkey, R. W. 1972, P.A.S.P., 84, 597.

- Evans, D. S. 1955, M.N.R.A.S., 115, 468.
- Fix, J. D., and Alexander, D. R. 1974, Ap. J. (Letters), 188, L91.
- Fizeau, H. 1868, Comptes rendus, 66, 932.
- Fomalhont, E. B., and Wright, M. C. H. 1974, In Galactic and Extra-Galactic Radio Astronomy, edited by G. L. Verschurr and K. I. Kellermann (New York: Springer-Verlag), p. 256.
- Fried, D. L. 1966, J. Opt. Soc. Am., 56, 1372.
- Gatley, I., Becklin, E. E., Matthews, K., Neugebauer, G., Penston, M. V., and Scoville, N. 1974, Ap. J. (Letters), 191, L121.
- Gehrels, T. (editor) 1971, Physical Studies of Minor Planets (Washington: U.S. Government Printing Office).
- Gehrz, R. D., Ney, E. P., Becklin, E. E., and Neugebauer, G. 1973, Astrop. L., 13, 89.
- Gehrz, R. D., and Woolf, N. J. 1971, Ap. J., 165, 285.
- Geisel, S. L. 1970, Ap. J. (Letters), 161, L105.
- Geisel, S. L., Kleinmann, D. E., and Low, F. J. 1970, Ap. J. (Letters), 161, L101.
- Gezari, D. Y., Labeyrie, A., and Stachnik, R. V. 1972, Ap. J. (Letters), 173, L1.
- Gillett, F. C., Low, F. J., and Stein, W. A. 1968, Ap. J., 154, 677.
- Gillett, F. C., Merrill, K. M., and Stein, W. A. 1971, Ap. J., 164, 83.
- Gilman, R. C. 1969, Ap. J. (Letters), 155, L185.
- Gilman, R. C. 1974, Ap. J., 188, 87.
- Hall, D. N. B., Aikens, R. S., Joyce, R., and McCurnin, T. W. 1975, Applied Optics, 14, 450.
- Herbig, G. H. 1970a, Evolution Stellaire Avant la Sequence Principale (Mem. Soc. Roy. Sci. Liege, 19), p. 13.
- Herbig, G. H. 1970b, Ap. J., 162, 557.
- Herbig, G. H. 1972, Ap. J., 172, 375.

- Herbig, G. H. 1974a, Ap. J., 188, 533.
- Herbig, G. H. 1974b, Ap. J., 189, 73.
- Humphreys, R. M. 1974, Ap. J., 188, 75.
- Humphreys, R. M., Strecker, D. W., and Ney, E. P. 1972, Ap. J., 172, 75.
- Hyland, A. R., Becklin, E. E., Frogel, J. A., and Neugebauer, G. 1972, Astron. and Astrophysics., 16, 204.
- Johnson, H. L. 1966, Ann. Rev. Astr. and Ap., 4, 193.
- Johnson, H. L., Mendoza, E. E., and Wisniewski, W. Z. 1965, Ap. J., 142, 1249.
- Johnson, M. A., Betz, A. L., and Townes, C. H. 1974, Phys. Rev. Lett., 33, 1617.
- Jones, T. W., and Stein, W. A. 1975, Ap. J., 197, 297.
- Kleinmann, D. E., and Low, F. J. 1967, Ap. J. (Letters), 149, L1.
- Kleinmann, D. E., and Low, F. J. 1970a, Ap. J. (Letters), 159, L165.
- Kleinmann, D. E., and Low, F. J. 1970b, Ap. J. (Letters), 161, L203.
- Knacke, R. F., and Capps, R. W., 1974, Ap. J. (Letters), 192, L19.
- Knapp, S. L. 1974, Dissertation, University of Maryland.
- Labeyrie, A. 1970, Astron. Astrophys., 6, 85.
- Lang, K. R. 1971, Highlights of Astronomy, Vol. 2 (Holland: D. Reidel Publishing Company), p. 626.
- Larson, R. B. 1969, M.N.R.A.S., 145, 271.
- Lemke, D., and Low, F. J. 1972, Ap. J. (Letters), 177, L53.
- Low, F. J. 1961, J. Opt. Soc. Am., 51, 1300.
- Low, F. J. 1970, Ap. J. (Letters), 159, L173.
- Low, F. J., Johnson, H. L., Kleinmann, D. E., Latham, A. S., and Geisel, S. L. 1970, Ap. J., 160, 531.
- Low, F. J., and Rieke, G. H. 1974, Methods of Experimental Physics (New York: Academic Press), p. 453.

- Low, F. J., and Smith, B. J. 1966, Nature, 212, 675.
- Low, F. J., and Swamy, K. S. K. 1970, Nature, 227, 1333.
- Martienssen, W., and Spiller, E. 1964, Am. J. Phys., 32, 919.
- McCarthy, D. W., and Low, F. J. 1975, Ap. J. (Letters), 202, L37.
- Meinel, A. B. 1960, In Telescopes, edited by G. P. Kuiper and B. M. Middlehurst (Chicago: Univ. of Chicago Press), p. 154.
- Mendoza V., E. E. 1966, Ap. J., 143, 1010.
- Mendoza V., E. E. 1968, Ap. J., 151, 977.
- Meyer-Arendt, J. R., and Emmanuel, C. B. 1965, National Bureau of Standards, Technical Note 25.
- Michelson, A. A. 1891, P.A.S.P., 3, 274.
- Michelson, A. A., and Pease, F. G. 1921, Ap. J., 53, 249.
- Miller, R. H. 1970, AURA Eng. Tech. Rep. No. 31.
- Neugebauer, G., Sargent, W.L.W., Westphal, J. A. 1971, P.A.S.P., 83, 305.
- Ney, E. P. 1975, Sky and Tel., 49, 21.
- Reddish, V. C. 1967, M.N.R.A.S., 135, 251.
- Rieke, G. H. 1975, Associate Professor of Astronomy, Lunar and Planetary Laboratory, Univ. of Arizona, private communication.
- Rieke, G. H., and Low, F. J. 1972, Ap. J. (Letters), 177, L115.
- Rieke, G. H., and Low, F. J. 1973, Ap. J., 184, 415.
- Rieke, G. H., and Low, F. J. 1975, Ap. J., 197, 17.
- Robinson, G., Hyland, A. R., and Thomas, J. A. 1973, M.N.R.A.S., 161, 281.
- Ryle, M. 1975, Science, 188, 1071.
- Shawl, S. J. 1972, Dissertation, University of Texas at Austin.

- Smart, W. M. 1965, Text-Book on Spherical Astronomy (Cambridge: University Press), p. 61.
- Stein, W. A. 1975, P.A.S.P., 87, 5.
- Stein, W. A., and Ney, E. P. 1974, P.A.S.P., 86, 380.
- Stock, J., and Keller, G. 1960, In Telescopes, edited by G. P. Kuiper and B. M. Middlehurst (Chicago: Univ. of Chicago Press), p. 138.
- Strom, K. M., Strom, S. E., and Grasdalen, G. L. 1974, Ap. J., 187, 83.
- Strom, K. M., Strom, S. E., and Yost, J. 1971, Ap. J., 165, 479.
- Strom, K. M., Strom, S. E., Yost, J., Carrasco, L., and Grasdalen, G. 1972, Ap. J., 173, 353.
- Strom, R. G., Miley, G. K., and Oort, J. 1975, Sci. Am., 233, 26.
- Swenson, G. W., and Kellermann, K. I. 1975, Science, 188, 1263.
- Thomas, R. N. 1973, Astr. and Ap., 29, 297.
- Toombs, R. I., Becklin, E. E., Frogel, J. A., Law, S. K., Porter, F. C., and Westphal, J. A. 1972, Ap. J. (Letters), 173, L71.
- Treffers, R., and Cohen, M. 1974, Ap. J., 188, 545.
- Wallerstein, G. 1971, Ap. J., 166, 725.
- Wickes, W. C., and Dicke, R. H. 1973, Astron. J., 78, 757.
- Wolf, N. J. 1973, in Interstellar Dust and Related Topics, I.A.U. Symposium No. 52, edited by J. M. Greenburg and H. C. Van de Hulst (Dordrecht: D. Reidel Publishing Co.), p. 485.
- Wolf, N. J., and Ney, E. P. 1969, Ap. J. (Letters), 155, L181.
- Woods Hole Summer Study on Synthetic Aperture Optics, 1967, Vol. 1, 2 (Washington: National Academy of Sciences--National Research Council).
- Wynn-Williams, C. G., and Becklin, E. E. 1974, P.A.S.P., 86, 5.
- Young, A. T. 1971, Sky and Tel., 42, 139.

Young, A. T. 1974, Ap. J., 189, 587.

Zappala, R. R., Becklin, E. E., Matthews, K., and Neugebauer, G. 1974,
Ap. J., 192, 109.